

September 30, 2013

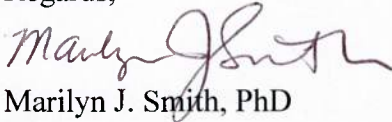
Defense Technical Information Center  
8725 John J Kinman Road, Suite 0944  
Fort Belvoir, VA 22060-6218

Dear Sir/Madam,

Enclosed you will find the final technical report for the ONR grant N0001409-1-1019, *Deconstructing Hub Drag*. The report is in two sections: **Part I (Experiments) and Part II (Computational Development and Analysis)**, as discussed and agreed by the ONR technical monitor (Judah Milgram) and the Co-Principal Investigators at the Georgia Institute of Technology.

If you have questions or concerns with the reports, please feel free to contact me via any of the means listed below.

Regards,



Marilyn J. Smith, PhD

Professor

Daniel Guggenheim School of Aerospace Engineering

Georgia Institute of Technology

Atlanta, GA 30332-0150

(404)894-3065

FAX: (404)894-2760

[marilyn.smith@aerospace.gatech.edu](mailto:marilyn.smith@aerospace.gatech.edu)

DISTRIBUTION STATEMENT A: Distribution approved for public release; distribution is unlimited

# Deconstructing Hub Drag

Final Technical Report

Part II: Computational Development and Analysis

Grant: N0001409-1-1019

by:

Rajiv Shenoy Marilyn J. Smith

Daniel Guggenheim School of Aerospace Engineering

Georgia Institute of Technology

Atlanta, Georgia, 30332-0150, USA

Phone: (404) 894-3065

Fax: (404) 894-2760

email: marilyn.smith@ae.gatech.edu

Submitted to:

Office of Naval Research  
875 North Randolph Street  
Arlington, VA 22203-1995

September 30, 2013

20131015009

# Contents

<b>1</b>	<b>Summary</b>	<b>9</b>
<b>2</b>	<b>Nomenclature</b>	<b>11</b>
<b>3</b>	<b>Background</b>	<b>13</b>
3.1	Problem Motivation . . . . .	13
3.2	Computational State of the Art for Rotating Hub Analysis . . . . .	14
3.3	Computational State of the Art for Complex Unsteady Turbulent Wakes . . . . .	16
<b>4</b>	<b>Computational Objectives and Goals</b>	<b>19</b>
4.1	Objectives . . . . .	19
<b>5</b>	<b>Computational Methodology and Development</b>	<b>20</b>
5.1	Baseline Computational Methodology . . . . .	20
5.1.1	Grid Generation Approach . . . . .	20
5.1.2	Numerical Solver Description . . . . .	20
5.1.3	Advanced Turbulence Modeling: Hybrid URANS-LES Formulation . . . . .	21
5.1.4	Post Processing and Analysis . . . . .	24
5.2	Development of Overset Feature-Based Grid Adaptation . . . . .	26
5.2.1	Anisotropic Feature-Based Adaptation . . . . .	26
5.2.2	Extension to Overset Grids . . . . .	28
5.2.3	Time-Dependent Adaptation . . . . .	28
5.2.4	Method Validation . . . . .	29
<b>6</b>	<b>Hub Analysis and Deconstruction</b>	<b>47</b>
6.1	Experiment Description . . . . .	47
6.2	Grid and Run Option Descriptions . . . . .	49
6.3	Error Analysis . . . . .	52
6.3.1	Experimental . . . . .	52
6.3.2	Computational . . . . .	53
6.4	Static and Dynamic Force Correlations . . . . .	54
6.5	Drag Deconstruction . . . . .	56
6.6	Interference Drag . . . . .	67
6.7	Wake Characterization . . . . .	67
6.8	Velocity Frequency Spectra . . . . .	71
6.9	Reynolds-averaged Scaling Analysis . . . . .	74
<b>7</b>	<b>Scissors Configuration Analysis</b>	<b>75</b>
7.1	Hub Drag Loads Analysis . . . . .	76
7.2	Vibratory Loads Analysis . . . . .	77
7.3	Wake Velocity Correlations . . . . .	79
7.4	Wake Sensitivity to Averaging Sample Size . . . . .	85
7.5	Mean Velocity Trends . . . . .	87
7.6	Velocity Histograms and Central Moments . . . . .	89
7.7	Velocity Spectral Analysis . . . . .	103
7.8	Long-age Wake Analysis . . . . .	112
<b>8</b>	<b>Summary of Findings</b>	<b>115</b>

<b>9 Management</b>	<b>117</b>
9.1 Research Leveraging . . . . .	117
9.2 Technology Transfer . . . . .	117
9.3 Awards . . . . .	117
9.4 Publications . . . . .	117
9.5 Data Availability . . . . .	118
9.6 Training . . . . .	118
<b>10 Acknowledgments</b>	<b>119</b>
<b>11 References</b>	<b>120</b>

## List of Figures

1	Mean pressure coefficient along the centerline for the three-dimensional circular cylinder on several grids with varying turbulence methods. LES data is from Ref. 65, and experimental data is from Ref. 66. From 63. . . . .	21
2	Global index convention illustrated for an example overset grid system. . . .	28
3	Model of the GIT rotor-airframe configuration. . . . .	30
4	Contours along the airframe symmetry plane from the $k\omega$ -SST model. . . . .	31
5	Contours along the airframe symmetry plane from the HRLES model. . . . .	31
6	HRLES: time-averaged pressures on the top centerline from one adaptive cycle. . . . .	33
7	HRLES: time-averaged pressures on the top centerline from two adaptive cycles. . . . .	33
8	HRLES: top centerline instantaneous pressures (first-quarter revolution). . . . .	34
9	HRLES: top centerline instantaneous pressures (second-quarter revolution). . . . .	35
10	Vortex behavior (from top: initial grid, adapted to $ \omega $ , and <i>vorticity-mixed scheme</i> ). . . . .	36
11	Vortex behavior (from top: initial grid, adapted to $ \omega $ , and <i>vorticity-mixed scheme</i> ). . . . .	37
12	Vortex behavior (from top: initial grid, adapted to $ \omega $ , and <i>vorticity-mixed scheme</i> ). . . . .	38
13	Inviscid simulations: comparison of the <i>vorticity-mixed</i> and <i>Q-criterion-mixed schemes</i> . . . . .	40
14	HRLES: comparison of the <i>vorticity-mixed</i> and <i>Q-criterion-mixed schemes</i> . . . . .	40
15	Comparison of inviscid and viscous modeling of the flowfield for the <i>Q-criterion-mixed scheme</i> . . . . .	41
16	Vortex-trajectory comparisons from the <i>vorticity-mixed scheme</i> . . . . .	42
17	Pressure-integral functional convergence for the HRLES <i>vorticity-mixed scheme</i> adaptation sequence. . . . .	43
18	Computational model of the ROBIN 2MRTS configuration. . . . .	44
19	ROBIN sideline vortex trajectories at $\mu = 0.23$ . . . . .	45
20	Q-criterion iso-surfaces colored by vorticity magnitude for the ROBIN configuration at $\mu = 0.23$ . . . . .	46
21	Comparison of the computational (CFD) and experimental plugged geometries. The CFD geometries also include identification of components and orientation. . . . .	48
22	Hub model within John J. Harper wind tunnel test section. From Ref. 91. . . . .	49
23	Application of anisotropic grid adaptation for increased resolution of wake field . . . . .	50
24	Planform (looking down) view of the vorticity magnitude for the initial and adapted grid. . . . .	51
25	Left (looking forward) side view of the vorticity magnitude for the initial and adapted grid. . . . .	51

26	Comparison of power spectral density (PSD) predicted using two different time steps for the $Re = 0.29 \times 10^6$ rotating hub at $\mu = 0.152$ . The wake locations (1-4) correspond to Fig. 44. (Note: Data are presented using the final adapted grid.) . . . . .	54
27	Correlation between experimental load cell and CFD data for the $0^\circ$ static hub model . . . . .	55
28	Surface pressure coefficient distribution on the static and rotating rotor hub. Free stream flow enters normal to the figure. . . . .	56
29	Component drag contributions to global hub drag for static simulations. (Note: Reynolds numbers are abbreviated such that 'M' implies millions.) . . . . .	58
30	Component drag contributions to global hub drag for rotating simulations. (Note: Reynolds numbers are abbreviated such that 'M' implies millions.) . . . . .	58
31	Model scale ( $Re = 0.29$ M at $\mu = 0.152$ ) drag build-up due to sequential deconstruction. . . . .	59
32	Comparison of linear and CFD computed drag reduction due to hub components at $Re = 0.29$ M and $\mu = 0.152$ . . . . .	60
33	Total drag comparison at $Re = 0.29$ M and $\mu = 0.152$ . . . . .	60
34	Surface pressure contours at $Re = 0.29$ M and $\mu = 0.152$ . . . . .	61
35	Driveshaft slice locations at which pressure coefficient plots are investigated. . . . .	62
36	Definition of the driveshaft central angle $\theta$ with respect to circular components in the flow field. . . . .	62
37	Pressure distribution (top four slices) at $Re = 0.29$ M and $\mu = 0.152$ . . . . .	63
38	Pressure distribution (bottom four slices) at $Re = 0.29$ M and $\mu = 0.152$ . . . . .	64
39	Pressure distributions along slice locations (Fig. 35) illustrating component interference at $Re = 0.29$ M and $\mu = 0.152$ . . . . .	65
40	Map of PIV data collection plane comprised of overlapping stitches. From Ref. 91. . . . .	68
41	Comparison of experimental (PIV) and <i>a priori</i> computational data for the tunnel axis wake velocity deficit for $U_\infty = 8.941$ m/s. . . . .	69
42	Velocity contours one hub diameter downstream of the hub center for $U_\infty = 8.941$ m/s. . . . .	70
44	Wake hot-wire sampling locations. From Ref. 91. . . . .	71
43	Illustration of the wake extent (via vorticity contours) for the static at $45^\circ$ orientation (left), rotating (center) and $0^\circ$ static orientation (right) ( $U_\infty = 8.941$ m/s). . . . .	71
45	Power density spectrum of velocity fluctuations in the hub wake for the static hub at $0^\circ$ orientation at $U_\infty = 13.41$ m/s. . . . .	72
46	Power density spectrum of velocity fluctuations in the hub wake for the rotating hub at 240 rpm $U_\infty = 8.941$ m/s. . . . .	73
47	Top view of HRLES blending function contours. . . . .	73
48	Power density spectrum of velocity fluctuations in the hub wake for the rotating hub at 240 rpm at $U_\infty = 22.35$ m/s. . . . .	74

49	Hub configuration with and without scissors. . . . .	76
50	Comparison of unsteady drag coefficient ( $C_D$ ) harmonics for a rotating hub with scissors at 240 rpm. . . . .	78
51	Comparison of unsteady side force coefficient ( $C_y$ ) harmonics for a rotating hub with scissors at 240 rpm. . . . .	78
52	Q-criterion contours of the wake at $Z = 0.0$ m at 240 rpm. . . . .	79
53	Wake velocity measurement locations in space. (Red line indicates traverse of each profile). . . . .	80
54	Comparison of computational and experimental wake velocity profiles at one hub diameter in the wake. . . . .	81
55	Comparison of computational wake velocity profiles at one hub diameter in the wake. . . . .	82
56	Comparison of experimental data with different measurement technique and addition of scissors. . . . .	83
57	Overall comparison of both sets of CFD and experimental data. . . . .	84
58	Comparison of computational and <i>translated</i> experimental wake velocity profiles at one hub diameter in the wake. . . . .	84
59	Time-averaged wake velocity comparison at $Z = 0.0$ m illustrating the effect of number of revolutions on the averaging of the wake velocity. . . . .	86
60	Time-averaged wake velocity comparison at $Z = 0.0$ m at different downstream locations. The rotor hub conditions are at 240 rpm and $U_\infty = 8.941m/s$ . . . . .	87
61	Time-averaged wake velocity comparison at $Z = 0.0$ m at different downstream locations. The rotor hub conditions are at 240 rpm and $U_\infty = 13.41m/s$ . . . . .	88
62	Time-averaged wake velocity comparison at $Z = 0.0$ m at different downstream locations. The rotor hub conditions are at 240 rpm and $U_\infty = 22.35m/s$ . . . . .	88
63	Histogram comparison at $Z = 0.0$ m and $X = 1D$ . The rotor hub conditions are at 240 rpm and $U_\infty = 8.941m/s$ . . . . .	90
64	Histogram comparison at $Z = 0.0$ m and $X = 2D$ . The rotor hub conditions are at 240 rpm and $U_\infty = 8.941m/s$ . . . . .	91
65	Histogram comparison at $Z = 0.0$ m and $X = 3D$ . The rotor hub conditions are at 240 rpm and $U_\infty = 8.941m/s$ . . . . .	92
66	Histogram comparison at $Z = 0.0$ m and $X = 1D$ . The rotor hub conditions are at 240 rpm and $U_\infty = 13.41m/s$ . . . . .	93
67	Histogram comparison at $Z = 0.0$ m and $X = 2D$ . The rotor hub conditions are at 240 rpm and $U_\infty = 13.41m/s$ . . . . .	94
68	Histogram comparison at $Z = 0.0$ m and $X = 3D$ . The rotor hub conditions are at 240 rpm and $U_\infty = 13.41m/s$ . . . . .	95
69	Comparison of statistical central moments from adapted grid at $Z = 0.0$ m and $X = 1D$ . The rotor hub conditions are at 240 rpm and $U_\infty = 8.941m/s$ . . . . .	97
70	Comparison of statistical central moments from adapted grid at $Z = 0.0$ m and $X = 2D$ . The rotor hub conditions are at 240 rpm and $U_\infty = 8.941m/s$ . . . . .	98

71	Comparison of statistical central moments from adapted grid at $Z = 0.0$ m and $X = 3D$ . The rotor hub conditions are at 240 rpm and $U_\infty = 8.941m/s$ .	99
72	Comparison of statistical central moments from adapted grid at $Z = 0.0$ m and $X = 1D$ . The rotor hub conditions are at 240 rpm and $U_\infty = 13.41m/s$ .	100
73	Comparison of statistical central moments from adapted grid at $Z = 0.0$ m and $X = 2D$ . The rotor hub conditions are at 240 rpm and $U_\infty = 13.41m/s$ .	101
74	Comparison of statistical central moments from adapted grid at $Z = 0.0$ m and $X = 3D$ . The rotor hub conditions are at 240 rpm and $U_\infty = 13.41m/s$ .	102
75	Wake PSD comparison at $Z = 0.0$ m and $X = 1D$ . The rotor hub conditions are at 240 rpm and $U_\infty = 8.941m/s$ .	104
76	Wake PSD comparison at $Z = 0.0$ m and $X = 2D$ . The rotor hub conditions are at 240 rpm and $U_\infty = 8.941m/s$ .	105
77	Wake PSD comparison at $Z = 0.0$ m and $X = 3D$ . The rotor hub conditions are at 240 rpm and $U_\infty = 8.941m/s$ .	106
78	Wake PSD comparison at $Z = 0.0$ m and $X = 1D$ . The rotor hub conditions are at 240 rpm and $U_\infty = 13.41m/s$ .	107
79	Wake PSD comparison at $Z = 0.0$ m and $X = 2D$ . The rotor hub conditions are at 240 rpm and $U_\infty = 13.41m/s$ .	108
80	Wake PSD comparison at $Z = 0.0$ m and $X = 3D$ . The rotor hub conditions are at 240 rpm and $U_\infty = 13.41m/s$ .	109
81	Wake PSD comparison at $Z = -0.204D$ and $X = 1D$ at 240 rpm.	110
82	Wake PSD comparison at $Z = -0.204D$ and $X = 2D$ at 240 rpm.	111
83	Wake PSD comparison at $Z = -0.204D$ and $X = 3D$ at 240 rpm.	112
84	Wake spectra comparison at $Z = 0.0$ m and $X = 5D$ at 240 rpm.	114

## List of Tables

1	Predicted circular cylinder characteristics for various turbulence methods and grids with number of spanwise planes, $N_z$ , and spanwise extent, $Z$ . Separation location is given in degrees of azimuth from the leading edge stagnation point. From Ref. 63.	22
2	Blade angles and resulting thrust obtained for GIT test cases. (Note: All angles are reported in degrees.)	30
3	HRLES: summary of grid size resulting from the different adaptation schemes	32
4	Relevant parameters for the ROBIN wake visualization test case. (Note: All angles are reported in degrees.)	44
5	Effect of grid adaptation on the grid size.	52
6	Estimation of the error for some experimental parameters. From Ref. 52	52
7	Comparison of global (total) drag coefficient.	55
8	Drag tabulation for cylindrical components static azimuth orientations.	57
9	Average drag tabulation for rotating cylindrical components.	57
10	Full Configuration ( $Re = 0.29$ M at $\mu = 0.152$ )	66

11	Shanks Removed ( $Re = 0.29$ M at $\mu = 0.152$ ) . . . . .	66
12	Hub Removed ( $Re = 0.29$ M at $\mu = 0.152$ ) . . . . .	66
13	Links Removed ( $Re = 0.29$ M at $\mu = 0.152$ ) . . . . .	67
14	Matrix of flow conditions and analysis methods. . . . .	76
15	Drag coefficient comparison showing the effect of scissors at 240 rpm. . . . .	77

# 1 Summary

The drag due to the fuselage and hub constitutes a major portion of the overall drag of a rotorcraft. Indeed, “hub drag” (drag from the rotor hub, swashplate, blade actuators, hub pylons, engine nacelles and blade shanks), can constitute over ten percent of the total power required on typical helicopter designs, and over forty percent of parasite drag. On modern compound, high-speed or long-endurance rotary-wing vehicle concepts, increased complexity may result in the combination of the bluff body drag contributors, i.e., the hub and fuselage, becoming a primary limiter of performance. Prior to the commencement of this effort, the knowledge of where the state of the art in predicting this large drag contribution using computational fluid dynamics (CFD) methods was inadequate to predict whether a design for an advanced rotorcraft will be close to actuality, even when it is compared to one or two small-scale model experiments. An understanding of the various contributors to hub drag and their scaling with Reynolds number and other flight parameters, is critical to improving current designs, and to assessing new concepts.

The effort specifically involves fundamental research that systematically investigated the scaling of complex nonlinear effects such as bluff body separation and rotational/stationary interference effects on a generic hub configuration that included shanks, blocks, pitch links and scissors. The effort proceeded in two parts: an experimental investigation and a concurrent computational investigation. For all configurations, except where experimental wake data collection locations were not known, all computations were computed *a priori* to obtaining the experimental data. For the cases where the simulations could not be completed before the experiments, no manipulation of the simulations from the original protocol established occurred, ensuring *a priori* and independent correlation of the experiment and computations.

The primary objective of computational portion of this project was to reduce the uncertainty in current numerical predictions, through computational investigations that leveraged a Vertical Lift Consortium (VLC)-funded hub drag scaling research effort. To confirm this objective, correlations are performed with the results obtained during the experimental portion of this project. Experiments were performed on a 1/3.5 model scale experimental model, which included data from load cells, as well as selected wake measurements using a combination of particle image velocimetry (PIV) and hot-wire anemometry.

To achieve this objective, advanced turbulence methods based on a hybrid unsteady Reynolds-averaged Navier-Stokes/Large Eddy Simulations (URANS/LES) approach was applied. A new feature-based anisotropic grid adaptation, capable of grid modification on overset meshes has been developed, validated and demonstrated in this approach.

The objectives of the computational portion of this research were all met. CFD methods, using the approach developed, can be applied on a single baseline grid for a range of Reynolds numbers and operating conditions. This eliminates the need to generate grids to maintain accuracy in the near and far wake. Excellent correlation with experimental performance and wake characteristics were obtained using *a priori* simulations for the recommended approach. Computational analysis was also used to identify potential errors in the experimental data.

The hub characteristics were identified with computational methods for both full assembly

and deconstructions of the hub. From these, identification of where theoretical approximations can be applied were identified. Interference effects were also quantified, and the sources identified, including the influence of a fuselage. Strouhal shedding and wake interactions were computed from the rich data provided from the computational simulations. Important effects of scaling for both static and rotating hubs were quantified; it is clear that there are significant differences in the behavior of the hub and the component interference between model and full helicopter scales. This implies the critical need of advanced computational techniques such as the one developed here when designing and analyzing hubs. Long-age wake data were captured and correlated with experimental data from other sources to show that prediction and analysis of empennage-based aeroelastic and unsteady aerodynamic phenomena, such as tail buffet and “wag” arc within reach of current computational resources. Turbulent spectra confirmed the ability to maintain complex wake behavior over these long periods.

Computational methods have now reached a maturity that, if care is taken in the grid generation and turbulence modeling, it may be more cost-effective and accurate to design and analyze complex hubs directly with computational methods rather than reliance on model scale experiments. Advanced turbulence models that use detached or large eddy simulations and grid adaptation are recommended to improve the performance quantities and the unsteady wake characteristics.

## 2 Nomenclature

$a$	=	Speed of sound, m/s
$b$	=	Half chord length, m
$c$	=	Rotor blade chord, m
$c_p$	=	Pressure coefficient
$C$	=	Coarsening factor
$C_T$	=	Thrust coefficient $\left(\frac{T}{\rho\pi R^2(\Omega R)^2}\right)$
$C_\nu, C_\epsilon$	=	Coefficients used in LES $k$ equations
$f_{c_p}$	=	Time-averaged fuselage centerline pressure integral
$E$	=	Total energy, $(E = C_\nu T + u_k u_k / 2)$
$\mathcal{E}$	=	RANS statistical filtering operator
$\mathcal{F}$	=	LES statistical filtering operator
$F_{e,(-)}$	=	Adaptation formulation across an edge based on a solution feature
$F_{tol}$	=	User specified adaptation tolerance
$h$	=	Specific enthalpy
$h^0$	=	Original mesh spacing, grid units
$h_1$	=	New mesh spacing request, grid units
$H$	=	Hessian matrix
$\mathcal{H}$	=	Additive hybrid blending operator
$\mathbf{i}, \mathbf{j}, \mathbf{k}$	=	Cartesian unit vectors
$\hat{I}$	=	Adaptation intensity
$k$	=	Turbulent kinetic energy or reduced frequency
$k_{sgs}$	=	Subgrid scale turbulence kinetic energy
$l_e$	=	Edge length, grid units
$L$	=	Leonards' stress
$M$	=	Anisotropic adaptation metric or Stress term used in $C_\nu$
$M_{tip}$	=	Tip Mach number
$n$	=	Time step index within adaptation window
$n_1, n_2$	=	Node (1 or 2) of given edge
$N$	=	Number of time steps within adaptation window
$p$	=	Static pressure, N/m <sup>2</sup>
$Pr$	=	Prandtl number
$q_i$	=	Heat-flux vector $(q_i = -\kappa\partial T/\partial x_i)$
$Q_{crit}$	=	Q-criterion, s <sup>-2</sup>
$R$	=	Rotor radius, m, or gas constant
$Re_c$	=	Reynolds number based on blade chord and tip speed $\left(\frac{V_{tip}c}{\nu}\right)$
$s$	=	Instantaneous strain-rate tensor
$S$	=	Mean strain-rate tensor, s <sup>-1</sup>
$t$	=	Time, s
$T$	=	Rotor thrust, N

$u, v, w$	=	Instantaneous local velocity components in (x,y,z), m/s
$U_\infty$	=	Free stream velocity, m/s
$V_h$	=	Effective hot-wire measured velocity, m/s
$V_{tip}$	=	Rotor tip speed, m/s
$W$	=	Adaptation time window
$x, y, z$	=	Streamwise, spanwise and vertical directions, m
$\mathbf{x}$	=	Spatial vector, m
$y^+$	=	Nondimensional normal distance of the first cell from the wall

### *Greek Symbols*

$\beta_{1s}, \beta_{1c}$	=	Lateral and longitudinal first flapping harmonics
$\delta_{ij}$	=	Kronecker delta
$\Delta$	=	Characteristic length for grid scale
$\widehat{\Delta}$	=	Characteristic length for test scale
$\gamma$	=	Ratio of specific heats
$\kappa$	=	Coefficient of heat conductivity
$\mu$	=	Rotor advance ratio or coefficient of molecular viscosity, N·s/m <sup>2</sup>
$\mu_T$	=	Eddy viscosity nondimensionalized by $\mu$
$\nu$	=	Kinematic viscosity, m <sup>2</sup> /s
$\rho$	=	Density, kg/m <sup>3</sup>
$\psi$	=	Blade azimuth angle, °
$\tau$	=	Viscous stress tensor,
$\Omega$	=	Rotation rate tensor, s <sup>-1</sup>
$ \omega $	=	Vorticity magnitude, s <sup>-1</sup>
$\omega$	=	Specific turbulence dissipation rate or vorticity magnitude, s <sup>-1</sup>
$\Omega$	=	Rotational velocity of rotor, rad/s

### *Mathematics Symbols*

$\partial$	=	Partial derivative operator
$\overline{(\cdot)}$	=	Averaged value
$\widetilde{(\cdot)}$	=	Favre-averaged value
$\overline{(\cdot)}$	=	Variable filtered at test level
$(\cdot)^{SGS}$	=	Subgrid scale
$(\cdot)'$	=	Fluctuating value
$(\cdot)''$	=	Fluctuating Favre-averaged variable value
$(\cdot)_T$	=	Turbulent variable
$(\cdot)_\infty$	=	Freestream value

## 3 Background

### 3.1 Problem Motivation

Parasite drag on rotorcraft can become a crucial factor in forward flight especially during high speed flight<sup>1,2</sup> and can limit the range, maximum speed, and payload of the vehicle. Reduction in parasite drag can improve vehicle stability and control<sup>3</sup> and significantly decrease vibrational and blade loads to reduce vehicle weight and extend the rotor blade life.<sup>4</sup> Hub assemblies for single main rotor helicopters can contribute nearly 25%-30% of vehicle parasite drag, while hub assemblies for coaxial rotors, such as those on the XH-59,<sup>5</sup> can contribute as much as 50% of the parasite drag. The complex and highly turbulent rotor and hub wake is convected to the empennage and results in acroclastic behavior such as tail buffet and aerodynamic behavior known as tail “wag”. These phenomena result in fatigue and reduced handling qualities. Therefore, reduction of the drag in the design of hub systems can be critical to the success of high-speed rotorcraft design. In order to achieve these goals, the drag sources associated with complex hub designs must be thoroughly investigated, well understood, and reliably predicted using analysis tools.

There is a large literature base on flight to wind tunnel correlation of drag for fixed wing vehicles<sup>6,7</sup> preceding the establishment of cryogenic wind tunnels capable of separately or simultaneously simulating flight Reynolds and Mach numbers with sub-scale models. However, rotary wing designers must deal with aerodynamically dirty appendages and interference of rotating components, where the issue of drag is much more complex and significant.

Industry estimates that a thirty percent reduction in hub drag below the current empirical gross weight correlation is necessary for next generation vehicles. Present-day computational fluid dynamics (CFD) codes, especially commercial codes suitable for vehicle flow field-based drag analysis, are quite inadequate for drag prediction even at the conceptual design stage. This point is reinforced by a recent NASA/DFLR blind-prediction exercise on a relatively clean cargo aircraft configuration where some wing-root separation occurred at a lift coefficient of 0.5. This showed a wide scatter (over 23% uncertainty) in the drag polar predictions from 34 different CFD researchers,<sup>8,9</sup> when compared with experimental results. The cited causes for uncertainties are the lack of accurate methods for the prediction of separation on smooth aerodynamic surfaces, as well as the application of RANS-based turbulence models that are pre-tuned to a select set of test cases and may not be suitable for the physics of the configuration. While RANS turbulence models typically provide acceptable prediction of separation in the case of airfoil leading edge stall,<sup>10</sup> trailing edge stall mechanisms continue to elude capture via statistical modeling.<sup>11</sup> In the case of rotorcraft hub drag, several mechanisms of separation may be present leading to poor CFD results,<sup>12</sup> and the problem is complicated by a number of superimposed nonlinear concerns including, but not limited to incompressible flight regime, rotational downwash from the rotor, and transition from laminar to turbulent flow. Different CFD methods are unable to consistently capture these flows when applying the same RANS turbulence closures and inadequately comprehend the impact of scaling from model to full scale Reynolds numbers.

These inconsistencies and gaps in the known physics are not limited to numerical simu-

lations. Keys and Rosenstein<sup>11</sup> showed that at low advance ratio ( $\mu$ ), an increase in average shank dynamic pressure explains the drag increase. Wind tunnel tests on compound rotorcraft show large uncertainty in source and magnitude of “interference” drag (i.e., discrepancy between the sum of component drag values and the integrated powered vehicle drag), which must be understood to apply hub drag reductions consistently, especially during the reliance on smaller model-scale wind tunnel tests.

A typical hub is a plethora of interacting bluff bodies, which are associated with poor performance characteristics and higher drag. The primary drag component in these bluff bodies is due to flow separation (pressure drag) rather than viscous effects (friction drag). Bluff body wakes associated affect the performance of both commercial and military air vehicles,<sup>13</sup> in particular impacting tail component fatigue and handling qualities. Accurate hub drag predictions are inhibited by many differing complex flow interactions. Some hub wake characteristics include periodic forcing and vortex interactions. In many cases, these interactions originate from fine structures such as tubes, wires and linkages. The identification of the influence of the full assembly and component Reynolds numbers can not be minimized; over the Reynolds number range of interest, distinct bifurcations produce significant and measurable differences in the wake flow field.<sup>14</sup>

Much of the experimental research of hub drag is directed toward improving drag characteristics of current hub designs by the addition of fairings. Fairing designs have been explored by Sikorsky and others to reduce flow separation and interference drag between the hub and fuselage.<sup>5</sup> To date, frontal swept area of the hub design has been the leading parameter tied to hub drag,<sup>15</sup> therefore the fairing of an existing hub design does not address the issue directly. This is especially true for articulated hubs, where empty space is required for the control hinges, resulting in channel flows that interact with cylindrical components. While empirically corrected analytic estimates have been developed to predict hub drag based on frontal area, there is no consistent trend when accounting for interference effect and frontal swept area.<sup>16</sup> Considerations for hub displacement from the fuselage have been made, weighing the effects of increased frontal area to decreased interference.<sup>15</sup>

Based on these issues, this research was designed to aid in meeting the needs for both commercial and military next generation rotorcraft through the reduction of drag through the methodologies and results developed herein. Drag reduction is also a major goal of the DoD thrusts. This effort also is applicable to future vehicle derivatives and joint transport rotorcraft hub drag reduction. It can be applied directly on H-92, VH-92, S-92 Growth, S-76, X2 and V22 vehicles.

### **3.2 Computational State of the Art for Rotating Hub Analysis**

The portion of the research undertaken in this ONR-funded project reported here is on the computational prediction of complex hub performance and their turbulent wakes. Recently, there have been several fundamental experimental studies of hub drag, accompanied by state-of-the-art computational fluid dynamics (CFD) predictions of these complex flows.<sup>5,17-21</sup> These studies have all focused on models that are a fraction (1/5 - 1/4 scale) of the full-scale rotor hub. Thus, the scaling of these complex hub systems, including rotational and

interference effects, must also be understood.

Wake et al.<sup>5</sup> investigated 1/4-scale faired hubs for the X2 Technology<sup>TM</sup> Demonstrator aircraft using an unstructured computational solver. These simpler faired elliptical geometries can prove to be challenging because of the difficulty of predicting separation (and potentially transition). The focus of their effort was to investigate the impact of aerodynamic fairings on drag for the dual hub configuration. Using a grid refinement study, they were able to obtain agreement with experiment within 15% for their tetrahedral grids, within 3% for their hexahedral grids, and they matched within 8% the drag estimates obtained by two experimental studies for various configuration changes. The configuration that they analyzed was static and did not include components such as root stubs or hardware in the analysis. A follow-on study in 2011 by Sikorsky<sup>17</sup> using another unstructured method confirmed the overall findings of their initial undertaking. Similar issues have been recently encountered during another experimental-computational collaboration.<sup>21</sup>

Bridgeman and Lancaster<sup>18</sup> have studied a 1/5-scale Bell rotor hub and fuselage both experimentally and computationally. Using an extensive grid independence study, they found that total drag predictions within 5%-10% of experimental values using an unstructured state-of-the-art solver (FUN3D) could be achieved for the non-rotating hub-fuselage configuration, depending on the grid resolution. Details such as hardware, pitch links, and root stubs were included in the computational model; a breakdown of the individual contributions of these components was not part of the focus of this work. A follow-on effort citebell2 indicated that comparable results could be achieved by any of the unstructured solvers that were evaluated, including the solver utilized in this study. An extension to the methodology for rotating hubs was performed by Hill and Louis.<sup>20</sup>

Reich et al.<sup>21</sup> studied a notional rotor hub at 1/3 and 2/3 scale Reynolds number both computationally and experimentally at a single advance ratio of 0.2 in the Penn State University water tunnel. Measurements from experiment included total hub drag and wake diagnostics. Computations with a commercial code were also performed. They found that the most prominent wake structures were from the two-per-revolution (scissors) and four-per-revolution (main hub arms). Both of these vortical structures persisted far downstream of the hub, with the four-per-rev structure dissipating faster than the two-per-rev structure. Correlations with computations were not as accurate as the analyses performed by Bridgeman and Lancaster,<sup>18,19</sup> and the computations did not include turbulent wake spectra correlations with experiment.

For most of these simulations, existing unsteady Reynolds-Averaged Navier-Stokes (URANS) turbulence models or Detached Eddy Simulations (DES) were utilized to obtain the numerical simulation. Studies show that these URANS models are failing when the flow field includes viscous-dominated features, such as separation or vortex interactions. This poor correlation is not surprising, as the URANS models are statistical approximations of the turbulence scales. Large eddy simulation (LES) to direct numerical simulation (DNS) are needed to resolve the most energetic scales that dictate the behavior of vortex shedding and interaction encountered in these flows. LES is capable of capturing the larger eddies and models the smallest or subgrid-scale (sgs) eddies, permitting coarser grids than DNS,

which captures eddies of all sizes. Unfortunately, classic DNS and LES require significantly larger grids and more restrictive temporal step size to capture the most energetic turbulent features, which scale nonlinearly with increasing Reynolds number. Hybrid turbulence techniques have become an area of interest to close the gap between RANS and LES/DNS. Hybrid techniques in legacy CFD codes should capture the largest scales wherever grid resolution is sufficient to support LES. Thus even coarse grids, more suitable for Very-Large LES (VLES), should be more representative of the flow physics. Of these hybrid methods, the most well known is Detached Eddy Simulation (DES) typically applied with the Menter  $k$ - $\omega$  SST or Spalart-Allmaras URANS turbulence models. LES simulations occur in separated flows, following the Smagorinsky eddy viscosity assumption, while RANS turbulence modeling is applied in attached flows. Two recent Georgia Tech hybrid RANS/LES and VLES/LES turbulence simulation techniques have been implemented into the computational methodologies, OVERFLOW and FUN3D with good success on airfoils and rotors.

The approach in this effort is to integrate *a priori* computational predictions with experiments, so that the basic flow phenomena are carefully understood and the predictions are validated against experiment at the flow field phenomenon level, not just at the integrated performance level. This provides better confidence as the predictions are extended to other configurations and conditions than those in the validation experiment.

### 3.3 Computational State of the Art for Complex Unsteady Turbulent Wakes

The resolution of unsteady wake features is also essential for a multitude of aeroelastic applications pertinent to rotorcraft. These include, but are not limited to modeling of aeroelastic rotor blades in forward flight, rotor-fuselage or rotor-rotor interaction, helicopter-ship interaction, and tail buffet. Other applications of interest can include wing-store separation, ship-wake interactions, and wind turbines. The current most popular computational fluid dynamics (CFD) approach to resolve these multiple reference frame applications is via overset grids, where the moving body or component meshes are generally highly refined and overset on one or more static background grids.<sup>22-26</sup> Despite the ability of unstructured overset methods to model dynamic bodies, it does not address the issue of numerical dissipation that can result in inaccuracy of the wake physics.<sup>26,27</sup>

Feature-based grid adaptation for unsteady problems has been applied on single grids using various methodologies. Accurate predictions of hovering rotors in a single rotating adaptive mesh have been performed by several researchers.<sup>28-31</sup> However, these scenarios can not be immediately applied to the prediction of rotors in forward flight, where adaptation is needed in both the background inertial reference frame and the near-body rotating frame. Further, the interaction of rotors with non-moving bodies such as fuselages, wind-tunnel struts, and other configurational components also require moving-grid capability to simulate multiple motion frames. As an alternative to the overset configuration, Park and Kwon<sup>32</sup> have demonstrated an unstructured sliding mesh approach where a rotating grid communicates with a stationary background grid. Here, articulation of the rotor blades was

made possible using grid deformation based on a spring analogy, and also applies feature-based grid adaptation. Another non-overset based approach has been described by Cavallo et al.,<sup>33</sup> which uses unstructured grid movement and deformation to enable moving body adaptation.

Past research efforts in overset adaptation have in many instances relied on an off-body (background) Cartesian grid-based adaptive capability. Meakin<sup>34</sup> presented a grid component grouping algorithm with overset structured grids using a method of adaptive spatial partitioning and refinement and applied it to background Cartesian grids. Variations of this technique have been subsequently demonstrated by Henshaw and Schwendeman<sup>35</sup> and Kannan and Wang.<sup>36</sup> Canonne et al.<sup>37</sup> used an overset structured cylindrical grid topology to simulate rotor motion in hover where the background grid is adapted.

Hybrid-solver developmental efforts have focused on rotor methodologies where two separate solvers are applied in the near body and background regions, respectively. Duque et al.<sup>38</sup> have employed a structured near-body and unstructured wake grid approach to evaluate rotors. Here, isotropic adaptation was applied on the unstructured background grid operating in a non-inertial reference frame. This work recommended the use of anisotropic adaptation to accurately capture inherently anisotropic phenomena such as tip-vortices and to exploit computationally efficiency of this grid adaptation technique. Park and Darmofal<sup>39</sup> introduced a parallel anisotropic adaptation capability for non-overset tetrahedral grids. This technique has been applied to investigate several applications such as sonic-boom propagation,<sup>40,41</sup> viscous transonic drag prediction,<sup>40</sup> and re-entry vehicle configurations.<sup>42</sup> Recent development has focused on the coupling of a body-fitted unstructured solver with a high-order Cartesian solver to propagate the wake in the mid and far fields. Sankaran et al.<sup>43</sup> and Wissink et al.<sup>44,45</sup> have successfully implemented automatic mesh refinement (AMR) in the Cartesian background solver to resolve the wake based on flow field features.

The effect of time-dependency on the flow field is an essential aspect in applying grid adaptation to study dynamic moving bodies and their wake structure. Researchers<sup>33,37</sup> have shown that adapting the solution at a given frequency (based on flow time) have proven effective, with increasing frequency yielding higher accuracy. Investigations involving off-body Cartesian-based adaptive mesh refinement<sup>35,36,43-45</sup> have extended this rationale to adapt the solution a frequency comparable to that of the solver time step, allowing for a coupled adaptive flow solver. However, this capability is not computationally efficient for tetrahedral unstructured-based methods as they do not have the advantage of octree data structures to provide for the adaptive mechanics.

An alternative approach is thus required which addresses the time-dependency issue without the computational overhead of frequent adaptation. Kang and Kwon<sup>29</sup> present an adaptation technique that detects local maxima of a vortex core every five degrees and using a 3-D parabolic blended curve to represent the vortex core path. Park and Kwon<sup>32</sup> describe a 'quasi-unsteady' adaptive procedure for rotors in forward flight based on a time period or window dependent on the blade passing frequency. Cells satisfying an adaptation indicator are marked at each time step within the window and adaptation is performed for those cells at the conclusion of each window. Sterenborg et al.<sup>46</sup> describes a similar technique and applied

it for a fluid-structure interaction investigation. The extension of a time-dependent feature-based adaptation methodology for anisotropic grids involving dynamic bodies is delineated by Alauzet and Oliver.<sup>47</sup>

These successful implementations of grid adaptation provide impetus for further investigation of this approach for rotorcraft applications involving multiple grids. What is common across these prior overset-based efforts is that the adaptation is restricted to the off-body background meshes. Since vorticity originates on a viscous surface where the near-body grid is employed, the full capability of the adaptation cannot be exploited unless the adaptation can occur across the meshes. In addition, for rotorcraft configurations, a time-dependent strategy is necessary to permit accurate and efficient simulation of the wake growth.

## 4 Computational Objectives and Goals

The long range computational goals of this project is demonstrate the capability of computational methods (CFD) for use on hub and hub/fuselage design and analysis with high confidence. In addition, the ability to predict the complex wake structure for near and far wakes is needed to address other design and analysis issues on the helicopter.

### 4.1 Objectives

The objectives of the computational portion of the project, as outlined in the original proposal are:

1. Isolate and quantify the different sources of hub/pylon/nacelle drag.
2. Tighten the tolerances of upper-bound empirically-based computations suitable for conceptual design, by reference to the basic experiments.
3. Refine the capability to predict drag from first principles through computational aerodynamics, suitable for the preliminary design stage and beyond.
4. In the process, advance the state of knowledge on predicting flows around complex configurations involving flow separation from fixed and smooth surfaces, as well as a wide range of Reynolds numbers.

## 5 Computational Methodology and Development

### 5.1 Baseline Computational Methodology

The baseline grid and solver methodologies, prior to modification, are described here.

#### 5.1.1 Grid Generation Approach

NASA's VGRIDns grid generation software<sup>48</sup> was used to generate either fully tetrahedral or mixed element meshes for configurations studied. To perform a rotating simulation, meshes were overset to form a composite grid using SUGGAR++,<sup>49</sup> the overset assembly code documented in Section 5.1.2. The unstructured overset grid methodology allows for mesh refinement about complex shapes, and limits the number of overset meshes needed to perform the computation. For most of the configurations discussed in this report, comparisons were made with wind tunnel experiments, requiring the background grid to represent the tunnel test section.

Where ever possible, the viscous boundary layers of the components were modeled using prismatic elements, while the mesh surrounding the configuration was comprised of tetrahedral elements. This mixture of elements has been shown to accurately capture the behavior of the viscous boundary layer while minimizing the cells needed in the external flow field.<sup>50</sup> Based on prior experience with accurately predicting viscous effects,<sup>51</sup> between 30-50 normal mesh layers were used to model the boundary layers. The baseline mesh external to the boundary layer was generated with general wake refinement, such that a new grid adaptation strategy (Section 5.2) was used to modify the grid based on the specific flowfield.

Details of the hub model (including the bolt nuts, holes), the mount and the wind tunnel test section were included to correlate with the wind tunnel experiments.<sup>52</sup> The grid fidelity are further described in each individual geometry section.

#### 5.1.2 Numerical Solver Description

FUN3D, NASA's unstructured RANS solver, was selected as the flow solver with which to demonstrate the new adaptation strategy. FUN3D utilizes an implicit, node-based finite volume scheme to resolve the RANS equations on unstructured, mixed-topology grids.<sup>53</sup> Both compressible and incompressible<sup>54</sup> Mach regime capabilities are available in the flow solver. Time-accuracy is achieved using a second-order backward differentiation formula (BDF). Roe's flux difference splitting scheme<sup>55</sup> is used compute the inviscid fluxes, while an equivalent central difference approximation is utilized to resolve the viscous fluxes. A Gauss-Seidel strategy is used to solve the resulting linear system of equations. FUN3D has available a plethora of turbulence methods, of which Menter's  $k\omega$ -SST<sup>56</sup> two-equation model and a single-equation turbulent kinetic energy large eddy simulation (LES) model<sup>57,58</sup> were applied in this effort.

Overset functionality, which is essential to simulate grid motion of a rotating hub in the presence of a non-rotating test facility or fuselage, is achieved via two libraries, SUGGAR++ and DiRTlib. The Structured, Unstructured, and Generalized overset Grid As-

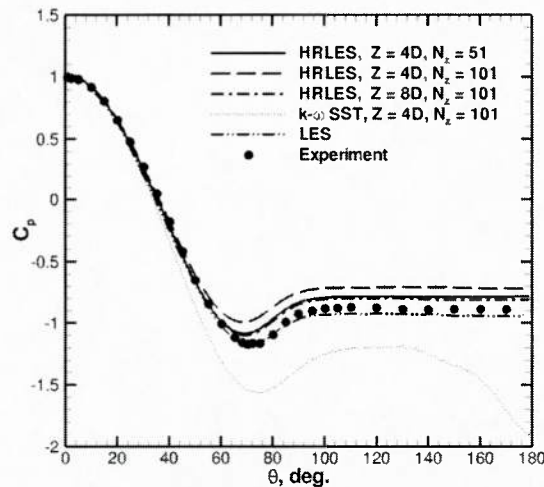


Figure 1: Mean pressure coefficient along the centerline for the three-dimensional circular cylinder on several grids with varying turbulence methods. LES data is from Ref. 65, and experimental data is from Ref. 66. From 63.

sembleR (SUGGAR++) code provides for Chimera of overset capability for structured, unstructured, and Cartesian grid topologies.<sup>49,59</sup> Its application is primarily for composite grid assembly for moving body simulations. The code is designed to perform as either a library or as a stand-alone executable catering to various grid formats. Composite grids can be created for both node and cell centered flow solvers. The code creates the composite grid along with a domain connectivity information (DCI) file. The DCI file contains information of the assembly of multiple overlapping grids via interpolation. It lists the locations of fringe points, where interpolation is required, as well as donor points that provide interpolation weights and the interpolated values at the fringe locations. Additionally, hole-cutting information and orphans (points lacking interpolation data) are documented in this file.

FUN3D's overset capabilities have been successfully applied to compressible and incompressible rotorcraft applications.<sup>60-62</sup> In such simulations, the background grid, which consists of the fuselage and other wind-tunnel static geometries up to the far-field boundaries, is assembled with finer near-body grids for each of the moving rotor blades.

### 5.1.3 Advanced Turbulence Modeling: Hybrid URANS-LES Formulation

A hybrid unsteady Reynolds-Averaged Navier-Stokes and large eddy simulation (URANS/LES) turbulence approach (GT-HRLES) within FUN3D<sup>63</sup> was used to obtain time-accurate evaluations of the unsteady hub wake. This turbulence approach has been shown to capture both attached and separated flows more accurately than URANS alone.<sup>63,64</sup> In particular, the separation location, wake properties and performance quantities of cylinders is comparable to LES results, and within experimental error bounds.<sup>63</sup> These are illustrated in Fig. 1 and Table 1.

$N_z$	$Z$	Turbulence model	Mean $C_D$	Strouhal no.	Separation location
–	–	Experiment <sup>67</sup>	$0.99 \pm 0.05$	$0.215 \pm 0.005$ <sup>68</sup>	$86 \pm 2^\circ$
101	$4D$	$k\omega$ -SST	1.456	0.213	$98.4^\circ$
2	–	DES	1.5	0.25	$86.8^\circ$
51	$4D$	HRLES	0.971	0.216	$85.8^\circ$
48	$\pi D$	LES <sup>65</sup>	1.04	0.210	$88.0^\circ$

Table 1: Predicted circular cylinder characteristics for various turbulence methods and grids with number of spanwise planes,  $N_z$ , and spanwise extent,  $Z$ . Separation location is given in degrees of azimuth from the leading edge stagnation point. From Ref. 63.

The hybrid URANS-LES approach<sup>57,58</sup> is a modeling strategy that extends a URANS approach, represented by the statistical operator  $\mathcal{E}$  and the LES approach represented on an explicit or implicit filtering operator  $\mathcal{F}$ . The approach relies on the introduction of an additive hybrid operator  $\mathcal{H}$  where  $\mathcal{H} = k_F \mathcal{F} + k_E \mathcal{E}$  with a constraint of  $k_F + k_E = 1$  for two blending factors,  $k_E$  and  $k_F$ , which may be functions of space and time. The constraint  $k_F + k_E = 1$  is very important as it imposes the preservation of the constants, which is a fundamental property necessary for an averaging operator. In this effort, the URANS model is the two-equation Menter  $k\omega$ -SST (shear stress transport) model<sup>69</sup> and the LES approach solves the  $k$  model. In the current hybrid RANS-LES approach,  $k_F = 1 - k_E$ , so that  $\mathcal{H} = (1 - k_E)\mathcal{F} + k_E\mathcal{E}$ .

Time or Reynolds-averaging provides the typical statistical operation for the URANS equations, but an LES approach requires a mass-time averaging or Favre filtering. The difference between these two averaging or filtering approaches is key to resolution of the turbulence in each approach. In URANS, the statistical operator,  $\mathcal{E}$ , resolves the turbulent velocity,  $u_i(\mathbf{x}, t)$ , into fluctuating and mean components,  $u_i(\mathbf{x}, t) = u'_i(\mathbf{x}, t) + \bar{u}_i(\mathbf{x}, t)$ , where, over a sufficient time period ( $t \gg t'$ ), the mean of the fluctuating velocity,  $\bar{u}'_i(\mathbf{x}) = 0$ . In LES, the spatial filtering operator  $\mathcal{F}$  separates the turbulent velocity into a large scale component and a small or sub grid scale (SGS) component. The SGS component,  $u'_i$ , differs from the Reynolds decomposition in that the filtered value of the SGS is not zero  $\bar{u}' \neq 0$ . Moreover, the LES filtered field is not idempotent ( $\bar{\bar{u}} \neq \bar{u}$ ), as is the assumption for the RANS statistical averaging. The fluctuating LES filtered terms are denoted with double prime notation ( $u''_i(\mathbf{x}, t)$ ) to differentiate the two quantities.

Consider the compressible conservation of mass, momentum and energy, which are given by

$$\frac{\partial \rho}{\partial t} + \frac{\partial}{\partial x_i} (\rho u_i) = 0 \quad (1a)$$

$$\frac{\partial \rho u_i}{\partial t} + \frac{\partial}{\partial x_j} (\rho u_i u_j) = \frac{\partial}{\partial x_j} (-p \delta_{ij} + \tau_{ij}) \quad (1b)$$

$$\frac{\partial \rho E}{\partial t} + \frac{\partial}{\partial x_i} (\rho u_i E) = \frac{\partial}{\partial x_i} [-q_i + (-p \delta_{ij} + \tau_{ij}) u_j] \quad (1c)$$

The set of equations given by Eqn. (1) is closed by specifying the equation of state  $p = \rho RT$ , where  $R$  is the gas constant.

For the hybrid RANS-LES formulation, the density, pressure, and heat transfer coefficients in the Navier-Stokes equations remain Reynolds-averaged, while the remaining variables are Favre- or mass-averaged to include compressibility effects. When the filtering operation is applied to the Navier-Stokes equations (and assuming that the filter commutes with the differentiation operator, which is strictly not correct), the general form of the LES equations can be obtained. Several fluctuating terms arise with the filtering, indicating that these are the turbulence terms that must be blended and switched between URANS and LES in different regions of the solution. These terms include the viscous stress tensor,  $\overline{\rho\tau_{ij}} = -\overline{\rho u_i'' u_j''}$ , and arising from the decomposed energy equation, the turbulent heat flux,  $q_i = \overline{\rho u_i'' h''}$ , and the rate of turbulent dissipation,  $\overline{\rho\epsilon} = \overline{\sigma_{ji} \frac{\partial u_i''}{\partial x_j}}$ . For simulations that encompass Mach numbers below the low supersonic regime, the molecular diffusion and turbulent transport terms are negligible and are typically not included, which is true here.

Closure for the viscous stress tensor is obtained from the Boussinesq approximation and is modeled using the typical eddy viscosity approach

$$\tau_{ij} = 2\nu_T S_{ij} - \frac{2}{3}k\delta_{ij} \quad (2)$$

where the eddy viscosity,  $\nu_t$ , is determined from the URANS and LES equations.

The Menter SST turbulence model solves two partial differential equations describing the turbulence kinetic energy  $k$  and the dissipation rate per unit turbulence kinetic energy  $\omega$ , which is then related to the turbulent characteristic length. These equations are

$$\frac{\partial}{\partial t}(\rho k) = \tau_{ij}^{RANS} \frac{\partial u_i}{\partial x_j} - \beta^* \rho \omega k + \quad (3a)$$

$$\begin{aligned} & \frac{\partial}{\partial x_j} \left[ (\mu + \sigma_k \mu_T^{RANS}) \frac{\partial k}{\partial x_j} \right] \\ \frac{\partial}{\partial t}(\rho \omega) + \frac{\partial}{\partial x_j}(\rho u_j \omega) &= \frac{\gamma \rho}{\mu_t} \tau_{ij}^{RANS} \frac{\partial u_i}{\partial x_j} - \beta \rho \omega^2 + \quad (3b) \\ & \frac{\partial}{\partial x_j} \left[ (\mu + \sigma_\omega \mu_t^{RANS}) \frac{\partial \omega}{\partial x_j} \right] \\ & + 2(1 - F_2) \rho \sigma_{\omega 2} \frac{1}{\omega} \frac{\partial k}{\partial x_j} \frac{\partial \omega}{\partial x_j} \end{aligned}$$

where the *RANS* superscript indicates a variable based on the Reynolds-averaged Navier-Stokes formulation that will be blended with its LES SGS counterpart to resolve the viscous stress tensor from Eqn. (2). There are a number of constants in Eqn. (3), which are defined as  $\beta^* = 0.09$ ,  $\sigma_k = 0.85$ ,  $\sigma_\omega = 0.5$ ,  $\sigma_{\omega 2} = 0.856$ , and

$$F_2 = \tanh \left\{ \left[ \max \left( \frac{2\sqrt{k}}{\beta^* \omega y}, \frac{500\nu}{y^2 \omega} \right) \right]^2 \right\} \quad (4)$$

where  $y$  is the distance to the nearest wall.

The turbulent kinetic energy production term  $k$  is computed in RANS models using either vorticity  $\Omega = \sqrt{\Omega_{ij}\Omega_{ij}}$  where  $\Omega_{ij} = \frac{1}{2} \left( \frac{\partial \bar{u}_i}{\partial x_j} - \frac{\partial \bar{u}_j}{\partial x_i} \right)$  or the strain rate  $S = \sqrt{2S_{ij}S_{ij}}$  where  $S_{ij} = \frac{1}{2} \left( \frac{\partial \bar{u}_i}{\partial x_j} + \frac{\partial \bar{u}_j}{\partial x_i} \right)$ . Spalart<sup>70</sup> noted that while vorticity has been more commonly applied in many RANS models, the actual physics of turbulence production are based on the strain rate. In the boundary layer the choice of vorticity or strain rate makes little difference, since the values are relatively comparable in that region. However, in other regions, such as wakes, where vorticity is much larger than the strain rate,  $k$  can be over predicted in a vorticity-based model. Menter's original formulation<sup>69</sup> in 1994 was based on the vorticity, but his more recent formulations<sup>71,72</sup> recommend a change to the strain rate.

Concurrent with the solution of the URANS turbulence model equations, a one-equation LES equation for the turbulent kinetic energy is also solved to determine the SGS values of the blended variables:

$$\begin{aligned} \frac{\partial}{\partial t} (\bar{\rho} k^{SGS}) + \frac{\partial}{\partial x_j} (\bar{\rho} \tilde{u}_j k^{SGS}) &= \tau_{ij}^{SGS} \frac{\partial \tilde{u}_i}{\partial x_j} - \\ C_\epsilon \bar{\rho} \frac{(k^{SGS})^{3/2}}{\Delta} + \frac{\partial}{\partial x_j} \left[ \left( \frac{\tilde{\mu}}{Pr} + \frac{\mu_t^{SGS}}{Pr_T} \right) \frac{\partial k^{SGS}}{\partial x_j} \right] & \end{aligned} \quad (5)$$

Here,  $C_\epsilon$  is a constant 0.916 and  $\Delta$  is the characteristic length given by  $\Delta = V_{cell}^{1/3}$  where  $V_{cell}$  is the cell volume (for the unstructured node-based solver, this is the dual cell volume). The SGS eddy viscosity is next computed from

$$\nu_T^{SGS} = C_\nu \Delta \sqrt{k^{SGS}} \quad (6)$$

where  $C_\nu$  is a constant value 0.0667.

#### 5.1.4 Post Processing and Analysis

Post processing of the data obtained during the different simulations utilize a number of different software. They include Tecplot<sup>73</sup> and Fieldview<sup>74</sup> for dynamic and static views of the flow field and surface behavior, and MATLAB<sup>75</sup> to extract and plot frequency data. Data and contour plots are presented throughout this report. In these plots, the following variable definitions were used:

$$\text{Pressure Coefficient:} \quad C_p = \frac{p - p_\infty}{0.5 * \rho * U_\infty^2} \quad (7)$$

$$\text{Q-criterion:} \quad Q_{crit} = \frac{1}{2} (||\Omega||^2 - ||S||^2) \quad (8)$$

$$\text{Vorticity Magnitude:} \quad |\omega| = \left[ \left( \frac{\partial w}{\partial y} - \frac{\partial v}{\partial z} \right)^2 + \left( \frac{\partial u}{\partial z} - \frac{\partial w}{\partial x} \right)^2 + \left( \frac{\partial v}{\partial x} - \frac{\partial u}{\partial y} \right)^2 \right]^{1/2} \quad (9)$$

$$(10)$$

Analysis of the computational data was performed to ensure that the minimum error resulting from numerical modeling is included in the data. In section 5.2.4, validation of the code modifications is discussed, along with verification of the simulations. Grid independence studies, within the scope of the changing scales of turbulence captured/modeled by the LES method, have been undertaken. Additional levels of grid adaptation on select cases were applied to discern their influence on performance and wake characteristics.

Statistical data analyses were also performed. Since the computational results cannot be performed for the large number of revolutions found in experiments, a moving window analysis was made on averaged data. Windows on the ultimate and penultimate revolutions were compared to ensure that the solution variable of interest was periodic or not changing; if not additional revolutions were simulated until this behavior was observed. The results were then averaged over a minimum of two revolutions to provide both means and unsteady bounds<sup>1</sup>. Care was taken in the analysis of periodic data to include a full cycle during the analysis to eliminate possible bias resulting from averaging.

For statistics resulting from a full revolution, an additional analysis for the Gaussian or normal distribution was computed to determine the repeatability of the unsteady quantities. Data lying outside the tenth and ninetieth percentiles were deemed as outliers. Details of these analyses are provided with the appropriate data results. The following definitions to compute the statistical quantities were utilized, with the MATLAB version R2013b function name included in parentheses:

$$\text{Mean (mean):} \quad \bar{x} = \frac{1}{n} \sum_{i=1}^n x_i \quad (11)$$

$$\text{Standard deviation (std):} \quad \sigma = \left( \frac{1}{(n-1)} \sum_{i=1}^n (x_i - \bar{x})^2 \right)^{0.5} \quad (12)$$

$$\text{Kurtosis (kurtosis):} \quad ku = \frac{E(x - \bar{x})^4}{\sigma^4} \quad (13)$$

$$\text{Sample Skewness (skewness):} \quad sk = \frac{\frac{1}{n} \sum_{i=1}^n (x_i - \bar{x})^3}{\frac{1}{n} \sum_{i=1}^n (x_i - \bar{x})^{3/2}} \quad (14)$$

Fast Fourier Transforms (FFT) were also computed to find the turbulence spectra of the data at specific points. For consistency, the FFT's were computed using the MATLAB<sup>75</sup> function, `fft`. This function (MATLAB version R2013b), uses the formulae based on the discrete FFT algorithm by

$$X(k) = \sum_{j=1}^n x(j) \omega_n^{(j-1)(k-1)} \quad (15)$$

---

<sup>1</sup>An unsteady bound should not be confused with an uncertainty or error bound. In highly unsteady flows, such as those encountered here, fluctuations in parameters are expected, and their quantification is useful in many engineering applications.

where

$$x(j) = (1/n) \sum_{k=1}^n X(k) \omega_n^{-(j-1)(k-1)} \quad (16)$$

and where  $\omega_n = e^{-2\pi i/n}$ .

## 5.2 Development of Overset Feature-Based Grid Adaptation

To help meet the objectives and goals of the computational portion of this research, a new adaptation strategy has been developed that permits time-dependent anisotropic adaptation for dynamic overset simulations. This strategy minimizes numerical dissipation and computational costs due to prohibitively large grid sizes. A clear advantage of this technique is that grids may be optimized for different flow conditions and geometric orientations without need to manually tailor the grid each time a new run condition is simulated. Previous numerical investigations<sup>5,76</sup> of hub drag have not examined the ability of grid adaptation to improve predictions of the loading or the flow features of the unsteady wake, and this is a new capability of direct use to the Navy.

The current development permits adaptation to be executed over a periodic time window in a dynamic flow field so that an accurate evolution of the unsteady wake may be obtained within a single unstructured methodology. Unlike prior adaptive schemes, this approach permits grid adaptation to occur seamlessly across any number of grids that are overset, excluding only the boundary layer to avoid surface manipulations. Using a rotor-fuselage interaction, flow field physics, time-averaged and instantaneous fuselage pressures, and wake trajectories have been computed and compared with experiment.<sup>77</sup> The ability of the methodology to improve these predictions without user intervention has been confirmed (see Section 5.2.4).

The ability to perform adaptive mesh *h-refinement* on a single grid is made possible by the refine library. Adaptive mesh refinement (AMR) can be performed via serial or parallel execution.<sup>39</sup> The application of this library, prior to this effort, has included sonic-boom propagation,<sup>40,41</sup> viscous transonic drag prediction,<sup>40</sup> and re-entry vehicle configurations.<sup>42</sup>

### 5.2.1 Anisotropic Feature-Based Adaptation

FUN3D's anisotropic tetrahedral adaptation capability<sup>39,78</sup> forms the basis for the new adaptation strategy. This feature-based adaptation requires the identification of a feature, as well as an algorithm or key to define the grid modification. In this effort, the indicators explored were vorticity, pressure difference, and the Q-criterion. The vorticity adaptation formulation,  $F_{e,|\omega|}$ , is similar to the one applied by Duque et al.,<sup>38</sup> which scales vorticity ( $\omega$ ) with an edge length,  $l_e$ . For a given edge connecting nodes  $n_1$  and  $n_2$ , the vorticity formulation is computed based on the averaged vorticity magnitude across the edge,

$$F_{e,|\omega|} = l_e \frac{|\omega|_{n_1} + |\omega|_{n_2}}{2}. \quad (17)$$

The pressure difference formula,  $F_{e,\Delta p}$ , was defined as the magnitude of the pressure difference  $\Delta p$  over an edge scaled by the edge length ( $l_e$ ) as

$$F_{e,\Delta p} = l_e |p_{n_1} - p_{n_2}|. \quad (18)$$

The formulation of the Q-criterion indicator is based on Kamkar's non-dimensional method<sup>79</sup> and uses the rotation rate ( $\Omega$ ) and strain rate ( $S$ ) tensors. Here the maximum value across the edge is applied,

$$F_{e,Q-crit.} = \max_{n_1, n_2} \left( \frac{1}{2} \left( \frac{\|\Omega\|^2}{\|S\|^2} - 1 \right) \right). \quad (19)$$

Using one of these formulations, the normalized local adaptation intensity,  $\hat{I}$ , is derived for each node as the maximum of the edge key,  $K_e$ , over all incident edges of a given node,

$$\hat{I} = \max_{edges} \left( \frac{K_e}{K_t} \right), \quad (20)$$

where  $K_t$  is a user-specified tolerance. The new isotropic mesh spacing is calculated using an estimate of the spacing on the original mesh  $h^0$ , a coarsening factor  $C$  (typically around 115%), and the adaptation intensity by,

$$h_1 = h^0 \min \left( C \left( \frac{1}{\hat{I}} \right)^{0.2} \right), \quad (21)$$

The power of 0.2 is an under-relaxation parameter that controls the aggressiveness of the refinement process. This parameter relates the convergence rate of error to the grid spacing for *adjoint-based adaptation*. The value of 0.2 (or 1/5) has been found sufficient since the convergence rates for *adjoint-based adaptation* are about  $O(h^4) - O(h^5)$ .<sup>80</sup> Although there is no formal connection to the local error estimates, this value has been typically chosen as a sufficient under-relaxation parameter for *feature-based adaptation*<sup>42</sup> utilized in this effort.

Consequently, an anisotropic adaptation metric may be derived using a scalar quantity for the isotropic spacing and a Hessian to stretch the resulting mesh. The Hessian of a quantity ( $-$ ) can be described as

$$H = \begin{bmatrix} \frac{\partial^2(-)}{\partial x^2} & \frac{\partial^2(-)}{\partial x \partial y} & \frac{\partial^2(-)}{\partial x \partial z} \\ \frac{\partial^2(-)}{\partial x \partial y} & \frac{\partial^2(-)}{\partial y^2} & \frac{\partial^2(-)}{\partial y \partial z} \\ \frac{\partial^2(-)}{\partial x \partial z} & \frac{\partial^2(-)}{\partial y \partial z} & \frac{\partial^2(-)}{\partial z^2} \end{bmatrix}. \quad (22)$$

Further details of the computation Hessian-based metric and its significance to the adaptation process are delineated in Ref. 78. The vorticity-based adaptation invokes the vorticity-magnitude Hessian to determine anisotropy, while the pressure gradient adaptation utilizes the Mach number Hessian, described in Ref. 42.

### 5.2.2 Extension to Overset Grids

The overset grid adaptation capability does not restrict adaptation to any component grid. This enables each grid to evolve independently and, in general, ensures for an orphan free composite grid. The current adaptation capability for viscous flows is restricted only to nodes beyond the boundary layer. FUN3D applies an adaptation software module that computes the adaptation metric as well as handles all associated adaptive mechanics. Description of the parallelized adaptation mechanics, which include grid operations such as node insertion and removal by splitting or collapsing edges, edge and face swapping, and node smoothing are detailed in Ref. 78. The extension of this method to include overset adaptation requires communication with DiRTlib,<sup>59</sup> the grid connectivity module, to assign a component mesh ID for each node in the composite mesh. The code performs adaptation over the entire composite grid system by tracking the component mesh ID for all added nodes.

Since overset assembly of the component meshes is handled by a library outside of the FUN3D framework (SUGGAR++),<sup>49</sup> a generalized global index convention was requisite so that subsequent assembly of the adapted grid with its domain connectivity information would be compatible with the solution information. This process is required to perform valid solution transfers between the unadapted and adapted grid systems. The convention requires both the flow solver and adaptation code to assign composite grid global indexes by arranging nodes in contiguous fashion by mesh ID over the list of component meshes. Nodes added due to adaptation are initially assigned new global indexes by appending them to the current global index list. Node removal results in unused global indexes, which is handled by a reverse, global-index shifting procedure. In order to satisfy the condition of contiguous mesh IDs, a new procedure was introduced to re-sort the global indexes of the adapted grid system as illustrated in Fig. 2. After adaptation, the component meshes are then saved, and the resultant domain connectivity information is obtained by invoking SUGGAR++ for subsequent grid assembly.

Mesh ID	Original Node Indexes	Updated Node Indexes	New Node Indexes	Mesh ID	Updated Node Shifted Indexes	New Node Shifted Indexes
1	1 2 <del>3</del>	1 2	14 15	1	1 2	3 4
2	4 <del>5</del> 6	3 4	16	2	5 6	7
3	7 8 9	5 6 7	17	3	8 9 10	11
4	<del>10</del> 11 12	8 9	18 19 20	4	12 13	14 15 16
5	13 14 15 <del>16</del> 17	10 11 12 13	21	5	17 18 19 20	21

(a) Node removal (struck through) and insertion      (b) Resorted global indexes

Figure 2: Global index convention illustrated for an example overset grid system.

### 5.2.3 Time-Dependent Adaptation

Time-dependent adaptation is obtained using a methodology based on that developed by Alauzet and Olivier.<sup>47</sup> The anisotropic grid metric is computed for every grid node at a

given time step and is progressively intersected over a selected time window such that the strongest restrictive metric at each node is retained to form the time-dependent grid metric. The Hessian,  $H$ , is intersected in time by collecting  $N$  solution samples within a time window  $w$  as given by,

$$|M_{w,max}| = \bigcap_{n=1}^N |M_{w,n}|. \quad (23)$$

Using the resulting metric, a new adapted mesh may be obtained suitable for multiple time intervals characterized by the flow phenomena obtained within the adaptive window. For rigid-body rotating systems, such a window can be identified as the time corresponding  $1/n_{blades}$  revolutions. The solution is sampled at each time step throughout the time window to obtain the metric intersection. The present approach does not utilize a solution transfer capability; hence, no additional interpolation errors are introduced and the inherent solver accuracy is retained as a result of re-simulation of the unsteady physics.

#### 5.2.4 Method Validation

The new overset anisotropic grid adaptation approach was validated using two cases: a rotor-fuselage interaction and a rotor wake.

##### *Rotor-Fuselage Interaction*

The Georgia Institute of Technology (GIT) rotor-fuselage interaction (RFI) configuration is comprised by a cylindrical fuselage and a hemispherical nose to permit easier identification of RFI has been extensively evaluated in the Harper Wind Tunnel.<sup>81</sup> The rotor blades have a rectangular planform with a NACA-0015 airfoil section. The rotor blades are nearly rigid which allow for CFD analyses that neglect structural deformations. Two advance ratios ( $\mu = 0.10$  and  $\mu = 0.20$ ) are selected for investigation and the relevant blade angles and thrust are reported in Table 2. Data from this effort include instantaneous and time-averaged pressures along the fuselage, as well as vortex behavior via laser light sheets. The fuselage length is non-dimensionalized ( $x/R$ ) by the rotor radius ( $R = 457mm$ ) for ease in presentation.

This model has been evaluated by numerous prior computational efforts with a variety of approaches, for example Refs. 22, 23, 82–84. O’Brien<sup>24</sup> used this as a validation case for his series of actuator to overset rotor models implemented into FUN3D. Numerous details of the time-averaged fuselage pressure coefficient have not been captured by these methods, in spite of the simplistic model geometry. O’Brien<sup>24</sup> noted that some time-averaged features just aft of the rotor were captured when the entire model (rotor strut and hub) were included, which prior efforts neglected. However, the vortex interaction observed in the original experiments near the nose ( $x/R 0.3$ )<sup>81</sup> has not been adequately resolved by any of these prior simulations.

Simulations were computed using the compressible, inviscid equation set as separation and other viscous effects should be minimal for the configurations chosen. Solution advancement was performed with a time step equivalent to  $1^\circ$  azimuthal sweep. During each time-step, 25 subiterations were used in conjunction with the temporal error control option

$\mu$	$\beta_{1s}$	$\beta_{1s}$	$C_T$
0.10	-2.02	-1.94	0.009045
0.20	-2.62	-3.29	0.009950

Table 2: Blade angles and resulting thrust obtained for GIT test cases. (Note: All angles are reported in degrees.)

to ensure one to two orders of magnitude reduction in residual. The metric intersection was performed over a time window corresponding to  $180^\circ$  blade sweep or 180 steps after the solution became periodic (after two revolutions). In order to obtain valid comparisons with experiment, the thrust values obtained for these cases were ascertained to be within 1% of those listed in Table 2.

A grid independence study on the fuselage mesh revealed very little variation in steady surface pressures. This evaluation was performed using the same near-body mesh for the rotor blades, consisting of 2.3 million nodes (13.5 million cells). The baseline fuselage (background) mesh consisted of 5.1 million nodes (30.2 million cells) – coarser meshes were not considered since grid resolution around the rotor-disk region needed to be maintained for spacing compatibility with the blade meshes. Steady state fuselage pressures on a refined fuselage mesh consisting of 9.6 million nodes (56.7 million cells) exhibited minor variation from the pressures of the baseline mesh. Grid convergence for the baseline mesh was, thus, established and its application for the full rotor-fuselage simulations was substantiated.

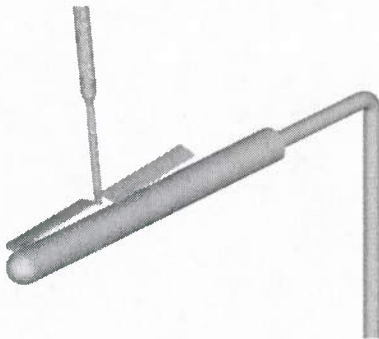


Figure 3: Model of the GIT rotor-airframe configuration.

Several feature-based adaptations were evaluated for the GIT RFI model to determine the validity of the method, as well as the appropriate flow field metric. The most accurate metric was determined to be a combination of the pressure gradient and vorticity for inviscid simulations. Details of this study can be found in Shenoy et al.<sup>77</sup>

The capability of this adaptation methodology to capture viscous flow phenomena was considered since this is important for the hub study in this effort. Two turbulence methods, the URANS model ( $k\omega$ -SST) and the HRLES model, were studied. Using a highly pre-refined composite grid (15.4 million nodes), where the background grid was refined in

the wake region between the blade and the fuselage, the effect of tip vortex dissipation was studied by applying both these turbulence models. The eddy viscosity and vorticity magnitude predicted using the  $k\omega$ -SST model and HRLES models are shown in Figs. 4 and 5, respectively. These figures depict the prediction at  $\psi = 120^\circ$ , but the same result is obtained at different blade azimuths.

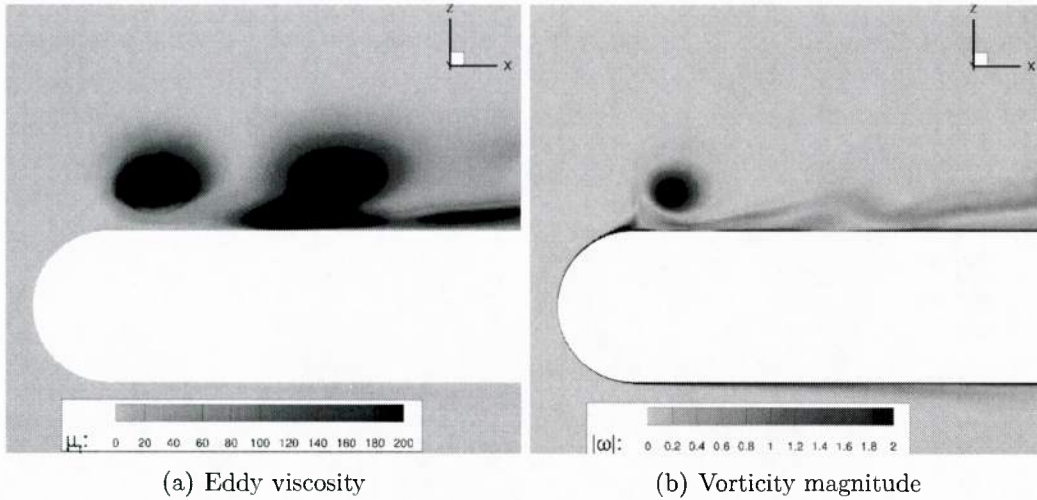


Figure 4: Contours along the airframe symmetry plane from the  $k\omega$ -SST model.

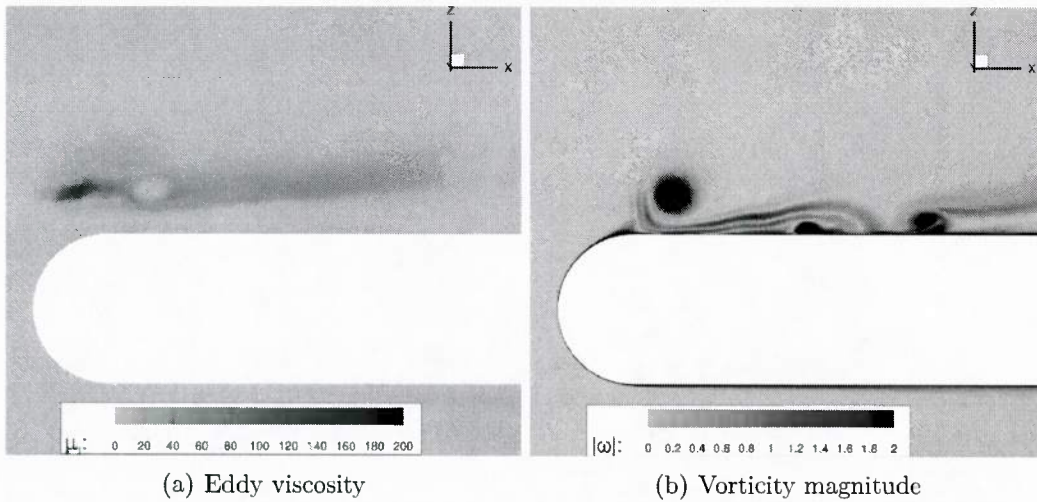


Figure 5: Contours along the airframe symmetry plane from the HRLES model.

Two observations can be made with respect to Figs. 4 and 5. First, the eddy viscosity prediction from the  $k\omega$ -SST simulation is significantly higher and widespread in the region coinciding with the forward tip vortex. The vortex also appears to be visibly diffused or

spread out in comparison to the HRLES simulation. Furthermore, the vortex core region of the HRLES simulation predicts significantly lower eddy viscosity, implying that this vortex core exhibits expected laminar behavior. The other observation is that the high eddy viscosity prediction from the  $k\omega$ -SST simulation that dominates the rotor wake region clearly diffuses the vortex propagating toward the fuselage following interaction with the oncoming blade. Additionally, rotor wake vorticity contours of the HRLES simulation show two distinct high vorticity regions that are characteristic of the expected vortex-fuselage interaction. This study demonstrates the superiority of the HRLES model in the preservation of the tip vortex and capturing a more complex interaction with the subsequent blade passage.

The initial grid used for the HRLES computations had the same pre-refinement in the rotor-wake region as in the inviscid simulations. The grid sizes resulting from the initial grid to the different feature-based schemes are listed in Table 3. Among the single adaptation schemes, adaptation to  $\Delta p$  was not considered because of its inability to preserve regions of high vorticity, which are essential in order to capture the magnitude of the fuselage surface pressures. The double adaptation schemes studied were the *vorticity-mixed scheme* and the *Q-criterion-mixed scheme*. The  $|\omega|$  (*iter. 2*) *scheme* was not performed because the inviscid simulations showed very little improvement from the single adaptation to  $|\omega|$ .

Table 3: HRLES: summary of grid size resulting from the different adaptation schemes

Scheme Description	Total Nodes (Millions)
Initial Grid	5.52
Adapted to $ \omega $	13.0
Adapted to Q-crit.	16.8
Adapted to $ \omega $ & $\Delta p$	24.2
Adapted to Q-crit. & $\Delta p$	30.7

Time-averaged fuselage pressures comparing the  $|\omega|$  and Q-criterion single adaptation schemes (Fig. 6) show very small differences, unlike the results from the inviscid simulation.<sup>77</sup> Both these schemes improve the magnitude of the pressures in the forward part of the fuselage ( $x/R \leq 0.3$ ), with exception to the nose region. Additionally, the primary vortex interaction resulting from both these schemes indicate the presence of a small pressure pulse at  $x/R \approx 0.5$ .

The *vorticity-mixed scheme* and *Q-criterion-mixed scheme* improve the accuracy of the time-averaged pressures (Fig. 7), particularly in predicting the intensity of the primary vortex interaction  $x/R \approx 0.5$ . Both schemes have clear similarities, but the *vorticity-mixed scheme* predicts a stronger pressure pulse than the *Q-criterion-mixed scheme*. Again, since the hub pin geometry is not modeled,<sup>85</sup> the HRLES simulations are not able to accurately predict the pressures in the aft portion of the rotor ( $x/R > 1.5$ ).

The instantaneous fuselage pressures, plotted in Figs. 8 and 9, show good correlation with experimental data at intermediate azimuths ( $\psi = 90^\circ - 150^\circ$ ) with both the *vorticity-mixed*

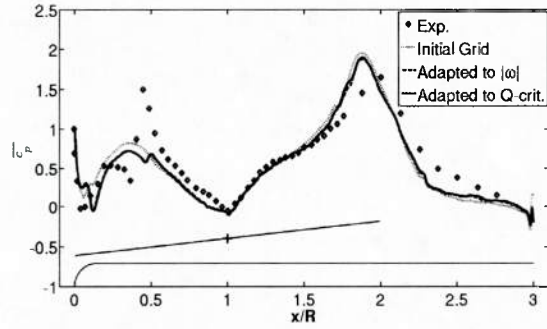


Figure 6: HRLES: time-averaged pressures on the top centerline from one adaptive cycle.

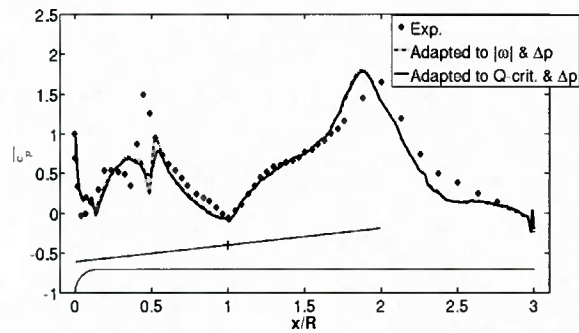
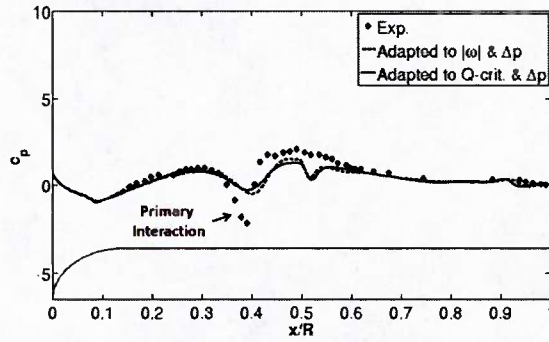
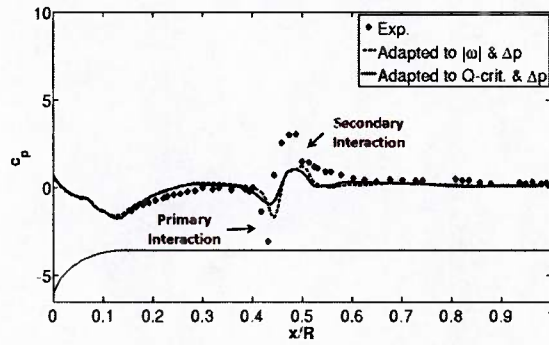


Figure 7: HRLES: time-averaged pressures on the top centerline from two adaptive cycles.

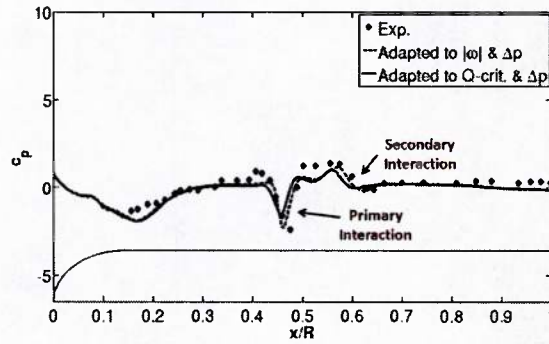
*scheme* and *Q-criterion-mixed scheme*. Both schemes agree very well with each other and the only difference observed is that the *vorticity-mixed scheme* predicts a higher magnitude of the primary vortex interaction. With respect to experiment, both schemes result in a small lead ( $\Delta x/R = 0.01$ ) in the spatial location for the primary vortex interaction. The magnitude of the interaction is under-predicted for the first quarter revolution and is over-predicted for the second quarter revolution. The secondary vortex interaction initially shows a slight lead in the spatial location ( $\Delta x/R = 0.05$ ), but during the second quarter revolution, this interaction lags behind the experiment by the same amount. The faster convection rate of the secondary vortex interaction is not captured. This may be attributable to boundary layer effects not being modeled as accurately either due to lack of adaptation or shortcomings of the turbulence modeling in this region. As with the inviscid simulations, the high pressure regions in the forward portion of the fuselage ( $0.2 \leq x/R \leq 0.5$ ) at  $\psi = 180^\circ$  do not correlate well.



(a)  $\psi = 30^\circ$

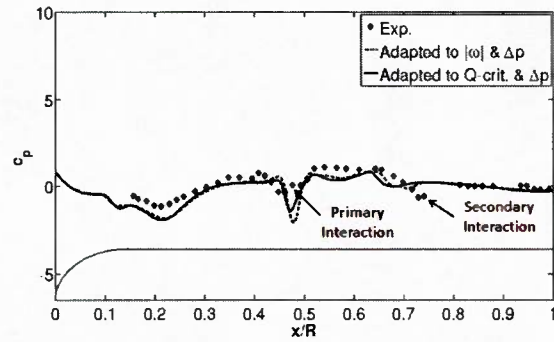


(b)  $\psi = 60^\circ$

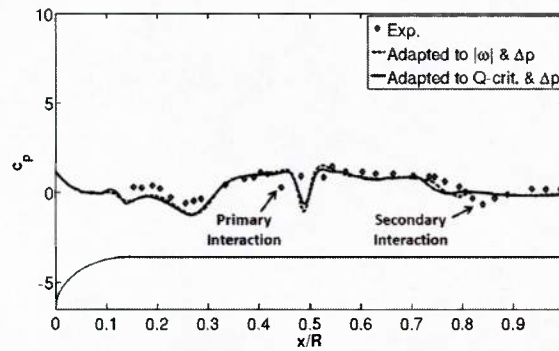


(c)  $\psi = 90^\circ$

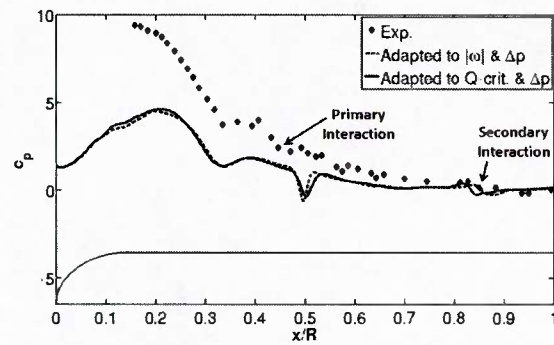
Figure 8: HRLES: top centerline instantaneous pressures (first-quarter revolution).



(a)  $\psi = 120^\circ$



(b)  $\psi = 150^\circ$



(c)  $\psi = 180^\circ$

Figure 9: HRLES: top centerline instantaneous pressures (second-quarter revolution).

To further understand the significance of the grid refinement in each scheme, the vortex behavior is examined in Figs. 10 – 12. The adaptation sequence from the initial grid to the *vorticity-mixed scheme* are plotted from top to bottom at each selected azimuthal location. Since the adaptation sequence leading to *Q-criterion-mixed scheme* show the similar results as with the *vorticity-mixed scheme*, they are not presented here. It is clear from scanning from top to bottom that the forward vortex core is more crisply predicted after the first

adaptation (middle plot) and refined further upon the second adaptation (bottom plot). In addition, the initially weaker vortical features in the rotor wake, diffused over large areas, become further defined due to adaptation.

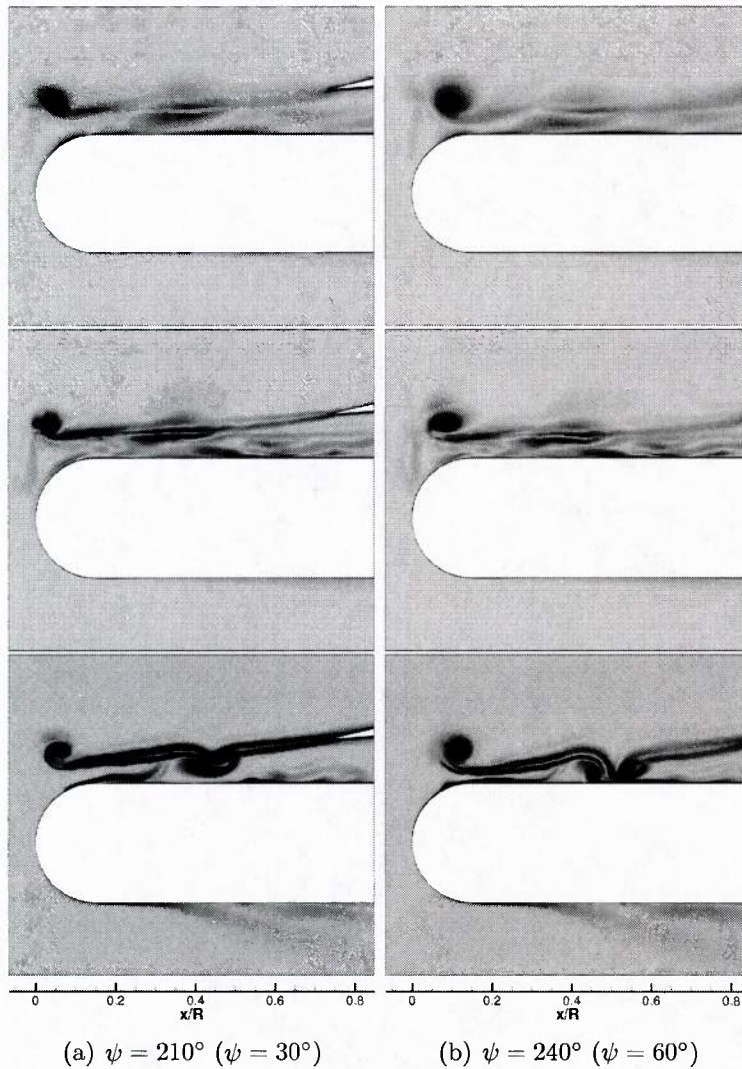


Figure 10: Vortex behavior (from top: initial grid, adapted to  $|\omega|$ , and *vorticity-mixed scheme*).

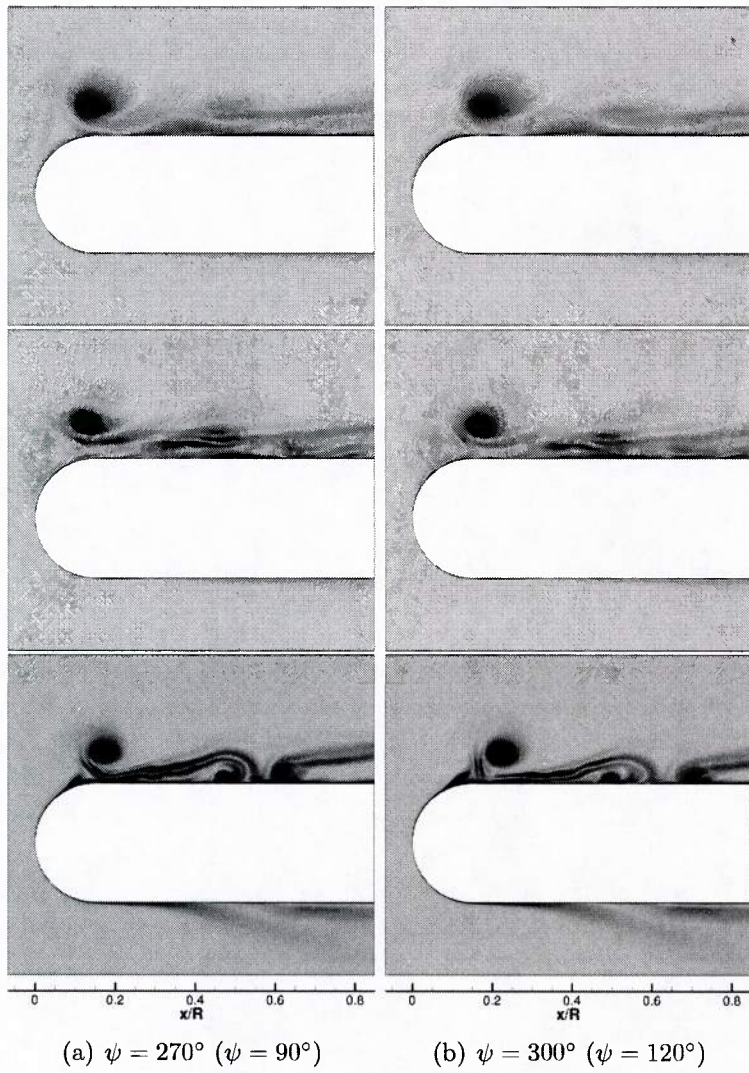


Figure 11: Vortex behavior (from top: initial grid, adapted to  $|\omega|$ , and *vorticity-mixed scheme*).

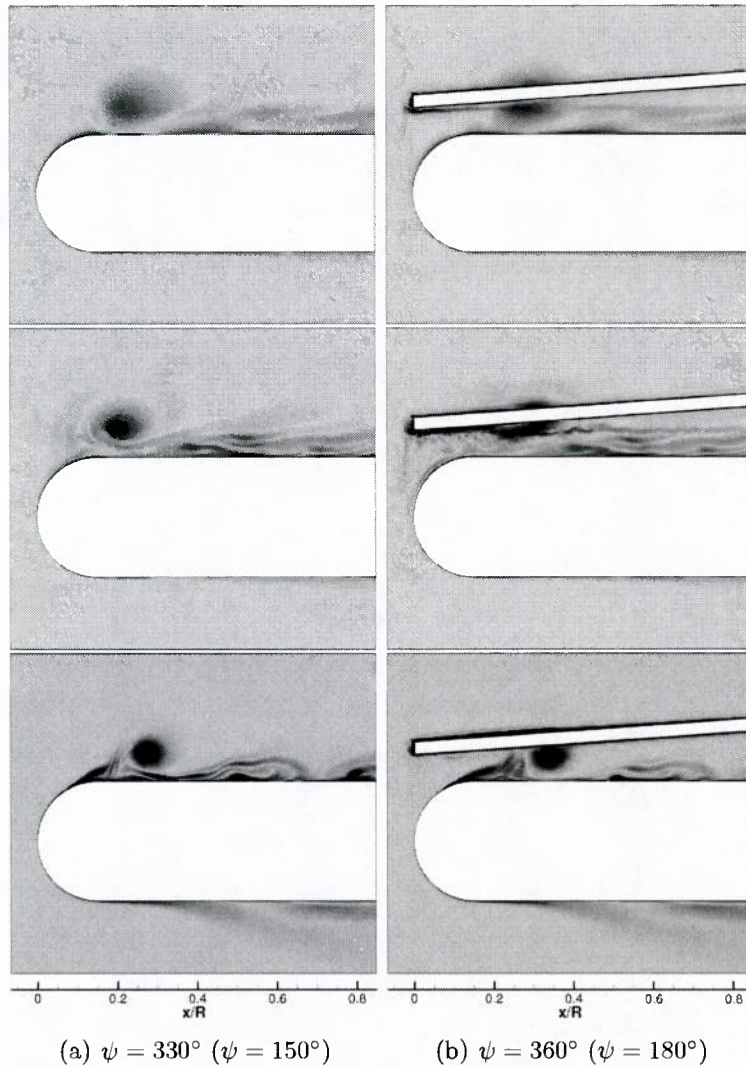


Figure 12: Vortex behavior (from top: initial grid, adapted to  $|\omega|$ , and *vorticity-mixed scheme*).

Differences between the various adaptation schemes can also be discerned from the magnitude and shape of the vorticity contours in these figures. For example, the shape of the vortex at  $0.4 \leq x/R \leq 0.5$  where the primary interaction occurs is very different. Specifically, tracing the *vorticity-mixed scheme* across Figs. 10 – 12, it is possible to discern the path of the tip vortex as it leaves the blade, interacts with the previous blade’s wake sheet, and finally collides with and encompasses the fuselage centerline. Brand<sup>81</sup> reported that the tip vortex from the prior blade interacts with the following blade at  $x/R = 0.3$  at  $\psi = 188^\circ$  (or  $\psi = 8^\circ$ ), which is comparable to the grid adaptation results in Fig. 12 (b). The weakening vorticity of the primary interaction, observed at approximately  $x/R = 0.45$  in Figs. 10 – 12, correlates to the experimental visualization. The vortex sheet roll-up, which was experimen-

tally observed to traverse in the range  $0.4 \leq x/R \leq 0.5$  during this azimuthal time period can also be observed traveling downstream at  $\psi = 210^\circ$  and with a distinct rotation by  $\psi = 240^\circ$ , located in the same fuselage locations. The development of the secondary vortex-fuselage interaction and its subsequent rapid downstream convection is also observed in the *vorticity-mixed scheme* and *Q-criterion-mixed scheme* (not shown).

A lack of agreement between the *vorticity-mixed* and *Q-criterion-mixed schemes* was observed in inviscid simulations<sup>77</sup> but not in the viscous simulations. The Q-criterion indicator formulation targets regions where the rotation rate  $\|\Omega\|$  dominates the strain rate  $\|S\|$ , since  $F_{tot} = 0.01$ . In regions where  $\|S\|$  exceeds  $\|\Omega\|$ , the Q-criterion (dimensional or non-dimensional) values are negative. Therefore such regions are not selected for refinement. The vorticity magnitude method, on the other hand, does not discriminate regions where strain rates dominate and its range is always non-negative.

Figure 13 illustrates the differences in the flow fields resulting from these schemes for the inviscid simulations. The vortex sheet region clearly displays uniformly high values of vorticity, but the values of Q-criterion in those regions are negative or very close to zero. Regions where both vorticity-magnitude and Q-criterion are high include the vortex core region and few localized regions in the vortex sheet. The fully turbulent flow fields resulting from these adaptation schemes is compared in Fig. 14. High values of vorticity throughout the vortex sheet are observed in Fig. 14 (a). In comparison to Fig. 13 (b), the vortex sheet in Fig. 14 (b), shows several more spots of positive Q-criterion values. Therefore, these regions in the vortex sheet are selected for refinement in the turbulent simulation and are excluded from refinement in the inviscid simulation. Since the adaptation metric is accumulated over  $180^\circ$  azimuthal sweep, the highly refined vortex sheet benefits the preservation of the tip vortex as it passes through these regions. Another difference between inviscid and turbulent simulations is that the latter exhibits an interaction with the rotor wake and fuselage boundary layer about the juncture of the hemispherical nose and cylindrical fuselage. This region indicates both high values of vorticity magnitude and positive Q-criterion. This behavior arises mainly due to the no-slip boundary condition of the turbulent simulations.

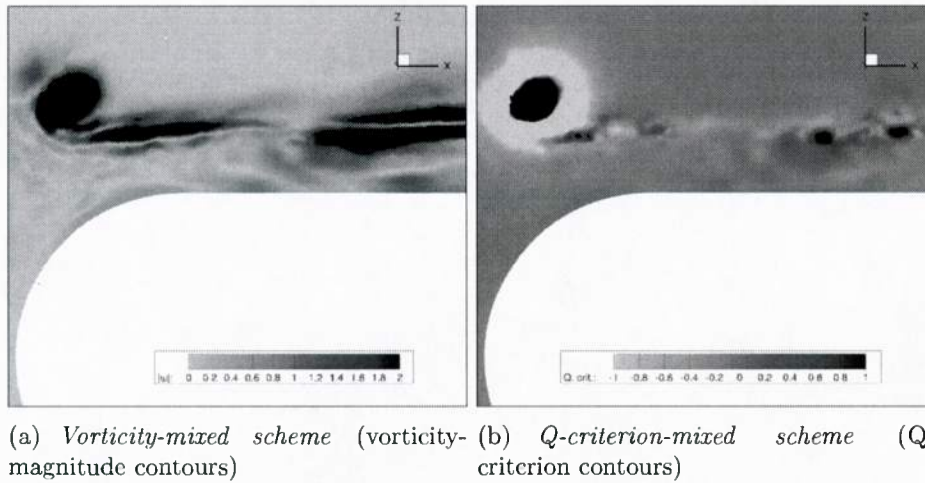


Figure 13: Inviscid simulations: comparison of the *vorticity-mixed* and *Q-criterion-mixed* schemes.

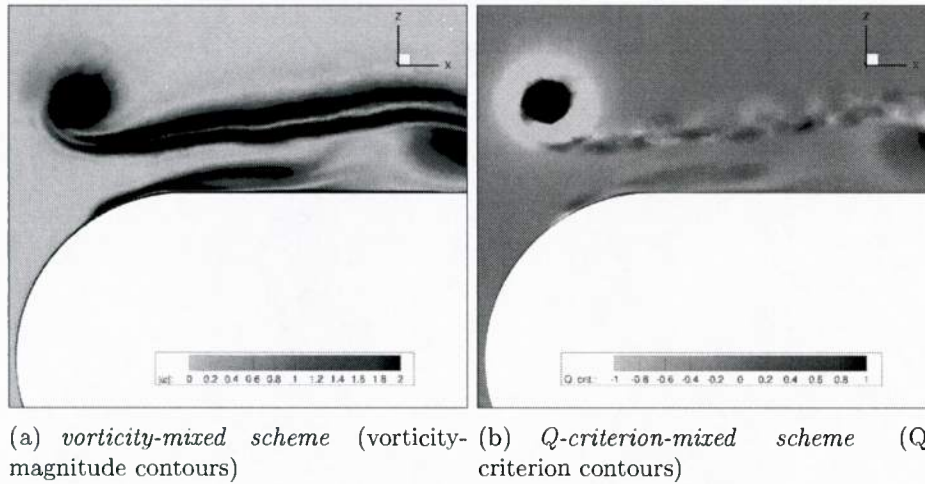


Figure 14: HRLES: comparison of the *vorticity-mixed* and *Q-criterion-mixed* schemes.

The genesis of positive  $Q$ -criterion values in the turbulent vortex sheet is explained by examining the flow field near the blade trailing edge in Fig. 15. The trailing edge region exhibits high  $Q$ -criterion values over a significant portion of the blade span for the turbulent simulation, absent from the inviscid simulation. This is attributed to boundary layer-trailing edge vortex shedding due to the blade's no-slip boundary condition.

Experimental visualizations document the tip vortex locations as soon as they become visible at  $\psi = 188^\circ$  and are plotted at  $30^\circ$  intervals until impingement with the fuselage in Fig. 16 (a). Vortex locations from the *vorticity-mixed scheme* resulting from both the inviscid and HRLES simulations, are shown in comparison to experiment. Figure 16 (b) plots

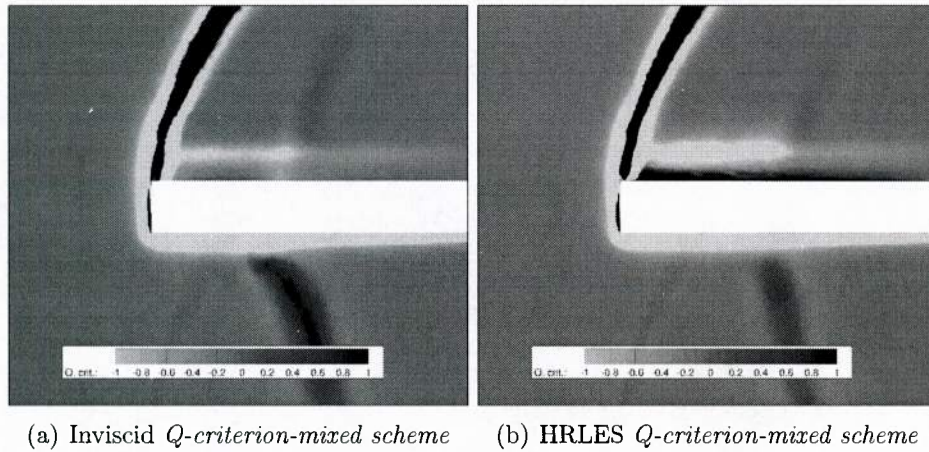
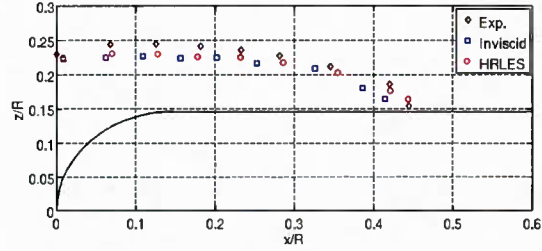
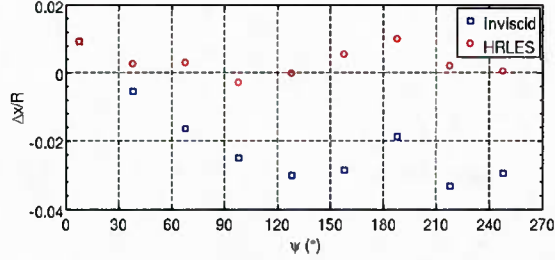


Figure 15: Comparison of inviscid and viscous modeling of the flowfield for the *Q-criterion-mixed scheme*

the streamwise spatial location lead (or lag) with respect to experiment. Both simulations show the same lead at the first vortex location. However, the inviscid simulation shows a vortex lag for the rest of the azimuthal locations, as high as  $\Delta x/R = 0.032$ . The HRLES simulation correlates much better with the spatial location, generally leading the experiment, with the maximum vortex lead of  $\Delta x/R = 0.013$ . This spatial lead is also observed via the surface pressures in Figs. 8 and 9. The uncertainty in the streamwise location reported with experiment was  $15\text{mm}$  or  $\Delta x/R = 0.033$ . Both simulations with the *vorticity-mixed scheme* are within the experimental error, but Fig. 16 (b) shows significantly better spatial correlation from the HRLES simulation of the vortex location with experiment.



(a) Vortex paths



(b) Streamwise location lead (positive) vs azimuth

Figure 16: Vortex-trajectory comparisons from the *vorticity-mixed scheme*.

The convergence of this feature-based adaptation process has been assessed by evaluating an integrated quantity of interest obtained over a series of adaptation cycles. Because the time-averaged pressure distribution has been previously applied as a suitability criterion of an adaptation scheme, the time-averaged centerline pressure integral is used here to identify convergence. The functional quantity is:

$$f_{\bar{c}_p} = \int_0^{3R} \bar{c}_p dx, \quad (24)$$

where the fuselage length is  $3R$ .

The convergence of the *vorticity-mixed scheme* has been assessed by performing an additional adaptation sequence, i.e. additional adaptations that include both  $|\omega|$  and  $\Delta p$ . The pressure integral is plotted in Fig. 17 for the *vorticity-mixed HRLES* simulation. Convergence is established for the four adaptation cycles since the change in the functional between cycles 3 and 4 is observed to be within 0.05%.

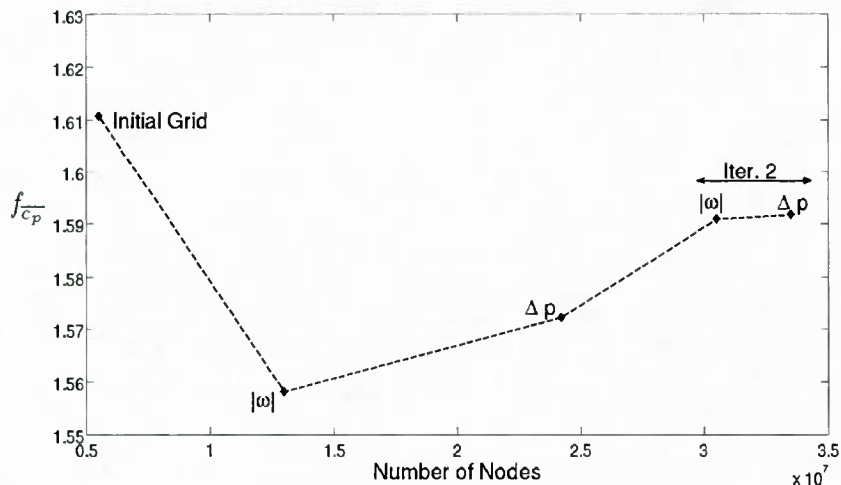


Figure 17: Pressure-integral functional convergence for the HRLES *vorticity-mixed scheme* adaptation sequence.

The efficacy of the overset, time-accurate grid adaptation capability has been demonstrated, but the solution dependency on the selection of the feature or combinations of features is clear. In addition, any uncertainty in the number of adaptation cycles suggests that a method to directly relate convergence to the functional of interest is required, such as adjoint-based adaptation. Adjoint-based adaptation has been demonstrated for steady, single grids by Park and associated authors.<sup>78,86</sup> The extension of adjoint-based adaptation capability to include overset, time-accurate simulations may be warranted and is being explored beyond this project.

### *Wake Prediction*

As this effort includes the analysis of rotor hub wakes, a second validation case that includes wake data was evaluated. The second validation case uses the Rotor Body Interaction (ROBIN) configuration, developed by NASA, which has been extensively used in various experiments and computational studies on rotor-fuselage interactions and wake trajectories.<sup>26,87-90</sup> This streamlined slender ROBIN fuselage model, described by a set algebraic equations at various fuselage locations, yields a simple analytical definition for a fuselage geometry. An engine mount or “doghouse” is a characteristic feature included in the configuration. An internally mounted rotor system is utilized consisting of four blades that are fully-articulated with a NACA-0012 airfoil section. The current effort focuses on the set of experiments conducted by Ghee and Elliott<sup>88</sup> in the 14-by-22-Foot Subsonic Tunnel at NASA Langley Research Center using the two-meter rotor test system (2MRTS). One of the experimental wake visualization cases (Table 4) was employed here to evaluate the influence of the adaptation process. Once again, the length data have been nondimensionalized by the rotor radius ( $R$ ) to facilitate ease in interpreting the simulations.

The compressible viscous option within FUN3D was applied to the ROBIN demonstra-

$\mu$	$C_T$	$\alpha_s$	$\beta_0$	$\theta_0$	$\theta_{1s}$	$\theta_{1c}$
0.23	0.0064	-3.0	1.5	6.5	-3.2	-1.1

Table 4: Relevant parameters for the ROBIN wake visualization test case. (Note: All angles are reported in degrees.)

tion. Similar to the GIT computations, the time step equivalency of  $1^\circ$  was chosen with 25 subiterations. Ten turbulence subiterations were also applied to converge the loosely-coupled Menter’s  $k\omega$ -SST turbulence model. Here the time window for the time-dependent metric corresponded to  $90^\circ$  blade sweep or 90 steps. Trim angles that were previously obtained on the same grid in Smith et al.<sup>26</sup> were used to estimate the required trim. The thrust values obtained were ascertained to be within 2% of the experimental values listed in Table 4, which validate the correlations with experiment without further trimming the rotor.

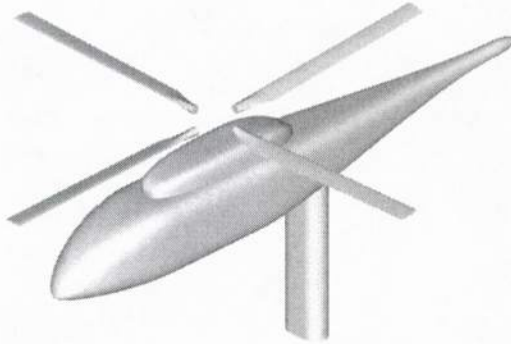


Figure 18: Computational model of the ROBIN 2MRTS configuration.

The purpose of this demonstration case was to examine the influence of grid adaptation on the prediction of the wake vortex trajectories. To examine this, a baseline grid wake trajectory was compared to a single adaptation based on vorticity magnitude. The application of only a single adaptation with the selection of the vorticity magnitude as the adaptation metric was based on the prior GIT RFI simulations for the range of experimental data available for correlation. The initial grid had 14.4 M nodes and the vorticity based adaptation increased the size to 17.6 M nodes.

Vorticity tracks were extracted at different longitudinal slices spanning the rotor disk. Vortex cores are determined by mapping local maxima of the normal vorticity component on each of these planes. There was no attempt made to differentiate individual vortex structures

like tip vortices from these contour maps. The wake trajectories for the advance ratio of 0.23 (Fig. 19) are observed to be very similar to the experiment and the baseline grid trajectories. The major influence of the grid adaptation was not readily transparent, as it was apparent primarily in the process through which the wake trajectories were numerically determined. As discussed with the GIT demonstration case, and illustrated here via  $Q$ -criterion plots (Fig. 20), the effect of the grid adaptation was to further refine the vorticity throughout the flow field. Thus, the refined strength and minimized extent of the vortex path rendered the wake tracking much simpler and with fewer approximations.

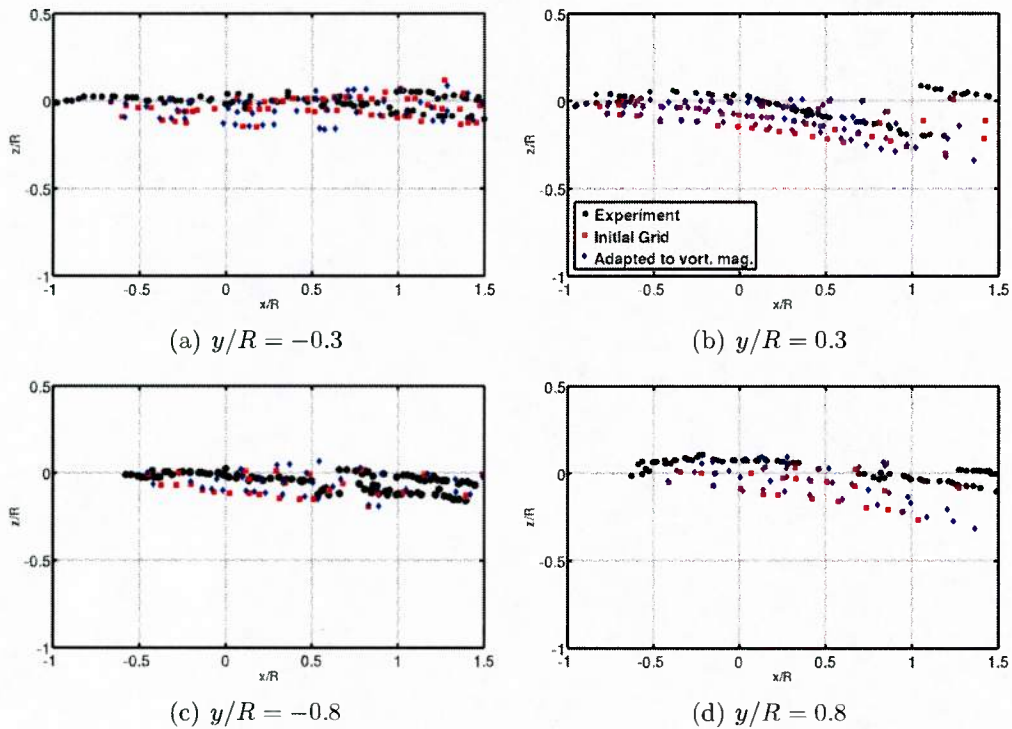


Figure 19: ROBIN sideline vortex trajectories at  $\mu = 0.23$ .

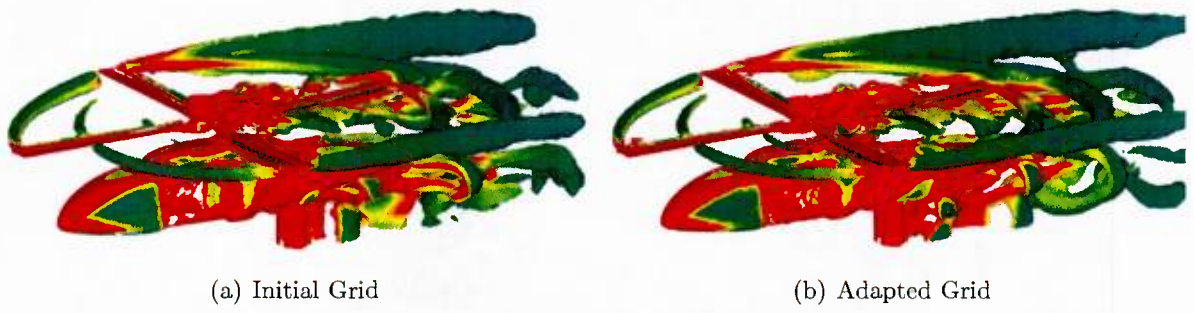


Figure 20: Q-criterion iso-surfaces colored by vorticity magnitude for the ROBIN configuration at  $\mu = 0.23$ .

## 6 Hub Analysis and Deconstruction

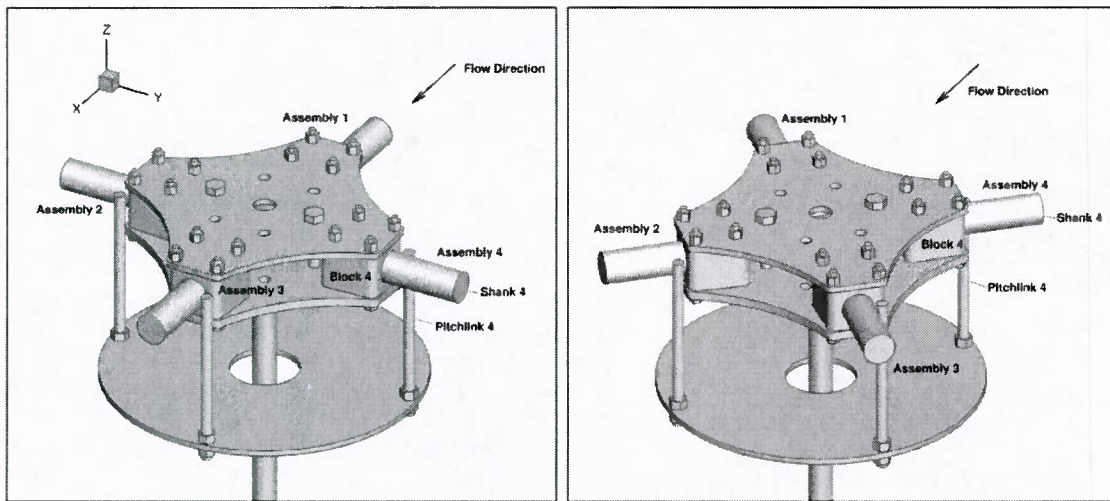
### 6.1 Experiment Description

Experiments on a generic four-bladed hub model were conducted in the John J. Harper low speed wind tunnel located within the Daniel Guggenheim School of Aerospace Engineering of Georgia Institute of Technology. A more complete detailed description with analysis can be found in Part 1 of this report.<sup>52</sup> The model (Fig. 21) is approximately one-quarter scale of a ten-ton helicopter. The complete model includes a number of geometric components found in a typical rotor hub: hub plates, blade shanks, swashplate, pitch links, drive shaft and requisite hardware (nuts, bolts, etc). A modified model, tested at the end of project in 2013, also added a scissors assembly, based on recommendations from industry. Some components found in full-scale rotors, such as hydraulic lines and control wire bundles, were not included in the model.

While there were different models with plugged and unplugged rotor shanks, only the plugged shank model was tested with rotation. A third configuration included plugged rotor shanks and closed the open region between the two hub plates (Fig. 21). A view of the experimental model and mount in the tunnel test section is illustrated as Fig. 22.

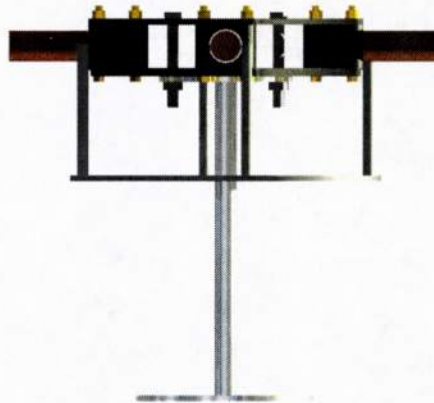
The experimental evaluation was initiated with static hub tests. Various azimuthal orientations at zero angle of attack were tested. Force data were obtained in  $15^\circ$  increments over a quarter revolution (since this is a four-bladed hub) for a range of available tunnel speeds. The plugged shank configuration was evaluated over the similar wind tunnel speed ranges and for rotation rates up to 240 rpm, and was the only configuration modeled computationally. In addition to the force measurements on the model, particle image velocimetry (PIV) and single axis hot-wire probes were applied at selected wake locations to measure the wake velocity and frequency spectra of velocity fluctuations, respectively.

Hub drag deconstruction was achieved experimentally by removing various components for selected static and rotating conditions. The drag was measured by removing the blade shanks, then the shanks and hub plates, pitch links, etc. until only the hub drive shaft remained.



(a) 0° azimuth view of the CFD model

(b) 45° azimuth view of the CFD model



(c) Side view of the experimental model (Ref. 91)

Figure 21: Comparison of the computational (CFD) and experimental plugged geometries. The CFD geometries also include identification of components and orientation.

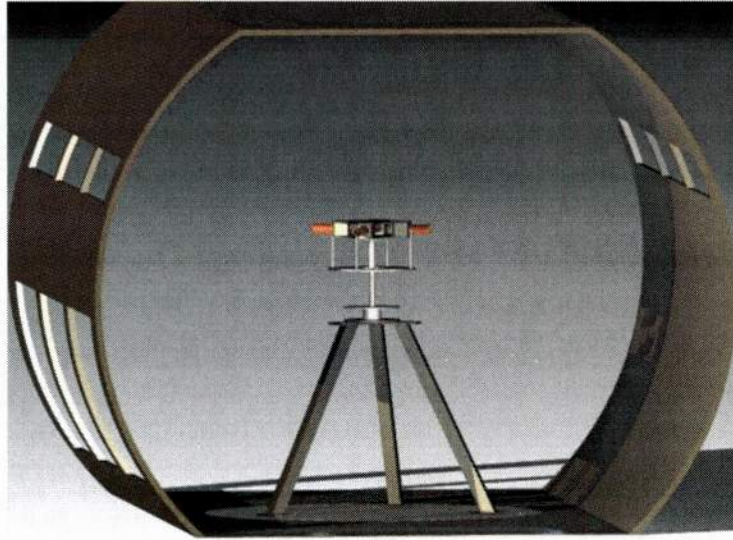


Figure 22: Hub model within John J. Harper wind tunnel test section. From Ref. 91.

## 6.2 Grid and Run Option Descriptions

Time-accurate predictions of the static hub and unsteady wake were simulated using the hybrid Reynolds-Averaged Navier-Stokes and large eddy simulation (RANS/LES) turbulence approach (GT-HRLES)<sup>92</sup> described in Section 5.1.3. The background grid included the wind tunnel test section (see Fig. 22), where the tunnel walls were modeled as inviscid surfaces. The wind tunnel mount, as well as details of the hub, including pitch links, bolts and nuts were included in the configuration, as previously illustrated in Figs. 21 and 22. Each component was identified in the simulations separately, which resulted in sets of integrated loads for each component, as well as the entire assembly. The ability to group and monitor the unsteady history of loads on various surfaces is beneficial in order to assess the drag predictions against theory and experiment.

A baseline overset grid of 11.1 million nodes was adapted using vorticity magnitude as the adaptation indicator. The boundary layer, consisting of 35 normal cell layers, had a maximum  $y^+ = 0.35$  for the reference Reynolds number of  $0.291 \times 10^6$ . An example of a grid before and after adaptation is illustrated in Fig. 23. The importance of the adaptation is emphasized in the shed vorticity of Figs. 24 and 25. The adapted grids provide significantly higher fidelity of the unsteady shed wake. This is particularly important in regions where the shed wake impacts on other hub components, as observed for the shed wake of the hub upstream of the main strut in Fig. 25. The initial and final adapted grid sizes for several of the cases examined computationally are listed in Table 5. Rotating hub adaptations resulted in larger overall grids than their static counterparts due to the larger extent of vorticity in the wake. Typically two adaptation cycles were required to result in drag changes of less than 1%, as documented by Shenoy et al.<sup>93</sup>

In addition to the basic computational options described in Section 5.1.2, there were several options that pertain specifically to the hub simulations. A dimensional time step (0.07 milliseconds) was selected to be equivalent to a one degree azimuthal sweep of the 240 rpm rotating hub. Using this time step, a fluid particle traverses the characteristic hub length in about 80 time steps. Each time step was augmented with an average of 25 Newton subiterations (up to a maximum of 40 subiterations) to increase the temporal accuracy of the simulation. A temporal error controller maintained a specific residual error so that the number of subiterations at each time step varies.

To mimic the turbulence intensity of the wind tunnel, a free stream turbulence intensity of 1% was applied to the simulation. This value was chosen based on prior-reported turbulence in wind tunnels of the same generation as the Harper wind tunnel. During 2012, there were major renovations to the wind tunnel, and it was reported that the wind tunnel turbulence intensity reduced to 0.03%. However, to maintain the correlations with the pre-renovation experiments, the original turbulence intensity was maintained. Simulations on similar complex configurations with both turbulence intensity levels did not result in observable changes in the parameters evaluated in this report.

The free stream density was assumed to be  $1.1901 \text{ kg/m}^3$  with a reference velocity of  $8.941 \text{ m/s}$ . With a shank-to-shank hub diameter of  $0.4862 \text{ m}$ , the Reynolds number was computed to be  $0.291 \times 10^6$ .

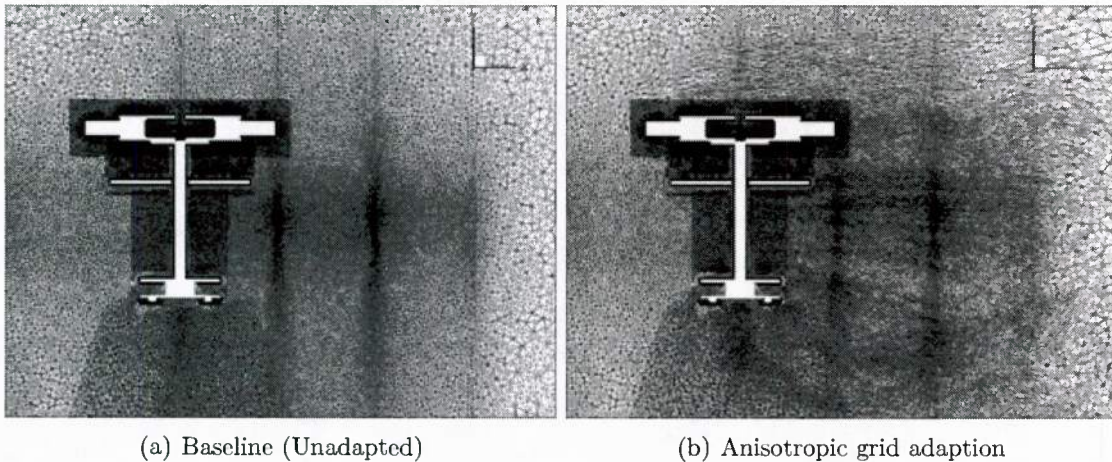
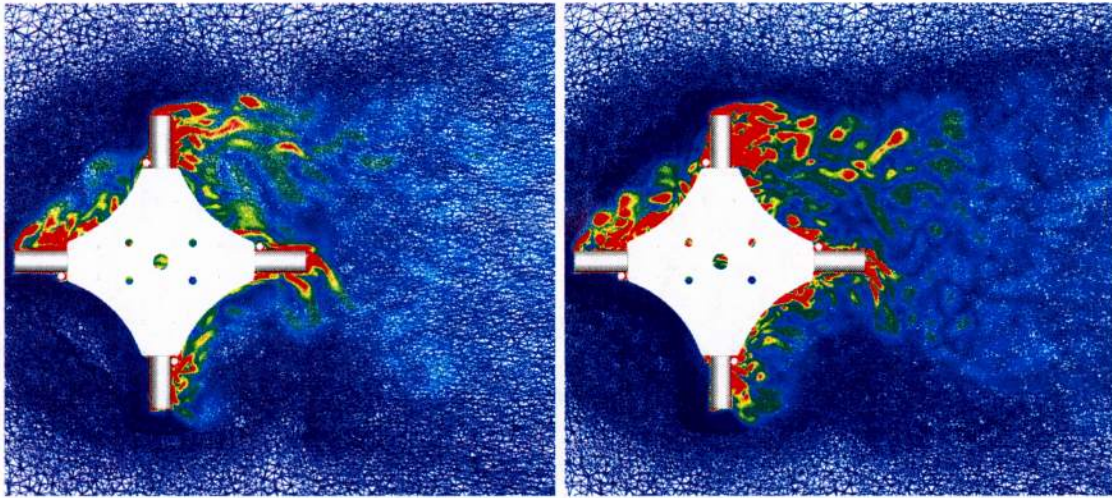


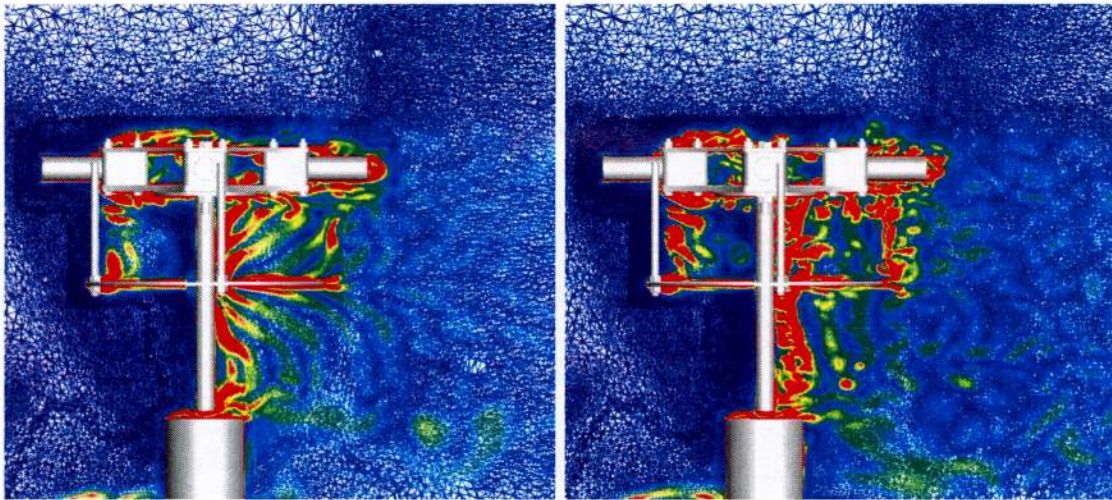
Figure 23: Application of anisotropic grid adaptation for increased resolution of wake field



(a) Initial rotating grid

(b) Adapted rotating grid

Figure 24: Planform (looking down) view of the vorticity magnitude for the initial and adapted grid.



(a) Initial rotating grid

(b) Adapted rotating grid

Figure 25: Left (looking forward) side view of the vorticity magnitude for the initial and adapted grid.

Test condition	Initial Grid	Adapted
Static hub at 0° orientation ( $U_\infty = 8.941$ m/s)	11.1 M nodes	15.8 M nodes
Static hub at 45° orientation ( $U_\infty = 8.941$ m/s)	11.1 M nodes	16.0 M nodes
Rotating hub at 240 rpm ( $U_\infty = 8.941$ m/s)	11.1 M nodes	19.5 M nodes
Static hub at 0° orientation ( $U_\infty = 13.41$ m/s)	11.1 M nodes	20.9 M nodes (2 iterations)
Rotating hub at 240 rpm ( $U_\infty = 13.41$ m/s)	11.1 M nodes	29.0 M nodes (2 iterations)
Rotating hub at 240 rpm ( $U_\infty = 22.35$ m/s)	11.1 M nodes	28.9 M nodes (2 iterations)

Table 5: Effect of grid adaptation on the grid size.

### 6.3 Error Analysis

With any investigation, there are errors associated with both experimental and computational efforts. Errors should be quantified and, if possible, minimized prior to analysis of data. An assessment of both the experimental and computational errors are addressed to provide a reference point for these and future analyses.

#### 6.3.1 Experimental

Experimental errors associated with the apparatus have been defined in the experimental portion of this report.<sup>52</sup> In addition to the documented vendor errors, there are other errors associated with the experiment. These are primarily based on human-related errors that can influence the measurements. These errors may include, but not limited to, issues with calibration of the equipment before and after the test, measurement of the locations where the wake measurements were taken, data reduction errors (associated with approximations), and setting/transcription of the experimental operational conditions (temperature, pressure, velocity, and their fluctuations during the test). Their estimates of some of the errors are shown in Table 6.

Parameter	Error Estimate
Dynamic Pressure	0.02%
Dynamic Viscosity	0.01%
Density	0.03%
Velocity	0.03%
Load Cell Calibration	1.37%
Calibration	0.77%
Temperature variation	0.45%
Approximation	0.43%
Ambient pressure	0.03%

Table 6: Estimation of the error for some experimental parameters. From Ref. 52

### 6.3.2 Computational

Numerical errors fall into two major categories: truncation errors and floating point precision errors. The former are primarily defined in the development of the computational technique, although they can be minimized with a refined isotropic grid. The second is associated with the computation itself.

The use of the feature-based overset grid adaptation aids to minimize these errors as the spatial grid is refined in the area where the maximum changes (and hence the largest gradients) occur in the flow field. To minimize these errors, grid adaptation was performed until the primary parameters of interest (hub drag, as well as velocities and turbulent spectra at specified wake locations) do not change within a defined tolerance. Examples with the hub drag error minimization are provided as part of this report. Since the turbulent wake is modeled with the large eddy simulation approach, grid refinement will result in the capture of more of the turbulence scales. Thus, changes in the wake behavior will change until the grid has been minimized such that all of the turbulent scales that contribute to the parameter evaluated have been captured. This is a direct relation to the tolerance chosen to define convergence.

Associated with the temporal integration are both truncation errors and floating point precision errors. In order to minimize computational times, most unsteady computational methods, including FUN3D, apply implicit time integration (specifically here the backward difference formulation). Convergence of the time step is demonstrated in Fig. 26, where the time steps studied corresponded to  $0.5^\circ$  ( $\Delta t = 0.3472 \times 10^{-3}$  s) and  $1^\circ$  ( $\Delta t = 0.6944 \times 10^{-3}$  s) azimuthal sweeps. Prediction of the 4/rev (16 Hz) and 8/rev (32 Hz) features that are prominent at these wake locations is insensitive to time step refinement (Ref. 91). Further, for frequencies higher than 100 Hz, a broad spectrum of scales is present showing evidence that the turbulence model is operating in LES mode. Based on these assessments, the dimensional time step was selected to be equivalent to a  $1^\circ$  azimuthal sweep of the rotating hub for all simulations. Up to forty subiterations were required to achieve time accuracy through residual reduction by two orders of magnitude during each time step.

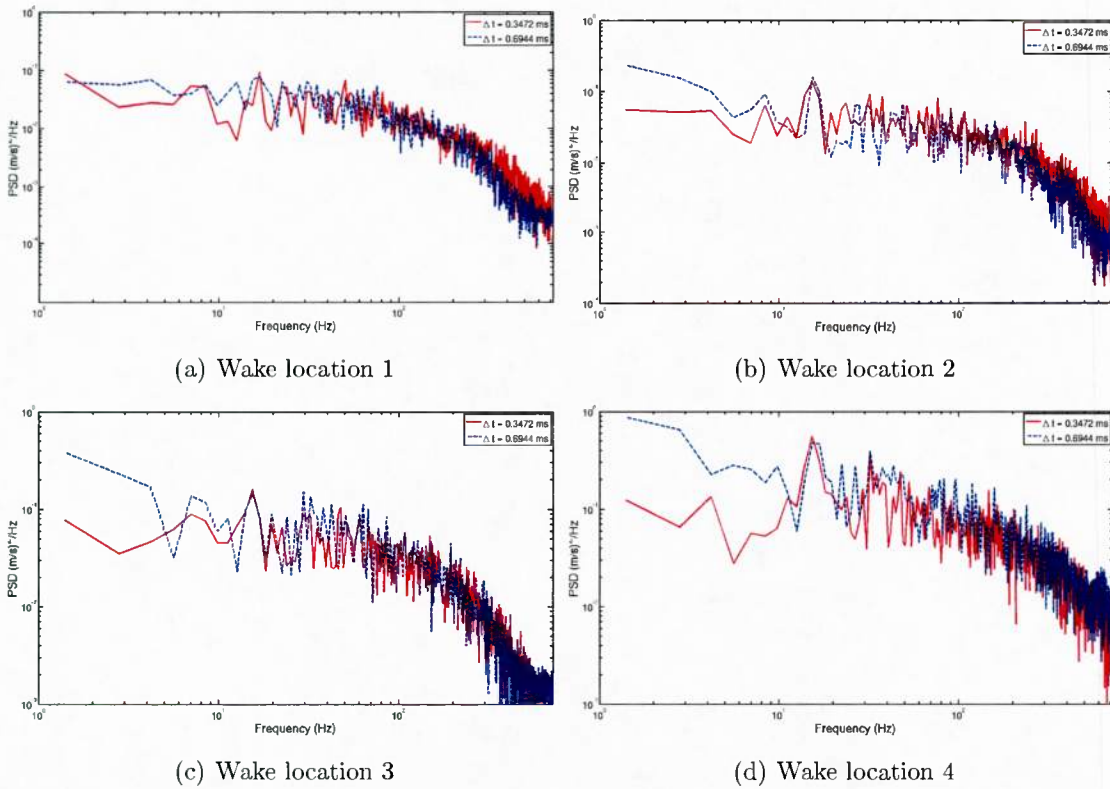


Figure 26: Comparison of power spectral density (PSD) predicted using two different time steps for the  $Re = 0.29 \times 10^6$  rotating hub at  $\mu = 0.152$ . The wake locations (1-4) correspond to Fig. 44. (Note: Data are presented using the final adapted grid.)

## 6.4 Static and Dynamic Force Correlations

The first simulations undertaken were to evaluate the grid requirements and the ability of the computational simulations to predict the hub forces. With the requisite number of normal cell layers within the boundary layer, as discussed in Section 5.1.1 and Ref. 51, the static hub drag is predicted very accurately by the computational approach, as depicted in Fig. 27. The drag is linear with the squared free stream speed. The maximum error occurs near a speed of zero with an error of 5%. Most errors are within 1%-2% over the speed range.

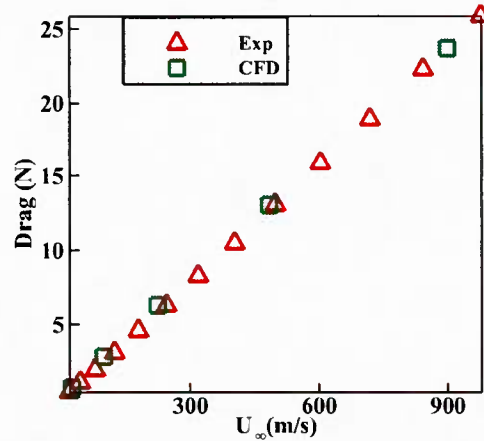


Figure 27: Correlation between experimental load cell and CFD data for the  $0^\circ$  static hub model

Comparison of the drag coefficient for the  $0^\circ$  and  $45^\circ$  static cases and the rotating case at 240 rpm results in drag coefficient values that are similar. The maximum drag occurs at  $0^\circ$  static orientation, while the minimum occurs at the  $45^\circ$  static orientation. The drag changes are directly related to the minimization of the frontal flat plate area as the orientation changes. This change results in fewer high pressure (near stagnation) areas, that are instead now suction areas, as illustrated in Fig. 28. Not unexpectedly, the rotational hub drag and pressure coefficient behavior falls between these two static results. Observing the pressures at the  $0^\circ$  azimuth (Figs. 28 a and c), overall the component pressure distributions appear to be similar, with the exception that the areas where lower pressure occurs have higher magnitudes when the model is rotating. This is particularly true for the forward and aft (with respect to the incoming flow from the left) root struts and blocks. The additional local velocity due to the rotation ( $V = \Omega R$ ) is particularly pronounced as the distance from the center of rotation,  $R$ , is increased, as expected.

Table 7: Comparison of global (total) drag coefficient.

	Model Scale
Static hub at $0^\circ$ orientation	1.26
Static hub at $45^\circ$ orientation	1.19
Rotating hub at 240 rpm	1.23

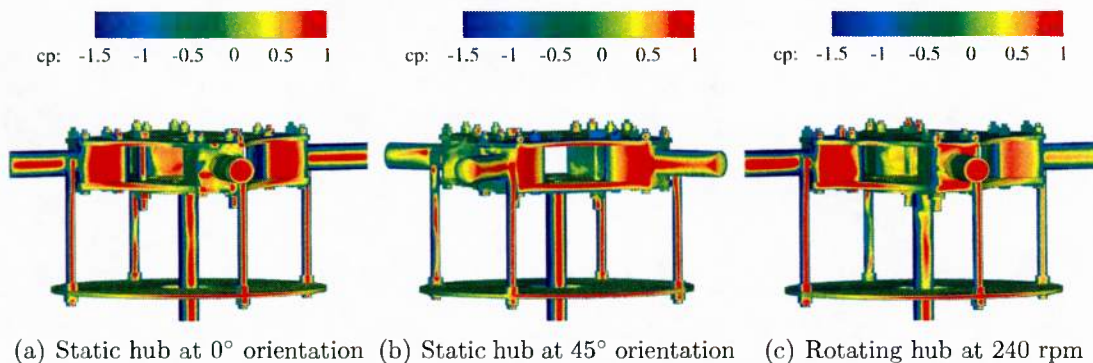


Figure 28: Surface pressure coefficient distribution on the static and rotating rotor hub. Free stream flow enters normal to the figure.

## 6.5 Drag Deconstruction

Analysis of the change in the individual component contributions to drag provides some insight into the cause of the differences in the total drag, and are directly related to the surface pressure changes in Fig. 28. The drag from each of the components for both the static cases (Table 8) and the rotating cases (Table 9) are presented. Using Fig. 21 to aid in the analysis, the differences in the physics is apparent. The components on the windward (forward) side of the hub maintain the higher drag, while the leeward (aft) hub components have significant reductions. The strut for the 45° azimuth has a higher drag value, but this is offset by the significantly lower shank and pitchlink drag values.

The actual change in drag coefficient on each component (Figs. 29a and 30a) yields the overall drag change, but the importance of each change is more readily observed by the percentage drag change in Figs. 29f and 30b. Approximately half of the components contribute a small relatively constant percentage change in the drag (within 2% - 4%) no matter what the configuration, static or rotating. For the components that are flat plates of various shapes, the drag reduction can be attributed primarily to the viscous (skin friction) drag as Reynolds number increases.<sup>94</sup>

Four components in particular, the blocks, driveshaft, shanks, and pitchlinks, do not conform to the relatively constant trend. These components are notably comprised of primarily bluff bodies, three of which are circular cylinders. Further analysis of the cylindrical components is compared with experimental results from Hoerner.<sup>95</sup> Due to the installation, most of these cylindrical components have “wall-like” ends and are of sufficient aspect ratio that they can be considered as essentially two-dimensional bodies, as per Hoerner’s experimental assessment. The critical Reynolds number ( $Re_c$ ) for cylinders in a cross-flow is approximately 300,000-400,000. The driveshaft is below  $Re_c$  and correlates with experimental drag predictions of 1.18 very well. Pitchlink 4 most accurately replicates the cylinder drag prediction, which is attributed to its orientation where it encounters minimal interference effects and nearly unperturbed free stream flow. Shank interference causes a reduction in drag obtained for pitchlinks 1 and 2; pitchlink 1 is affected by the presence of its shank and the assembly

Table 8: Drag tabulation for cylindrical components static azimuth orientations.

Component	$Re_d$	0°	45°
		$C_D$	$C_D$
Driveshaft	15,200	1.2305	1.612
Pitchlink 1	7,600	0.9353	0.9840
Pitchlink 2	7,600	1.0338	0.5697
Pitchlink 3	7,600	0.5377	1.1620
Pitchlink 4	7,600	1.1988	0.9614
Shank 1	21,000	0.2566	0.8151
Shank 2	21,000	0.7091	0.0469
Shank 3	21,000	0.0421	0.6929
Shank 4	21,000	0.6127	0.2639

Table 9: Average drag tabulation for rotating cylindrical components.

Component	Driveshaft	Pitchlinks	Shanks
Rotating at 240 rpm	1.2172	1.0371	0.6243

of pitchlink 2 is on the leeward side of its shank. Pitchlink 3 shows interference effects due to its location farthest downstream with respect to other components. Overall, the influence of scaling of the pitchlinks is negated due to the compensating interference effects, and this was observed at all static locations. Shanks 2 and 4, which should nominally compare with Hoerner at drag values of 1.18, encounter interference and/or finite aspect ratio effects that result in reduced drag from theory. For the rotating cases, the drag increases as the rotation speed increases, indicating the possible presence of the “Magnus” effect,<sup>95</sup> as well as changes in the friction drag and interference drag.

The above computations include the interference effects on the components. When each component is removed and the simulation recomputed, Fig. 31 indicates that the pitch links and blocks have significant decrease due to shank removal. Removal of the hub assembly results in a drag increase on the pitch links and a similar decrease on the driveshaft. Notably, the pitch link removal results in small change to surrounding components.

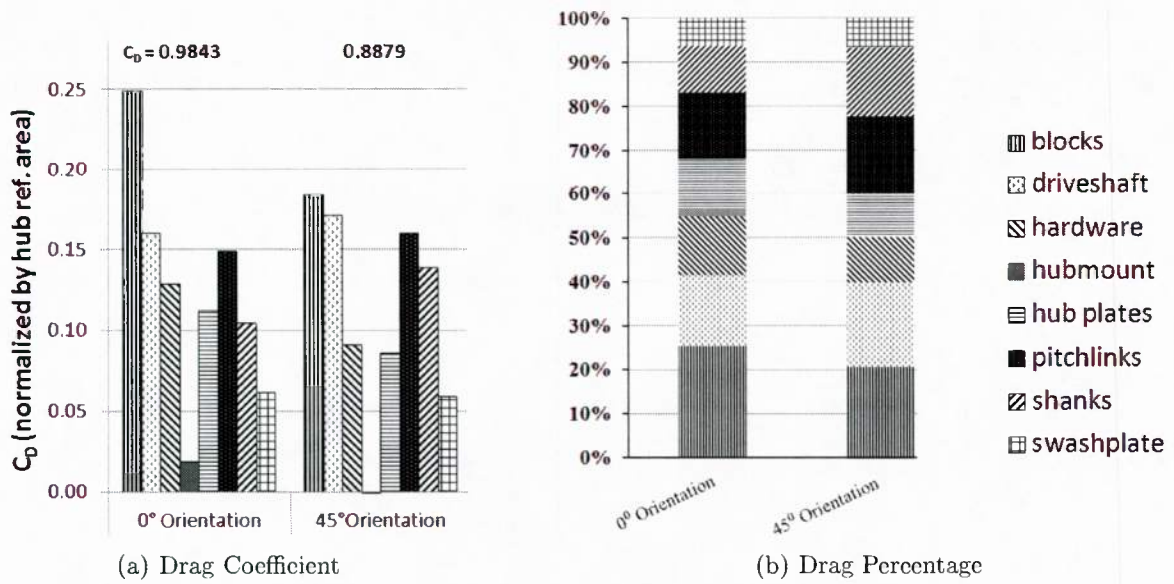


Figure 29: Component drag contributions to global hub drag for static simulations. (Note: Reynolds numbers are abbreviated such that 'M' implies millions.)

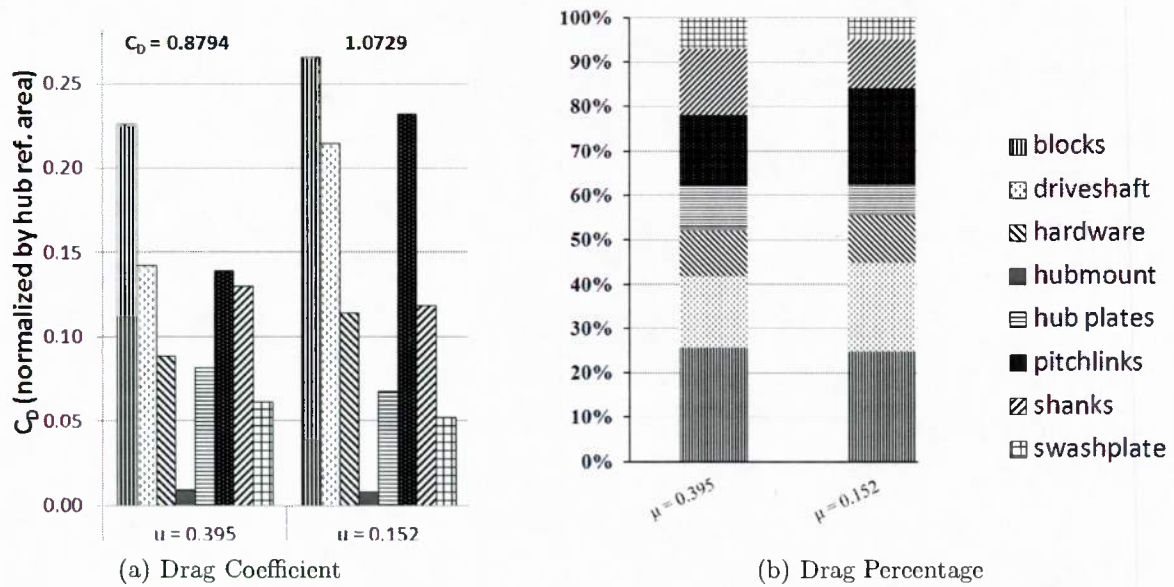
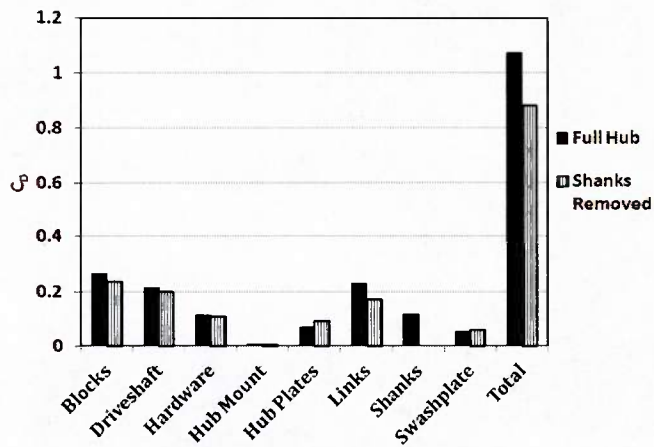
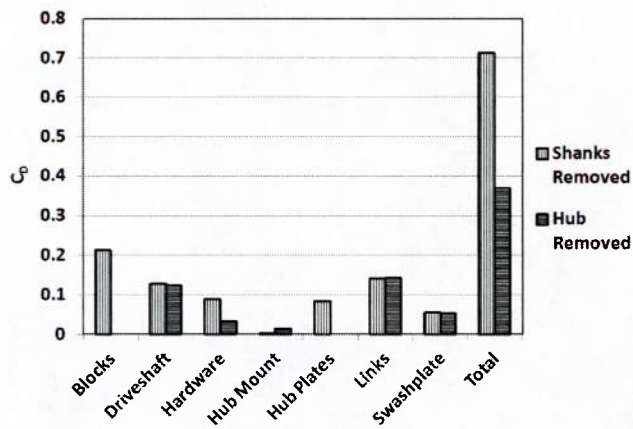


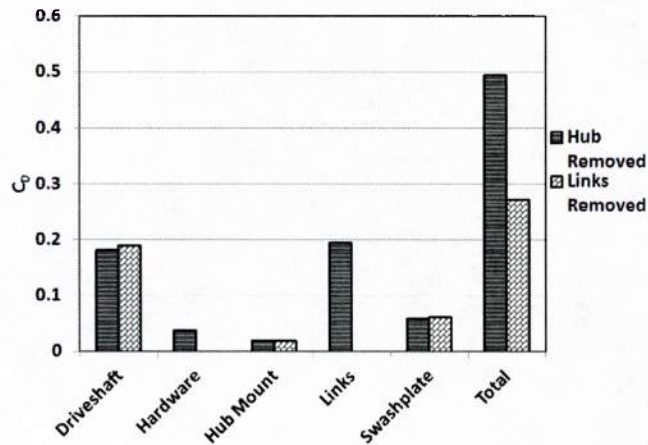
Figure 30: Component drag contributions to global hub drag for rotating simulations. (Note: Reynolds numbers are abbreviated such that 'M' implies millions.)



(a) Shank Removal



(b) Hub Removal



(c) Link Removal

Figure 31: Model scale ( $Re = 0.29 M$  at  $\mu = 0.152$ ) drag build-up due to sequential deconstruction.

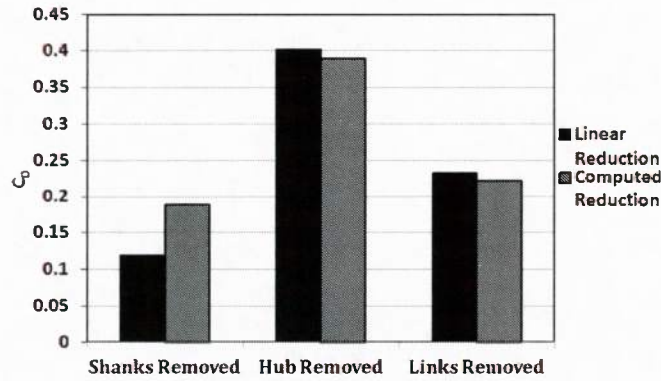


Figure 32: Comparison of linear and CFD computed drag reduction due to hub components at  $Re = 0.29 M$  and  $\mu = 0.152$ .

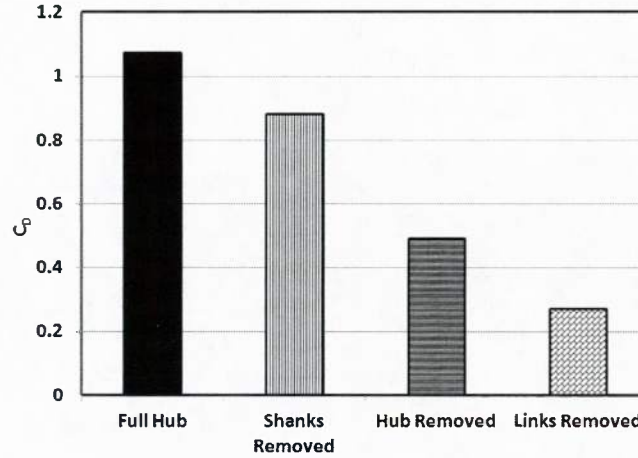


Figure 33: Total drag comparison at  $Re = 0.29 M$  and  $\mu = 0.152$ .

Analysis of surface pressure contours on the hub may provide further insight in to the trends in interference effects (Fig. 32) and the total drag comparison (Fig. 33). Out of the three deconstruction steps, the shank removal shows the biggest departures for linear drag reduction. For the  $Re = 0.29 M$  condition (Fig. 34 (a) v. (b)), the major areas of drag reduction are observed on the blocks (retreating side), and the pitch links, mainly due to shank interference.

Small differences are visually noted due to hub removal (see Fig. 34 (b) v. (c)). These are on the upper drive shaft, the hub mount, and the upper portion of the pitch links. Link removal creates the largest change on the surface pressures resulting on the drive shaft. Minimal difference is noted for the pressures for the  $\mu = 0.152$  condition at  $Re = 0.29 M$  (Fig. 34 (c) v. (d)).

Pressure coefficient distributions at various cross sections of the driveshaft (see Fig. 35) are compared to note the influence of interference effects in Fig. 37. The pressure coefficient is plotted as a function of the central angle  $\theta$  as defined in Fig. 36. Asymmetry in the distribution is expected with separated flow dominating the pressure side ( $\theta > 0$ ). The overall trend for all conditions with component removal causes the asymmetry to decrease at the model scale. At the  $Re = 0.29$  M condition (Figs. 37 and Figs. 38), the links removed condition recovers nearly all the symmetry except for the small rotation effects that alter the flow in a more localized fashion and are not affected by pitch links, the hub plates, or the shanks. The nearly symmetric pressure coefficient curves on the model scale driveshaft are not reproduced at the full scale simulations.<sup>96</sup>

The separation point on the suction side moves more upstream at the extreme cross-sections (slices one and eight) for the full hub (Fig. 37 and Fig. 38). For all three subsequent deconstruction configurations, the separation point at slice one is slightly upstream in comparison to the other cross-sections. This pattern is not observed for slice eight, on the other hand, as the flow remains more attached than at other cross sections. This may be because slice eight is affected by interference from a static object (the fuselage), as opposed to slice one being affected primarily by the rotating hub plates and mount.

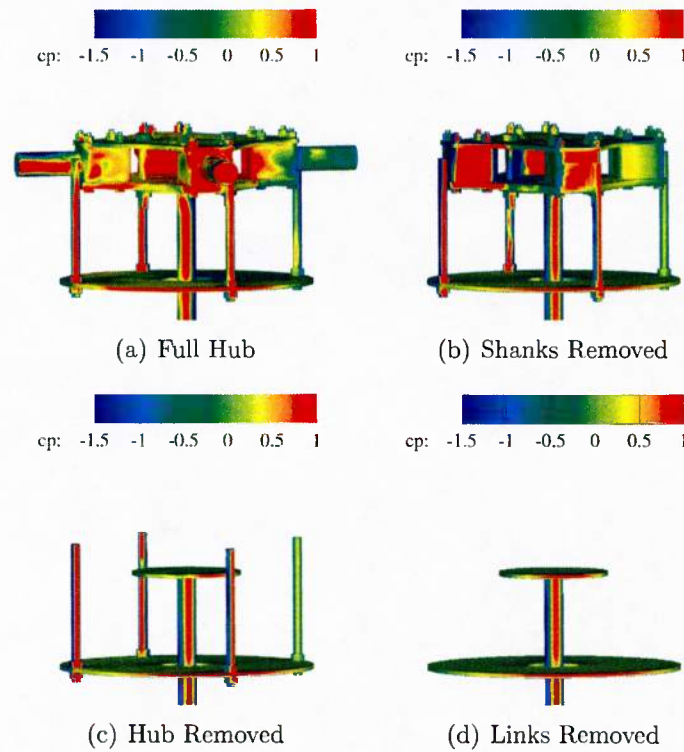


Figure 34: Surface pressure contours at  $Re = 0.29$  M and  $\mu = 0.152$ .

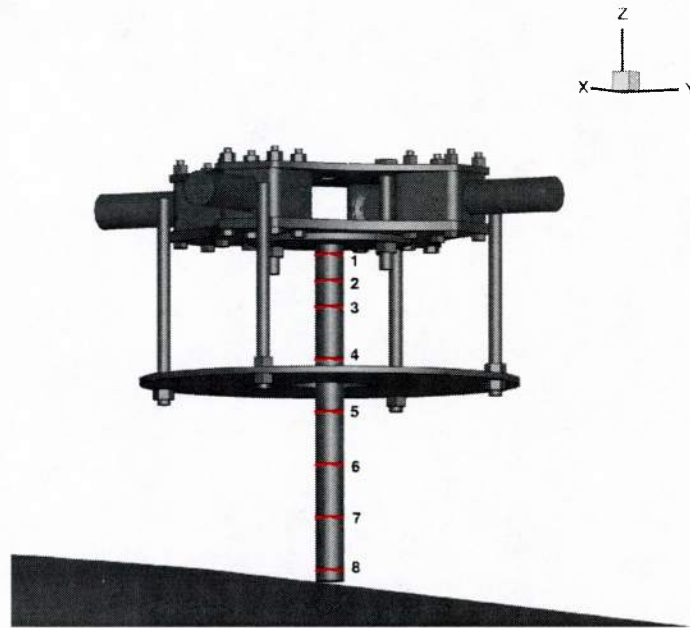


Figure 35: Driveshaft slice locations at which pressure coefficient plots are investigated.

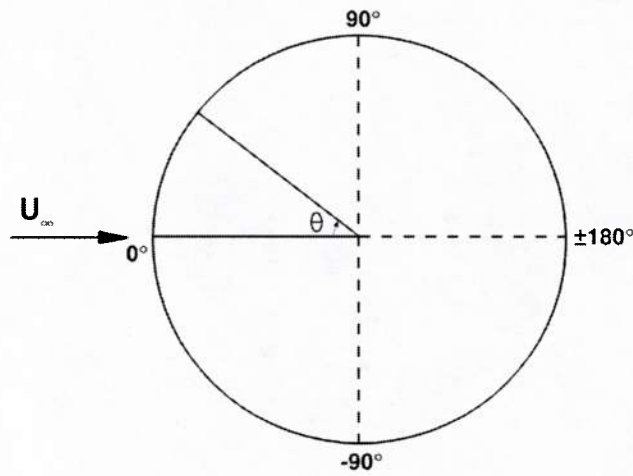
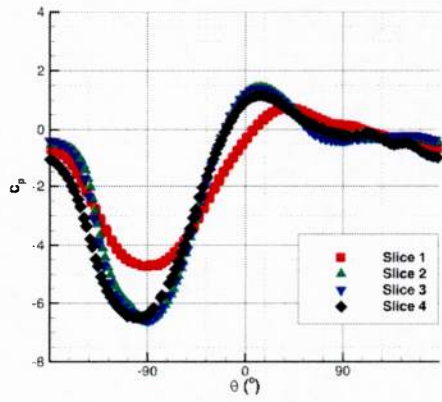
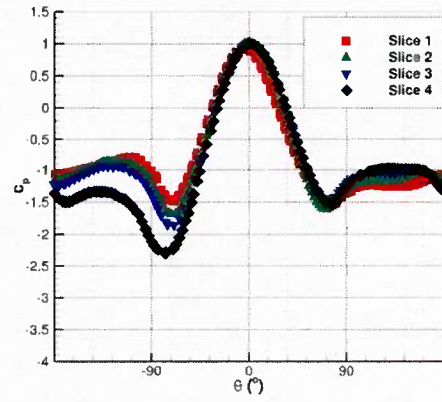


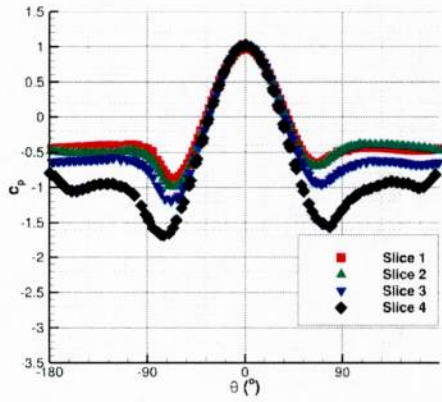
Figure 36: Definition of the driveshaft central angle  $\theta$  with respect to circular components in the flow field.



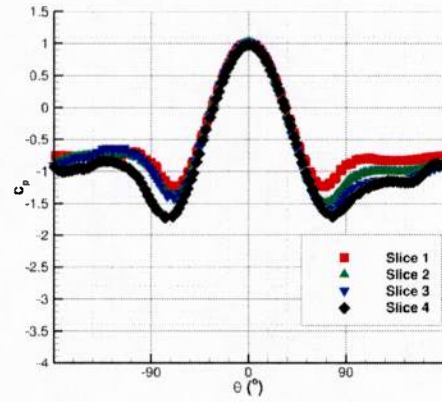
(a) Full Hub



(b) Shanks Removed

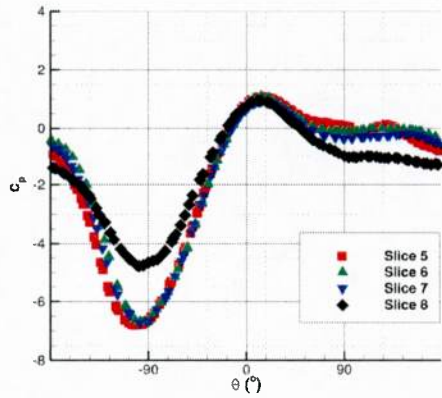


(c) Hub Removed

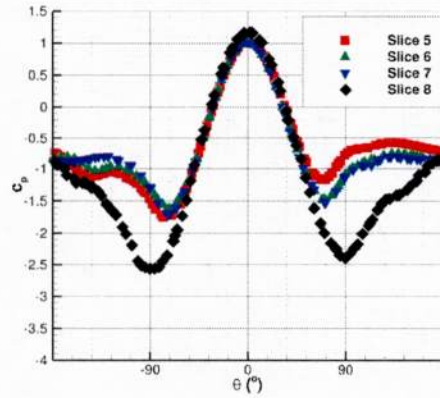


(d) Links Removed

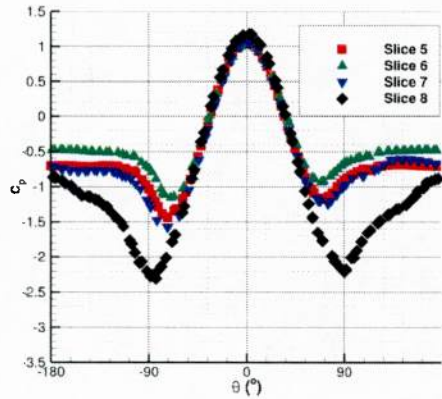
Figure 37: Pressure distribution (top four slices) at  $Re = 0.29 M$  and  $\mu = 0.152$ .



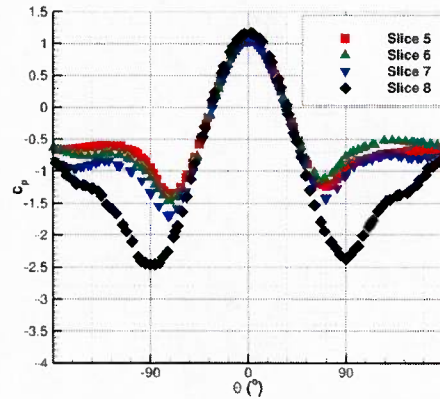
(a) Full Hub



(b) Shanks Removed



(c) Hub Removed

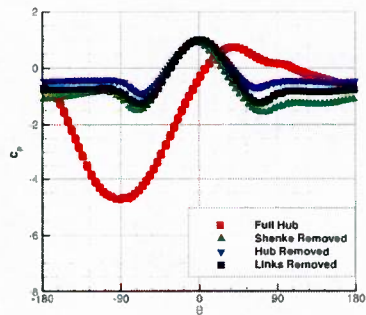


(d) Links Removed

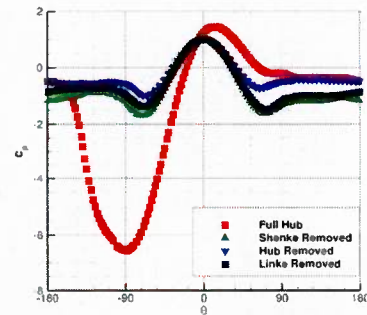
Figure 38: Pressure distribution (bottom four slices) at  $Re = 0.29$  M and  $\mu = 0.152$ .

The interference effects between the components is further elucidated by plotting the pressure coefficients along each slice for the deconstruction, as provided in Fig. 39. At the model scale Reynolds number (Fig. 39), the removal of the shanks has a dramatic effect on the pressure coefficient at all slice locations. In particular, the primary cause of asymmetry in the pressure distributions is clearly caused by the the rotating shanks. Further deconstruction results in minor changes in the pressure distributions, which appear to be very similar to infinite cylinder pressure distributions.<sup>95,97</sup>

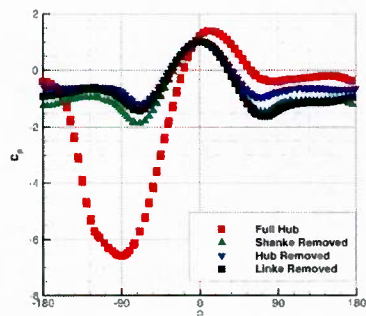
The specifics of the pressure distributions are quantified in Tables 10 to 13.



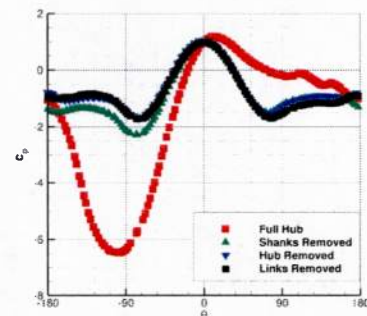
(a) Slice 1



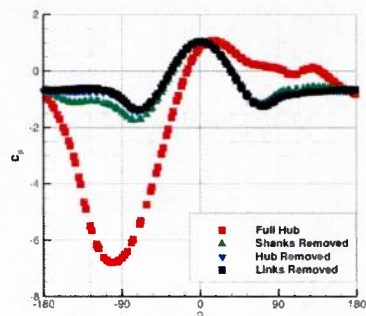
(b) Slice 2



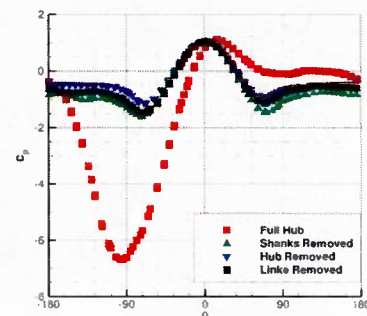
(c) Slice 3



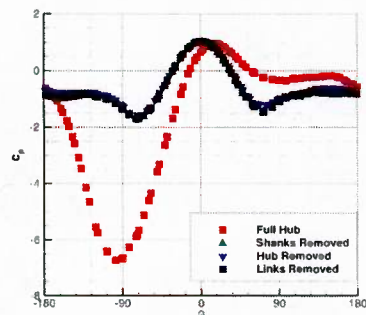
(d) Slice 4



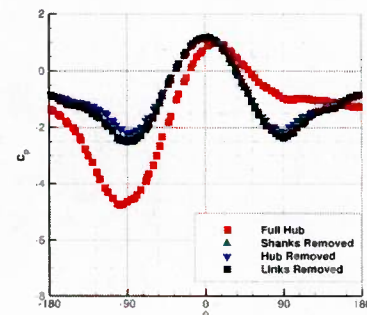
(e) Slice 5



(f) Slice 6



(g) Slice 7



(h) Slice 8

Figure 39: Pressure distributions along slice locations (Fig. 35) illustrating component interference at  $Re = 0.29 M$  and  $\mu = 0.152$ .

Table 10: Full Configuration ( $Re = 0.29$  M at  $\mu = 0.152$ )

Slice	$\theta_{c_{pmax}}$	$c_{pmax}$	$c_{pmin_l}$	$c_{pmin_r}$	$\theta_{c_{pmin_l}}$	$\theta_{c_{pmin_r}}$	$\theta_{sepl}$	$\theta_{sepr}$
1	39.027	0.731	-4.663	-0.709	-80.216	178.205	-113.134	66.863
2	15.539	1.437	-6.571	-0.225	-87.687	81.712	-121.576	41.689
3	14.086	1.390	-6.610	-0.405	-90.000	79.696	-120.818	122.041
4	13.491	1.168	-6.495	-0.235	-95.498	95.556	-126.927	39.113
5	16.403	1.059	-6.795	-0.124	-101.725	102.475	-177.230	60.462
6	14.191	1.092	-6.704	-0.115	-96.095	83.904	-165.807	132.760
7	15.042	0.938	-6.737	-0.373	-97.888	97.687	-171.467	122.847
8	13.036	0.948	-4.774	-1.048	-98.543	94.378	-177.603	53.284

Table 11: Shanks Removed ( $Re = 0.29$  M at  $\mu = 0.152$ )

Slice	$\theta_{c_{pmax}}$	$c_{pmax}$	$c_{pmin_l}$	$c_{pmin_r}$	$\theta_{c_{pmin_l}}$	$\theta_{c_{pmin_r}}$	$\theta_{sepl}$	$\theta_{sepr}$
1	-2.783	0.923	-1.486	-1.550	-69.169	75.598	-118.481	89.999
2	1.207	1.018	-1.687	-1.610	-71.185	71.866	-131.220	85.897
3	0.583	0.999	-1.861	-1.464	-68.873	74.259	-134.957	144.949
4	0.448	0.996	-2.297	-1.510	-77.113	76.768	-179.551	89.999
5	2.768	1.022	-1.751	-1.165	-77.524	68.720	-133.410	84.313
6	0.575	1.021	-1.629	-1.486	-74.076	69.579	-133.820	83.904
7	-0.338	1.010	-1.714	-1.522	-73.108	71.858	-144.815	89.999
8	2.395	1.165	-2.562	-2.396	-90.000	89.999	-112.271	111.505

Table 12: Hub Removed ( $Re = 0.29$  M at  $\mu = 0.152$ )

Slice	$\theta_{c_{pmax}}$	$c_{pmax}$	$c_{pmin_l}$	$c_{pmin_r}$	$\theta_{c_{pmin_l}}$	$\theta_{c_{pmin_r}}$	$\theta_{sepl}$	$\theta_{sepr}$
1	-0.359	0.979	-0.899	-0.679	-65.601	64.521	-140.362	75.827
2	1.361	1.002	-0.992	-0.705	-65.160	65.752	-115.475	77.801
3	2.284	1.013	-1.188	-0.951	-68.450	69.556	-161.033	79.792
3	0.179	1.026	-1.685	-1.561	-75.131	78.309	-179.819	89.999
5	0.013	1.039	-1.442	-1.180	-72.682	69.068	-141.958	83.802
6	0.890	1.035	-1.158	-0.934	-69.891	69.273	-134.683	77.110
7	1.428	1.045	-1.576	-1.250	-72.693	75.076	-148.401	82.859
8	2.291	1.176	-2.305	-2.209	-83.349	89.999	-177.711	111.591

Table 13: Links Removed ( $Re = 0.29 M$  at  $\mu = 0.152$ )

Slice	$\theta_{c_{pmax}}$	$c_{pmax}$	$c_{pmin_l}$	$c_{pmin_r}$	$\theta_{c_{pmin_l}}$	$\theta_{c_{pmin_r}}$	$\theta_{sep_l}$	$\theta_{sep_r}$
1	1.572	1.001	-1.269	-1.243	-68.137	70.137	-117.443	80.659
2	-0.860	1.009	-1.384	-1.502	-68.164	71.865	-121.576	85.897
3	0.583	1.011	-1.416	-1.622	-68.874	74.259	-96.936	89.999
4	0.448	0.976	-1.712	-1.699	-77.113	78.185	-179.551	89.999
5	2.768	1.045	-1.368	-1.249	-69.539	72.440	-155.186	84.313
6	0.575	1.040	-1.474	-1.139	-71.939	69.579	-179.424	83.904
7	1.985	1.030	-1.715	-1.435	-73.108	71.858	-178.014	89.999
8	2.392	1.165	-2.456	-2.371	-90.000	89.999	-112.215	111.505

## 6.6 Interference Drag

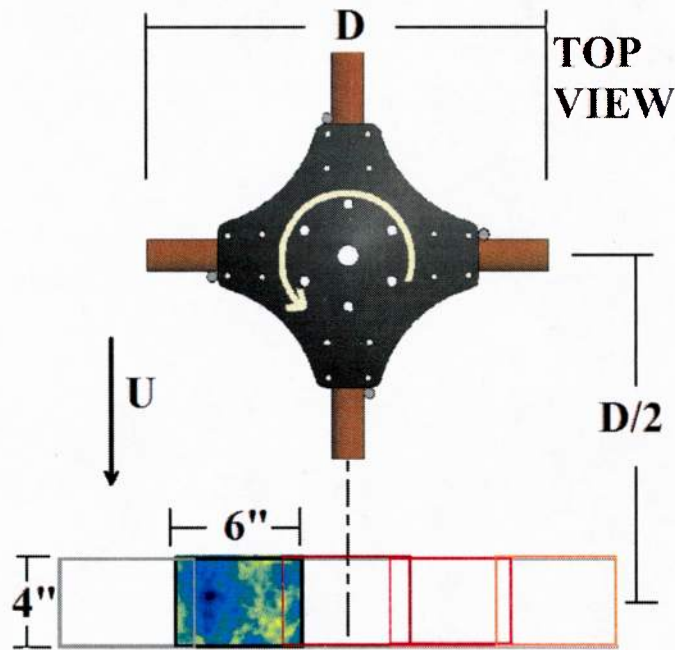
Component drag deficits for the static models lie between 4% and 54%. The individual component analysis does not account for these large deficits, thus interference drag is clearly present. The presence, or lack thereof, of interference drag can be readily observed using surface pressure coefficients. Figure 28 compares the surface pressures for the  $0^\circ$  static,  $45^\circ$  static, and rotating configurations, respectively. Pressure contours that remain consistent along a component indicate minimal interference effects are present. This permits the application of component drag characteristics, such as those found in Hoerner<sup>95</sup> during design.

The nonlinearity associated with interference drag for the rotating hubs is clearly illustrated in Fig. 43. Here, the rotating cases are examined in planform images for the mid-plane of the hub using identical contour levels. Overall, greater mixing is observed in the full scale flow fields (hence vorticity levels are lower) due to increase in the Reynolds number creating a more turbulent wake. The change in pressure coefficient and shed wake are clearly related when comparing Figs. 43 and 28. Interference effects can be observed on the left blade shank connector (just below the bolts), in Fig. 28 where the trailing edge pressure suction shifts to a more forward location from the bottom to top of the connector.

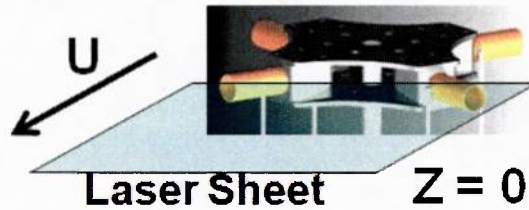
The removal of the blade shanks to examine the deconstructed model indicates that the blade shank contribution to the total drag is minimal. Upon removal of the blade shanks and the hub plates, the drag decreases by approximately one-third. Two thirds of the hub drag are due to the contributions of the drive shaft, swashplate and pitch link drag increments. Rotating each of these deconstructed models confirms that there is little variation in drag from the static configuration. The pitch link drag contribution may be computed from the shift in measurements from the prior deconstructed model.

## 6.7 Wake Characterization

The unsteady wake of the hub was experimentally evaluated through the use of particle image velocimetry (PIV), and was simultaneously or *a priori* analyzed with computational simulations. Experimental velocity deficits in the wake were obtained at a distance one hub diameter, as measured from the hub centerpoint (Fig. 40).



(a) Top view

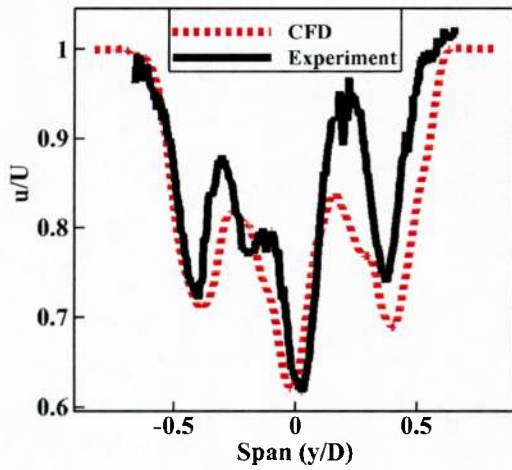


(b) Isometric View

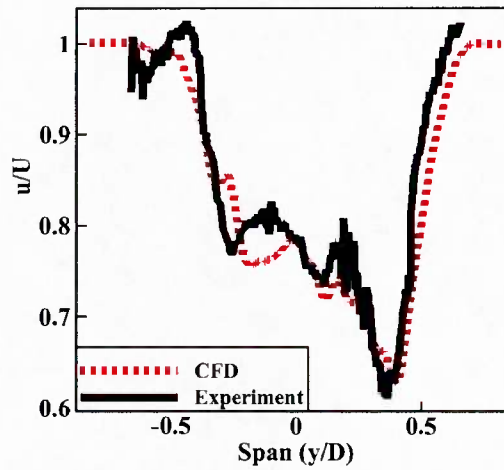
Figure 40: Map of PIV data collection plane comprised of overlapping stitches. From Ref. 91.

Computational results were correlated with experimental data to ascertain the ability of the computational adapted mesh - obtained *a priori* to observing the experimental results to capture the details of the wake. Both experimental and computational methods show a contraction of the momentum deficit in the hub wake when the model is oriented at  $45^\circ$  azimuth, corresponding to a reduction of hub drag based on frontal area. The experimental and computational wake velocity deficits correlated very well, as illustrated by Fig. 41. The causal wake behavior that drive the momentum deficits observed in Fig. 41 is clearly illustrated by the computational velocity contours downstream of the hub (Fig. 42). The largest deficit at the static hub centerline is clearly defined by the strong velocity deficit just behind the hub main shaft. The two secondary wake deficits appear behind the pitch links to the left and right of the hub shaft. When the hub rotates in a counter clockwise direction,

the primary velocity deficit is translated upward and to the right, appearing behind the right (aft looking forward) blade shank. The velocity deficit due to the main drive shaft appears to have coalesced with that of the right pitch link, leveling only a secondary velocity deficit from the left pitch link, which has also translated in the positive y-direction (to the right) of the flow induced by the counter clockwise rotation.



(a) Static hub at  $0^\circ$  orientation



(b) Counter clockwise rotating hub at 240 rpm

Figure 41: Comparison of experimental (PIV) and *a priori* computational data for the tunnel axis wake velocity deficit for  $U_\infty = 8.941$  m/s.

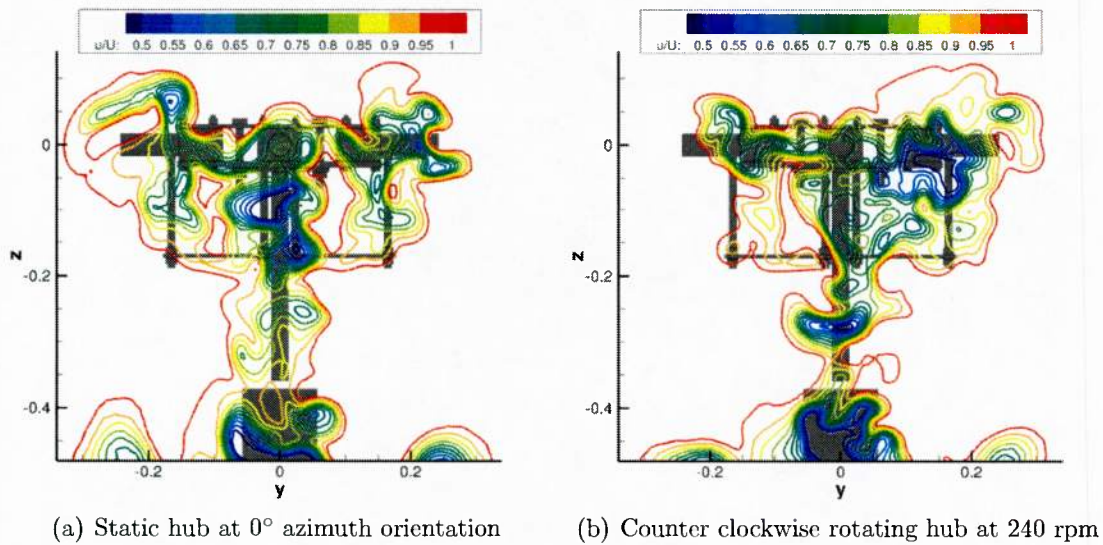


Figure 42: Velocity contours one hub diameter downstream of the hub center for  $U_\infty = 8.941$  m/s.

Further insights into the character of the flow on and behind the hub can be obtained from the computational simulations. Consider for example, the velocity contours presented in planform view (looking down on the rotor hub) in Fig. 43 for the static  $45^\circ$  azimuth, rotating, and static  $0^\circ$  azimuth cases. (The solid black line on the right of each figure indicates the downstream location of the velocity contours presented in Fig. 42.) The effects of rotation yield a contracted wake span similar to the  $45^\circ$  static case. As noted previously in the discussion of the force measurements, the drag for the rotating hub is similar to the drag of the static  $45^\circ$  azimuth orientation. The near-body wake behavior of these two cases are clearly similar, in contrast to the near-body shed wake of the static  $0^\circ$  azimuth case. The rotation causes significant vortex shedding from the blade shanks, similar to the bluff-body shed wake of the shanks when they are obliquely aligned with the free stream.

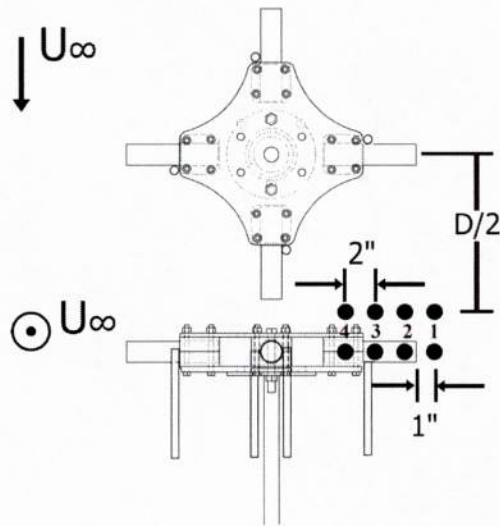


Figure 44: Wake hot-wire sampling locations. From Ref. 91.

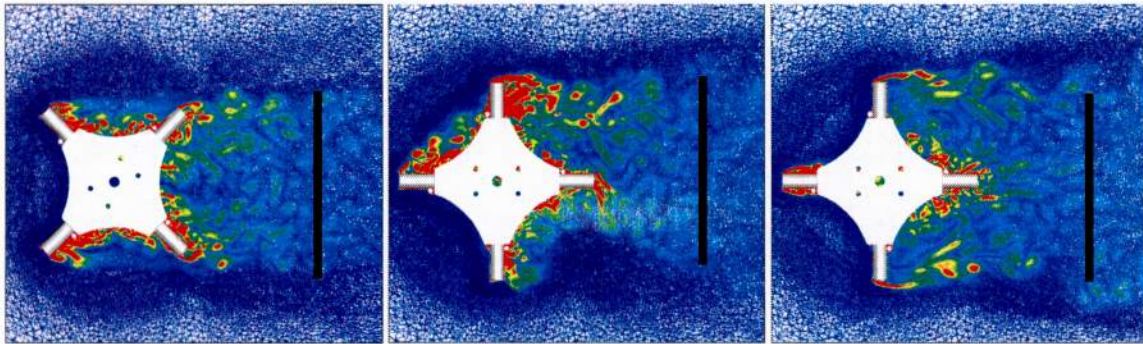


Figure 43: Illustration of the wake extent (via vorticity contours) for the static at  $45^\circ$  orientation (left), rotating (center) and  $0^\circ$  static orientation (right) ( $U_\infty = 8.941$  m/s).

## 6.8 Velocity Frequency Spectra

Experiments were conducted wherein a single axis hot-film anemometer measured velocity fluctuations at a few selected locations (Fig. 44) in the hub wake. Experiment and computational power density spectra plots for the static and rotating tests are illustrated in Figs. 45 and 46, which correspond to locations moving inboard of the hub wake. The initial computational simulations were computed before the experimental data were collected. Because the hot-wire anemometry locations were not known until after the experiment, these runs were continued, without user intervention, until enough data at these locations were obtained to perform the Fast Fourier Transforms (FFT) analyses at the selected locations. During these additional rotor revolutions, no significant changes in the other parameters analyzed were

observed.

The power spectra data are compared with the classic 5/3 law, which characterizes homogeneity of turbulence. A study in the shedding frequencies of bluff bodies by Sakamoto and Arie<sup>98</sup> provides Strouhal numbers of circular cylinders of varying aspect ratios. Their investigation yields predicted shedding frequencies in agreement with the blade shank frequency of approximately 50 Hz as seen from sample location two, just behind the shank. There is a noticeable amplitude spike for all sampling locations of the rotating test case corresponding to the predicted four-per-revolution signal of the four-bladed hub model. Both the experimental and CFD efforts capture this corresponding frequency of 16 Hz as the hub rotates at 240 rpm (4 rev/sec). The next harmonic of this frequency (8 per rev.) is greatly amplified at the inboard sampling location, well within the wake region.

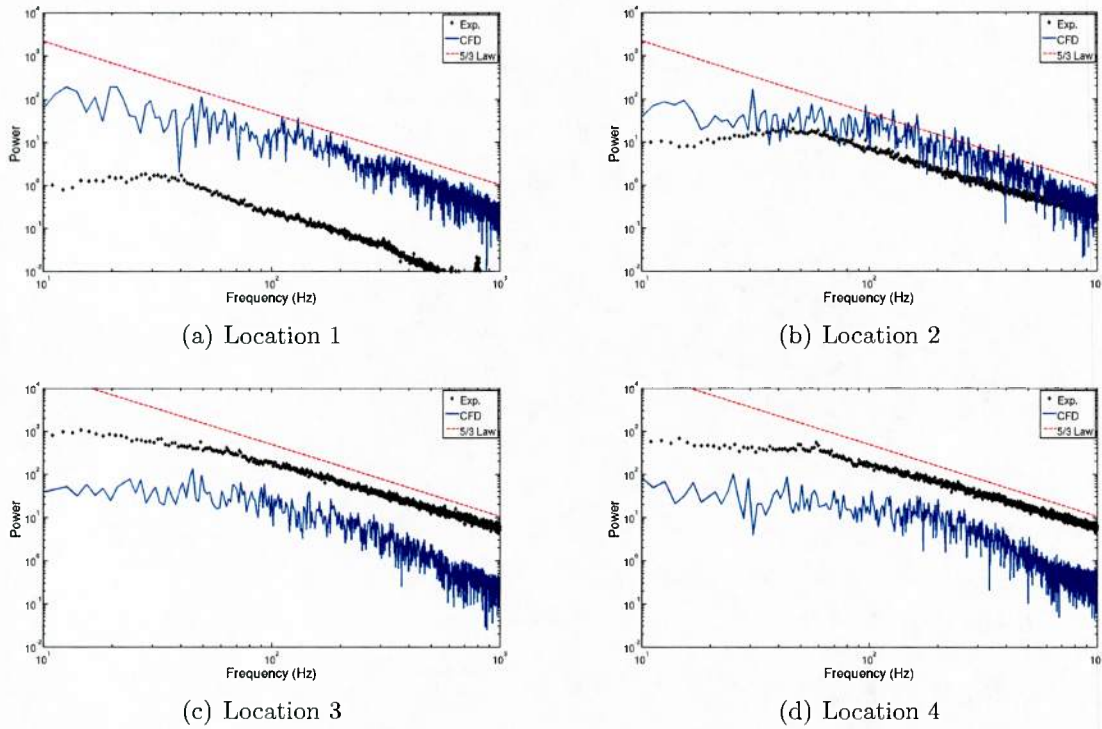


Figure 45: Power density spectrum of velocity fluctuations in the hub wake for the static hub at  $0^\circ$  orientation at  $U_\infty = 13.41$  m/s.

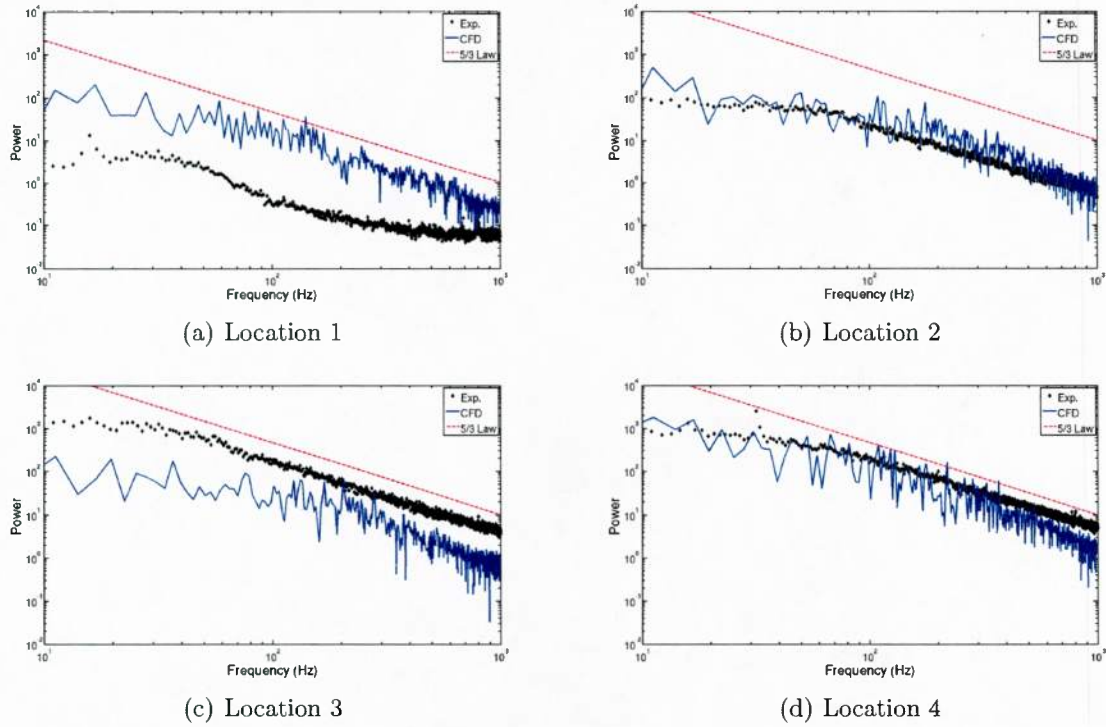


Figure 46: Power density spectrum of velocity fluctuations in the hub wake for the rotating hub at 240 rpm  $U_\infty = 8.941$  m/s.

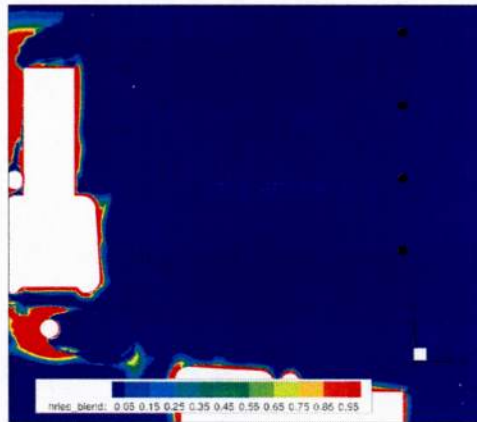


Figure 47: Top view of HRLES blending function contours.

Better agreement with 5/3 law slope is noticed for both the experimental and computational results at inboard locations. The turbulence displays an expected broad range of scales in the bluff body wake region. Contours of the HRLES turbulence model's blending

function are given in Fig. 47. Values near one indicate that the RANS formulation is in effect and values near zero indicate regions dominated by LES. The four locations show that the methodology is capturing of the broad range of turbulent scales with LES.

The power spectral plots (Figs. 45, 46, and 48) show some disagreement in the magnitude of power obtained between experiment and computations. The general observation is an over-prediction in power obtained by CFD at location one, attributed to the computational shear layer prediction coinciding with location one. One explanation for the discrepancies are that the wake comparisons have not been made at the same location due to an experimental uncertainty (as noted by the rapid changes in the wake extent near the comparison location in Fig. 43). Another is that further additional adaptations or simulation length may be needed in the computations. Recent experiments with hot-wire anemometry were analyzed, raising additional questions, as referenced in Section 7.3.

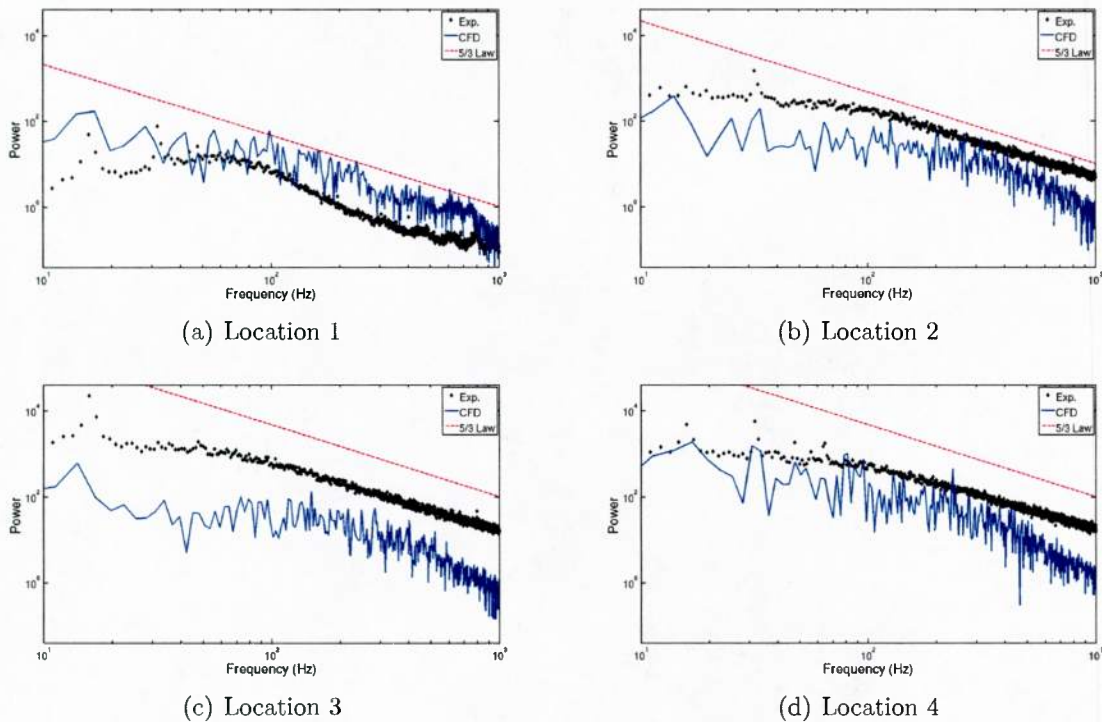


Figure 48: Power density spectrum of velocity fluctuations in the hub wake for the rotating hub at 240 rpm at  $U_\infty = 22.35$  m/s.

## 6.9 Reynolds-averaged Scaling Analysis

Under the final funding profile, the computational scaling analysis from wind tunnel model to full helicopter was not possible. However, additional funding was obtained from the Vertical Lift Consortium (VLC) to perform this study. This analysis is documented in

Refs. 93 and 96, and are not presented in this report. The analysis used the original computations described in the prior sections for correlation. The full-scale configuration was examined at flight conditions based on the UH-60A C8534 counter<sup>99</sup> to provide an order of magnitude increase in the global Reynolds number compared to the model scale experiment. To illustrate the Reynolds number effects, two full-scale rotating conditions to provide a variation based on rotating speed and advance ratio were also analyzed along with the static hub orientations are discussed. Finally, the inflow effects due to the presence of a fuselage were modeled using the Robin fuselage.

From Shenoy et al.,<sup>93</sup> the main conclusions from this study are

1. The boundary layer and near body grid should be designed for the viscous characteristics of the highest Reynolds number calculation. Computations indicate that the error can increase linearly with the increase in Reynolds number.
2. The application of a mesh adaptation technique that encompasses overset grids without regard to mesh boundaries improves the near wake and integrated load predictions, and permits an initial grid to be applied to a number of configurations without the need to develop new grids.
3. Components that are bluff bodies lead to nonlinear scaling of the drag through a combination of Reynolds number scaling effects and changes in the interference drag. For components that remain clear of the shed wakes, theoretical and experimental estimates of drag for each individual component correlate well with the computational results.
4. The determination of the interference drag for rotating bodies must include an estimation of the translational shift or bias in the shed wake due to the generation of side forces (Magnus effect). The shed wake translates as a function of the local velocity on the component surface with the free stream velocity and is clearly observed in the computational evaluations.
5. When scaling the drag during rotation, velocity scaling based on the advance ratio rather than the angular velocity of the rotor appears to a more appropriate physical scaling.

## 7 Scissors Configuration Analysis

The hub analysis presented thus far has been based on computations and experiments performed prior to late 2011, when wind tunnel renovations were undertaken. A final set of analyses with the addition of a scissors component (Fig. 49) was undertaken. There was no PIV data obtained in the last experiment, instead hot-wire anemometry was used to obtain wake velocities to augment the load cell force data. All computational results were obtained *a priori* to correlation with the experimental results.

$U_\infty$	8.941 m/s	13.41 m/s	22.35 m/s
120 rpm	Forces		
240 rpm	Forces, Velocities	Forces, Velocities	Forces

Table 14: Matrix of flow conditions and analysis methods.

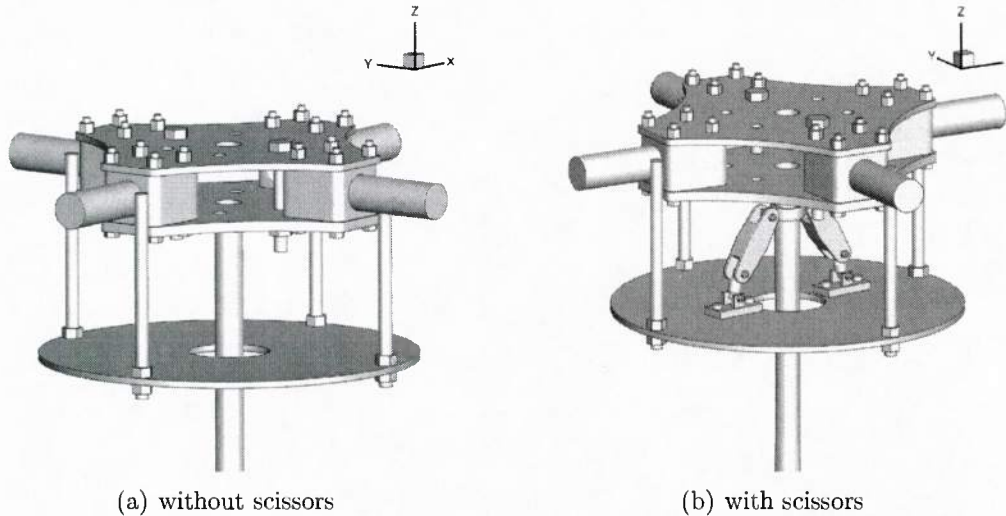


Figure 49: Hub configuration with and without scissors.

The hot-wire anemometry data were provided in the form of velocities of the form  $V_h$  as well as perturbations of this velocity.<sup>2</sup> The quantity  $V_h$  is the effective hot-wire measured velocity given by

$$V_h = \sqrt{u^2 + k_v v^2 + w^2}, \quad (25)$$

where  $k_v = 0.2$  as reported by experimental calibration. The presentation of the experimental data in this manner permitted a number of new statistical analyses.

Table 14 describes the different flow conditions analyzed and the analyses methods performed in this work. Forces are computed for each simulation performed, while velocity fields (mean and turbulent) were computed and correlated (wherever applicable) for  $U_\infty = 8.941$  m/s and  $U_\infty = 13.41$  m/s at 240 rpm.

## 7.1 Hub Drag Loads Analysis

The effect of the loads due to addition of the scissors is described in Table 15. The additional 10% drag increase at 120 rpm predicted by CFD was also predicted by the experiment.<sup>52</sup> The net drag increase at 240 rpm varies with the free stream speed and does not correlate

<sup>2</sup>Retrieved from <http://www.adl.gatech.edu/expaero/hubdrag/> on July 2, 2013, and verified through September 29, 2013.

Flow Condition	Configuration	$C_D$	% increase
$U_\infty = 13.41$ m/s at 120 rpm	without scissors	1.265	10.6%
	with scissors	1.397	
$U_\infty = 8.941$ m/s at 240 rpm	without scissors	1.263	15.9%
	with scissors	1.463	
$U_\infty = 13.41$ m/s at 240 rpm	without scissors	1.291	11.3%
	with scissors	1.437	
$U_\infty = 22.35$ m/s at 240 rpm	without scissors	1.237	6.1%
	with scissors	1.312	

Table 15: Drag coefficient comparison showing the effect of scissors at 240 rpm.

with the drag increase at 120 rpm. Also, the drag increase due to the scissors appears to decrease with increasing advance ratio or free stream speed. It is not determinable whether the effect of the drag increase due to the scissors is a function of the free speed primarily since simulations were not performed at the lower rotor speed at different free stream speeds.

## 7.2 Vibratory Loads Analysis

The unsteady drag and side force coefficient harmonics for the scissors hub are plotted in Figs. 50 and 51, respectively. The effect of the scissors can be assessed via these plots on the contribution to these forces. It is clear that the scissors have a major contribution in the two-per-rev harmonic for both forces. For both forces, the four-per-rev and eight-per-rev harmonics are prevalent and the four-per-rev energy is generally greater than that of the eight-per-rev. The exceptions are the drag harmonics at  $U_\infty = 8.941$  m/s, where the eight-per-rev energy is stronger for both configurations. Frequencies greater than four-per-rev are caused by aerodynamic wake structures that impinge on the oncoming geometry; at  $U_\infty = 8.941$  m/s, the advance ratio is smallest ( $\mu = 1.463$ ) indicating that the wake influence and impingement on the oncoming blade on the advancing side is the greatest. This is illustrated by a qualitative comparison of the wakes of two simulations in Fig. 52. At the lower speed, there are significant wake shedding that impinges on the advancing strut (top) from the forward strut (left) compared to the wake shedding for the higher velocity. These structures have a greater contribution on the advancing blade higher harmonics, where a significant drag contribution is obtained. This explains the discrepancy observed in Fig. 50(a).

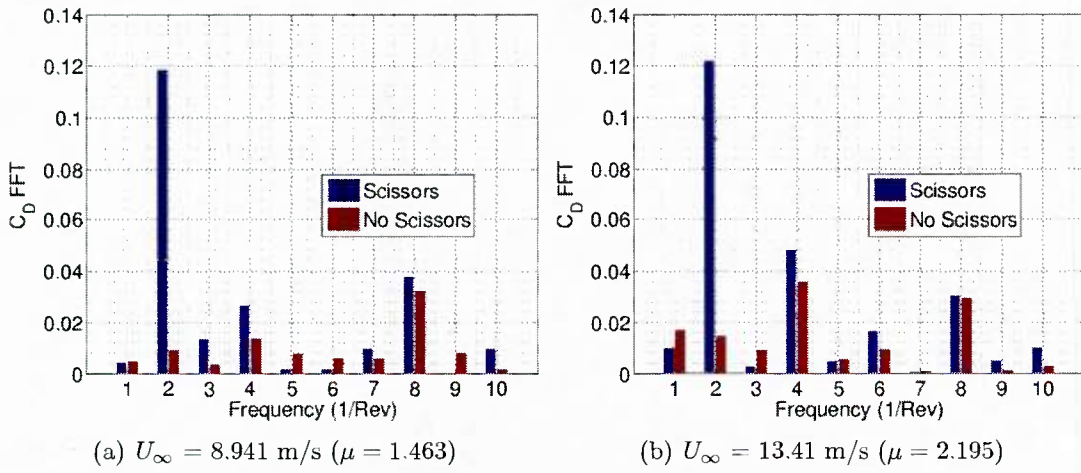


Figure 50: Comparison of unsteady drag coefficient ( $C_D$ ) harmonics for a rotating hub with scissors at 240 rpm.

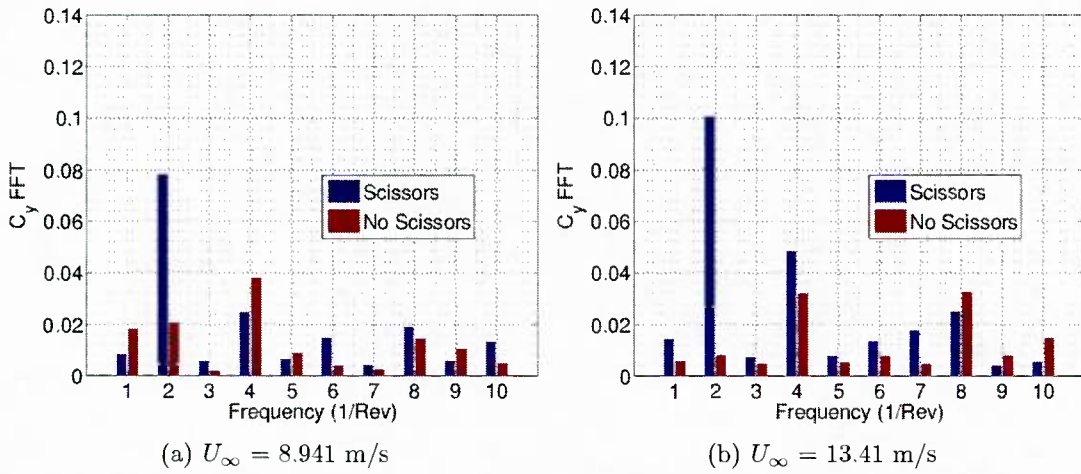


Figure 51: Comparison of unsteady side force coefficient ( $C_y$ ) harmonics for a rotating hub with scissors at 240 rpm.

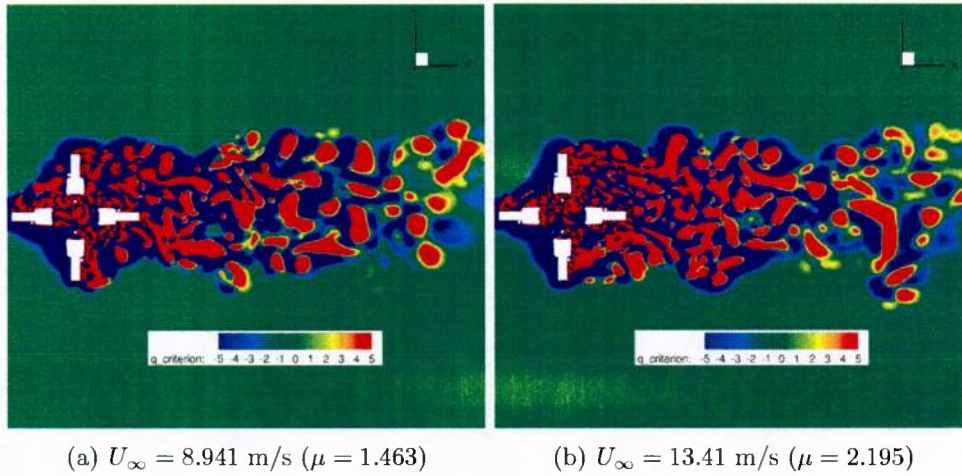


Figure 52: Q-criterion contours of the wake at  $Z = 0.0$  m at 240 rpm.

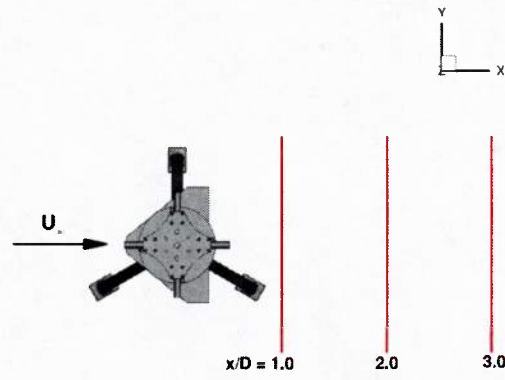
### 7.3 Wake Velocity Correlations

Wake velocities were obtained from the CFD simulations at  $X = 1D$ ,  $X = 2D$ , and  $X = 3D$  downstream of the hub for comparing trends and analyzing velocity spectra. The spatial locations of these probes are delineated in 53. In addition to the hub level at  $Z = 0.0$ , data are obtained at wake locations directly behind the seissors at  $Z = -0.204 D$  so that the effect of the seissors on the downstream wake may be determined.

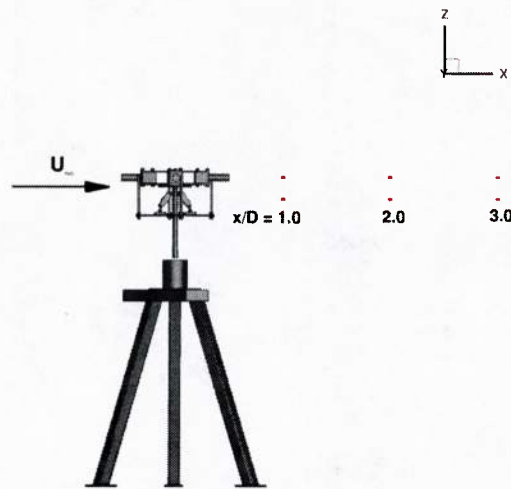
The *a priori* correlation between the computational and experimental wake data is not as accurate when hot-wire anemometry was utilized, when compared to the previous *a priori* computational correlation with the experimental PIV results obtained without the seissors (see Section 6.7). A typical example of the new experimental hot-wire and computational velocities are compared in Fig. 54. The computational approach for measuring the velocities is the identical to the approach applied with the PIV experimental correlations. Unfortunately, there was not PIV and hot-wire anemometry experimental data obtained with both hot-wire anemometry and PIV at the same locations for comparative analysis. Therefore, an alternate analysis to examine the discrepancies using the computational results comparing the data where both sets of experimental measurements were obtained.

Since the seissor components are located near the hub center (Fig. 49), the predicted wake extent from the seissor components is hypothesized using engineering first principles to remain in the wake core. The free stream velocity near the tunnel walls should be recovered for the same free stream conditions.

The computational data for the 2011 (PIV) and 2013 (hot-wire anemometry) tests are compared in Fig. 55. The PIV data are presented in the local streamwise velocity,  $u$ , while the hot-wire data require a computed velocity,  $V_h$ , defined in 25. In the computational results for the configuration including the seissors, the  $u$  component of velocity compares very well with  $V_h$ , indicating that the contribution of the local three-dimensional velocity



(a) Top view



(b) Side view

Figure 53: Wake velocity measurement locations in space. (Red line indicates traverse of each profile).

perturbations remain in the core of the wake. This is confirmed with a consistent comparison of the local streamwise velocity,  $u$ , across the span extent of the tunnel. The superposition of the shear layers between the wake core and free stream indicate insignificant contributions from the addition of the scissors. The free stream outside of the wake is also identically recovered from both simulations, which is required if the free stream velocities are identical, as reported by the experimental efforts.<sup>52</sup>

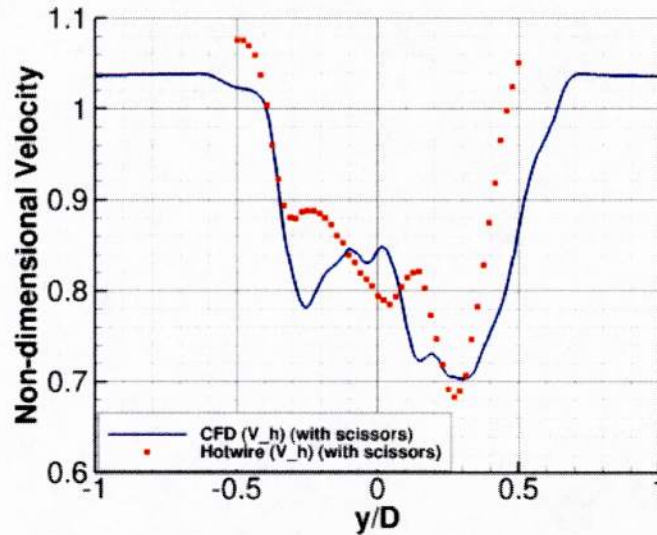


Figure 54: Comparison of computational and experimental wake velocity profiles at one hub diameter in the wake.

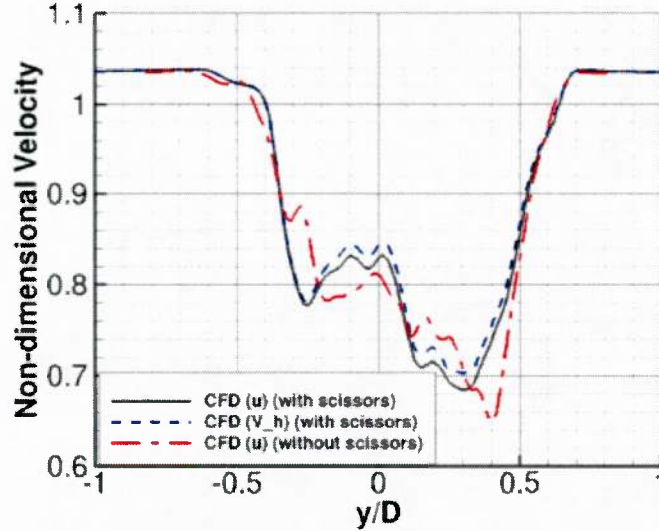


Figure 55: Comparison of computational wake velocity profiles at one hub diameter in the wake.

When the comparable experimental data are examined (Fig. 56), they exhibit a clear difference the wake extent and free stream recovery. Additionally, the bias toward the right of the wake due to rotational effects found in both PIV and computations does not appear in the hot-wire anemometry measurements. Similar trends in the local maxima and minima are generally observed for both methods but there is also appears to be a positive (upward) translational bias in the new hot-wire anemometry data. Therefore, a conclusion from this comparison would be that the scissors mitigate the wake drag, which is counterintuitive to first principles. As noted previously, there were no PIV data obtained for comparison against the configuration with scissors. When comparing the two computational and the two experimental methods on the same plot in Fig. 57, the experimental hot-wire results become a clear outlier. All other wake extents show good correlation with each other, although the effect of the scissors does effect the velocity profile in the core region.

The cause for the discrepancy in the hot-wire anemometry comparisons can not be confirmed given the available experimental data.<sup>52</sup> One hypothesis is that the tunnel free stream velocity may not have been identical to the velocity reported.<sup>52</sup> This hypothesis is supported in Fig. 56 since the free stream velocity is not recovered, and the expected wake core deficit was less than hypothesized. If the hot-wire data are translated to be coincident with the free stream velocity levels of the other results (Fig. 58), a portion of the expected results and improved correlation is observed. However, a larger right bias of the wake would be expected with a higher free stream velocity, so this may not be the source of the discrepancies. Other potential sources of error include a hub rotation rate different from the reported value, and/or errors associated with the  $V_h$  equation constants that are typically obtained from cal-

ibrations directly before and after the experiment. It was not possible to completely define the source(s) of the discrepancies without full access to and analysis of the experimental data, which was not available.

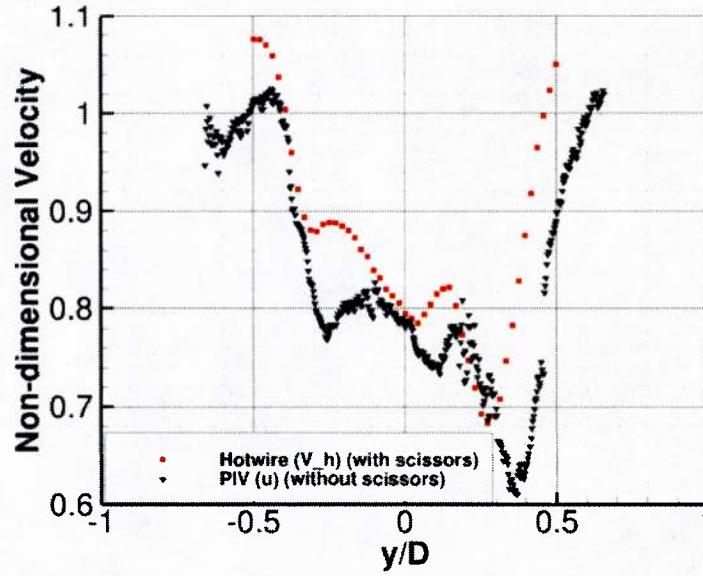


Figure 56: Comparison of experimental data with different measurement technique and addition of scissors.

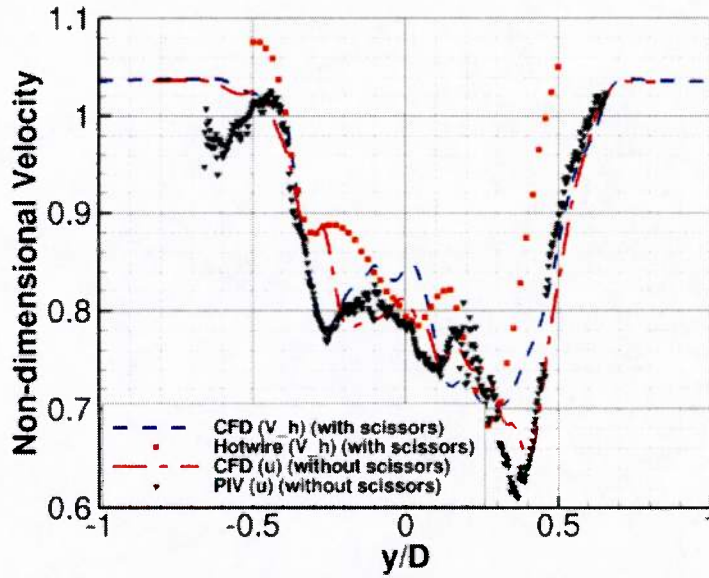


Figure 57: Overall comparison of both sets of CFD and experimental data.

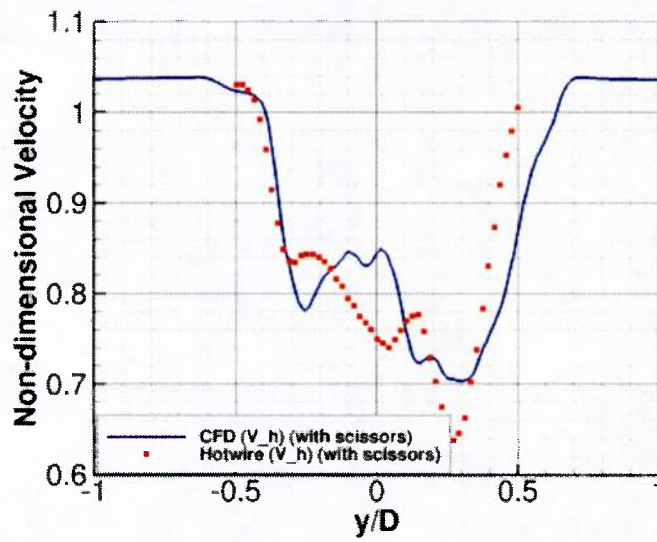
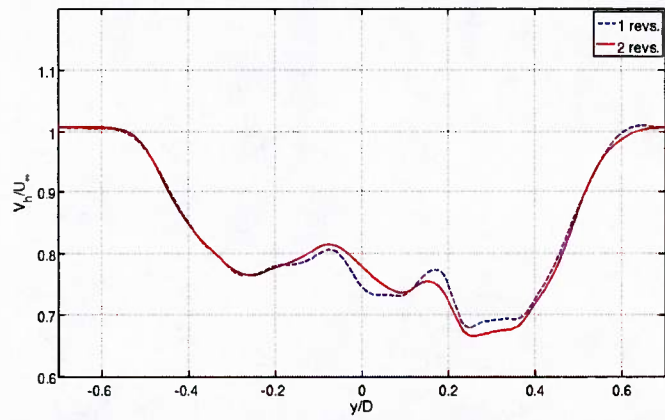


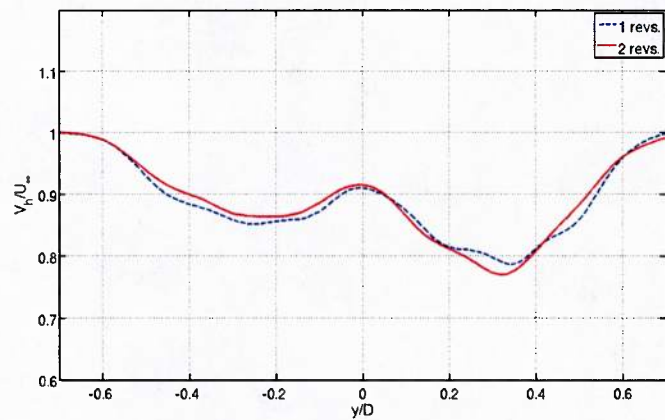
Figure 58: Comparison of computational and *translated* experimental wake velocity profiles at one hub diameter in the wake.

## 7.4 Wake Sensitivity to Averaging Sample Size

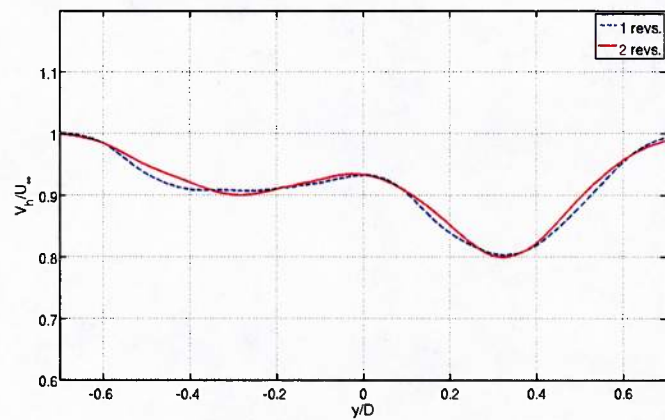
Mean velocity profiles can be obtained by time averaging the wake velocities after a fully developed flow field has been achieved. A study of the convergence (and periodicity) of the simulations can be made by varying the sampling window from one revolution to two revolutions. Figure 59 indicates that there minimal differences in the profiles when using the ultimate or both the final two revolutions of the simulation. The percent variation of the wake velocity deficit integral is 0.06%, 0.1%, 0.09% for the three downstream locations. Two revolutions of velocity data has been chosen as the sampling size for all time-averaged wake velocities.



(a)  $x = 1D$



(b)  $x = 2D$



(c)  $x = 3D$

Figure 59: Time-averaged wake velocity comparison at  $Z = 0.0$  m illustrating the effect of number of revolutions on the averaging of the wake velocity.

## 7.5 Mean Velocity Trends

Time-averaged velocity profiles resulting from the computational predictions at wake locations  $x = 1D$ ,  $x = 2D$ , and  $x = 3D$  for the different free stream velocities at a rotation speed of 240 rpm is shown in Figs. 60 – 62. Several observations can be made. The velocity deficit generally decreases (the wake velocity approaches the free stream recovery) at a given spanwise location as the downstream distance from the hub increases. This decrease is not linear with respect to the distance, rather most recovery occurs during one to two hub diameters downstream. Additionally, the increase in downstream distance tends to diffuse or smooth the local extrema in the core. The wake bias toward the right (advancing side) decreases as the downstream distance increases, with the maximum changes before two hub diameters in the wake is reached. This wake skew is apparent by the larger velocity deficits on the wake's advancing side.

As the free stream velocity increases (higher advance ratios), the asymmetry of the wake diminishes in the wake locations examined. This implies that at higher advance ratios the wake skew tends to disappear, which is expected since the effect of rotation is limited due to the dominance of the free stream energy.

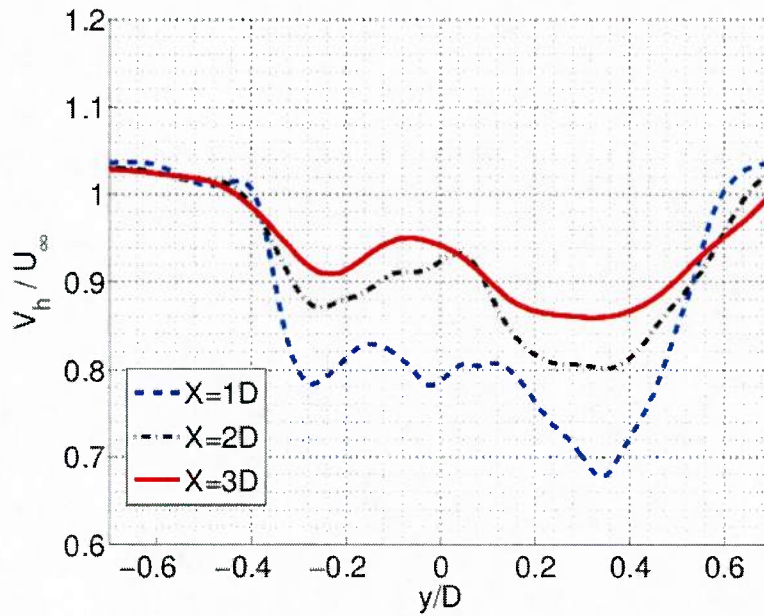


Figure 60: Time-averaged wake velocity comparison at  $Z = 0.0$  m at different downstream locations. The rotor hub conditions are at 240 rpm and  $U_\infty = 8.941$  m/s.

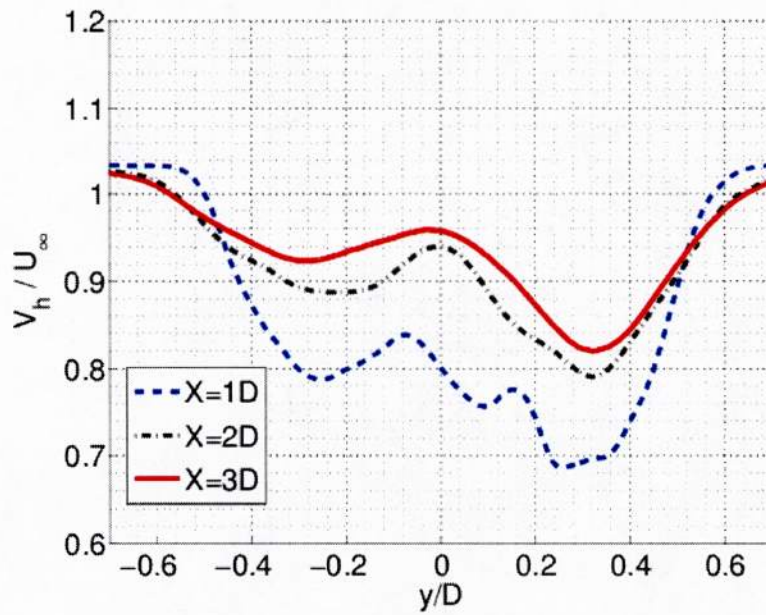


Figure 61: Time-averaged wake velocity comparison at  $Z = 0.0$  m at different downstream locations. The rotor hub conditions are at 240 rpm and  $U_\infty = 13.41\text{m/s}$ .

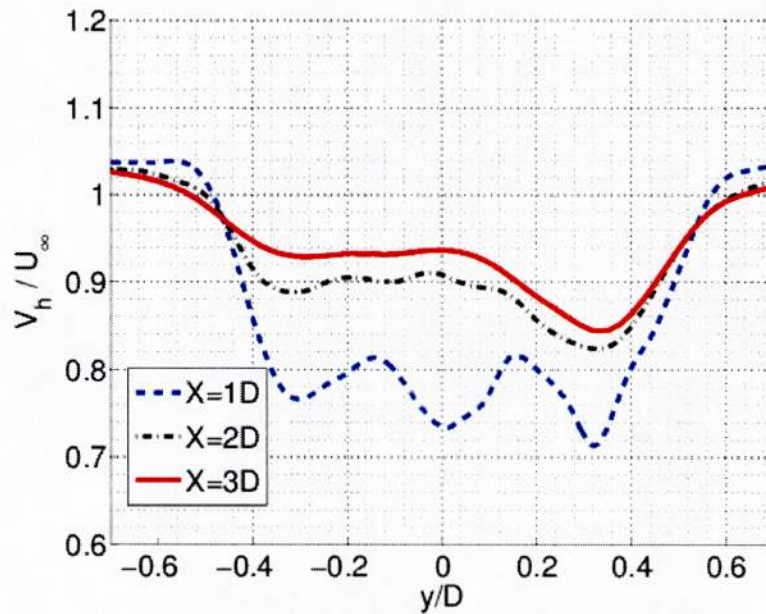
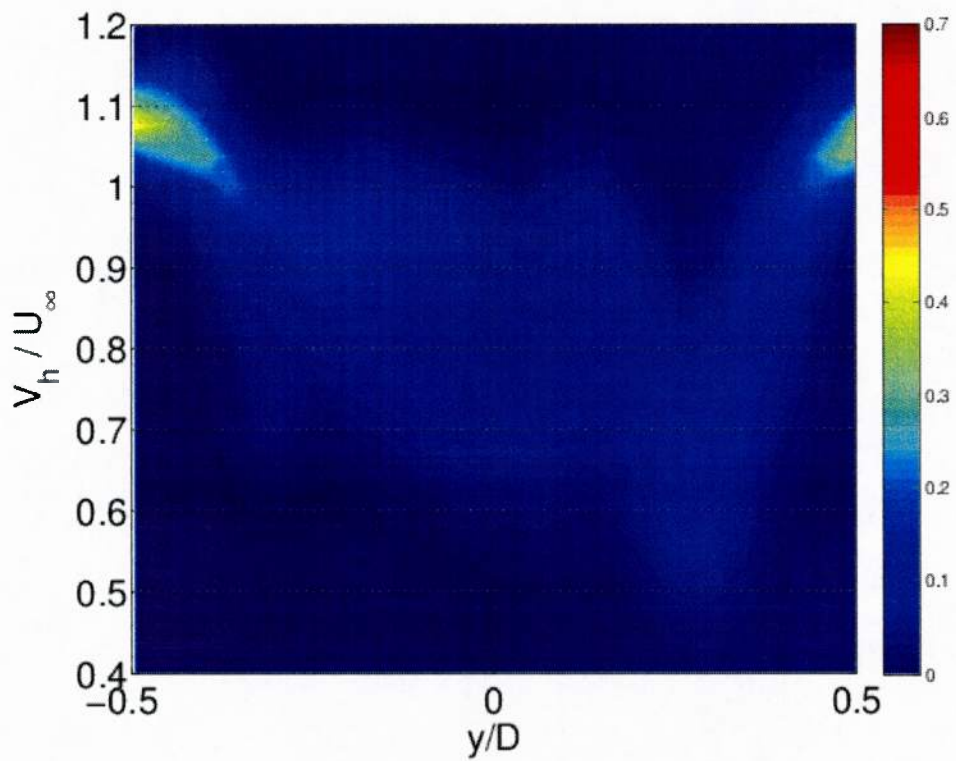


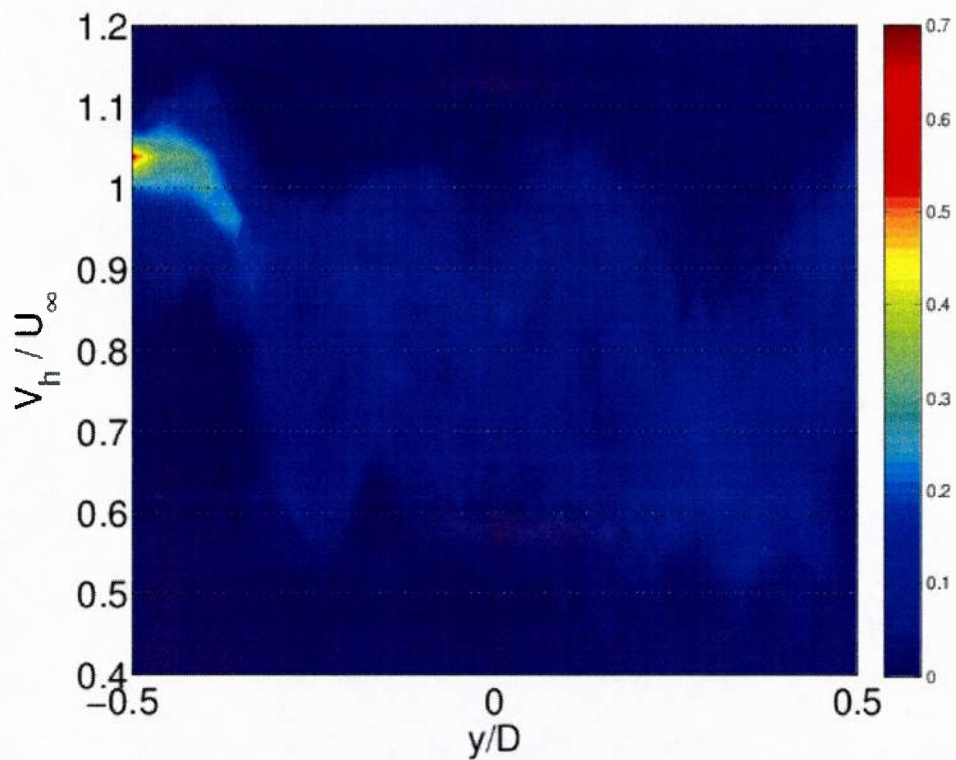
Figure 62: Time-averaged wake velocity comparison at  $Z = 0.0$  m at different downstream locations. The rotor hub conditions are at 240 rpm and  $U_\infty = 22.35\text{m/s}$ .

## 7.6 Velocity Histograms and Central Moments

In order to compare the distribution of different effective velocities measured in the wake between the experimental and computational results, histograms of the both data sets at different wake locations have been compared and assessed. In Figs. 63 - 68, the general shape of the distributions show good correlation in the velocity axis, although the velocity translation noted in Section 7.3 is evident. This implies that the computation accurately captures the general range of experimental velocities with a similar distribution. The experimental data appear much smoother than the computation data as the number of computational samples is much larger. The histograms indicate that the general trend is followed between both data sets. The experimental data set exhibits a shift in the  $-y$  direction (leftward) by about  $\Delta y = -0.1D$ .



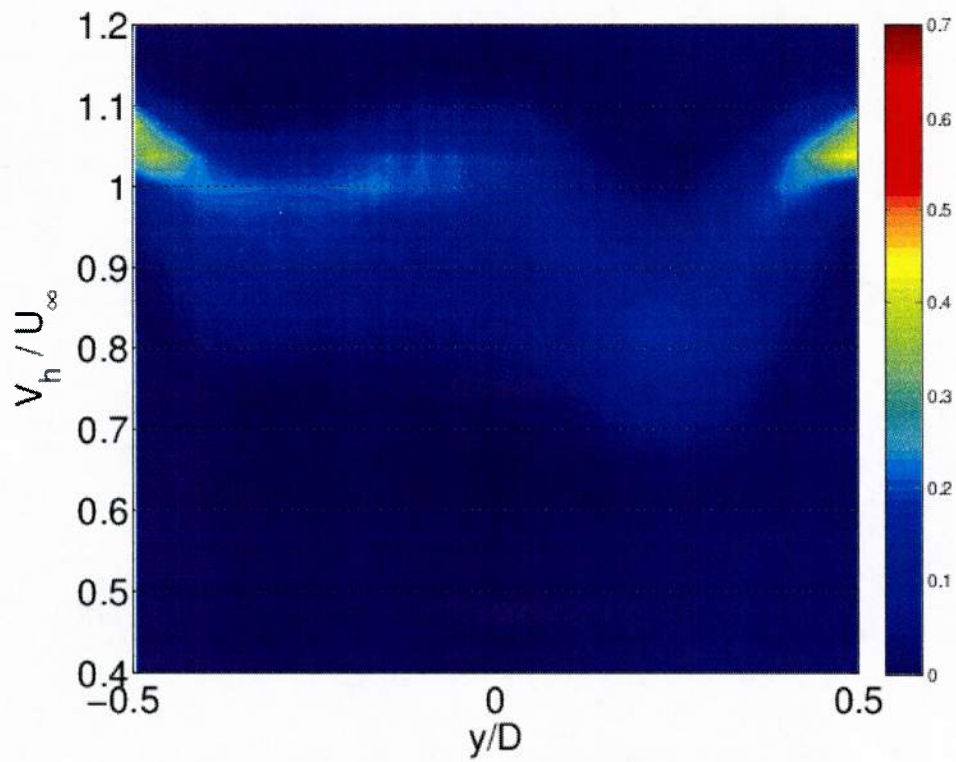
(a) Experiment



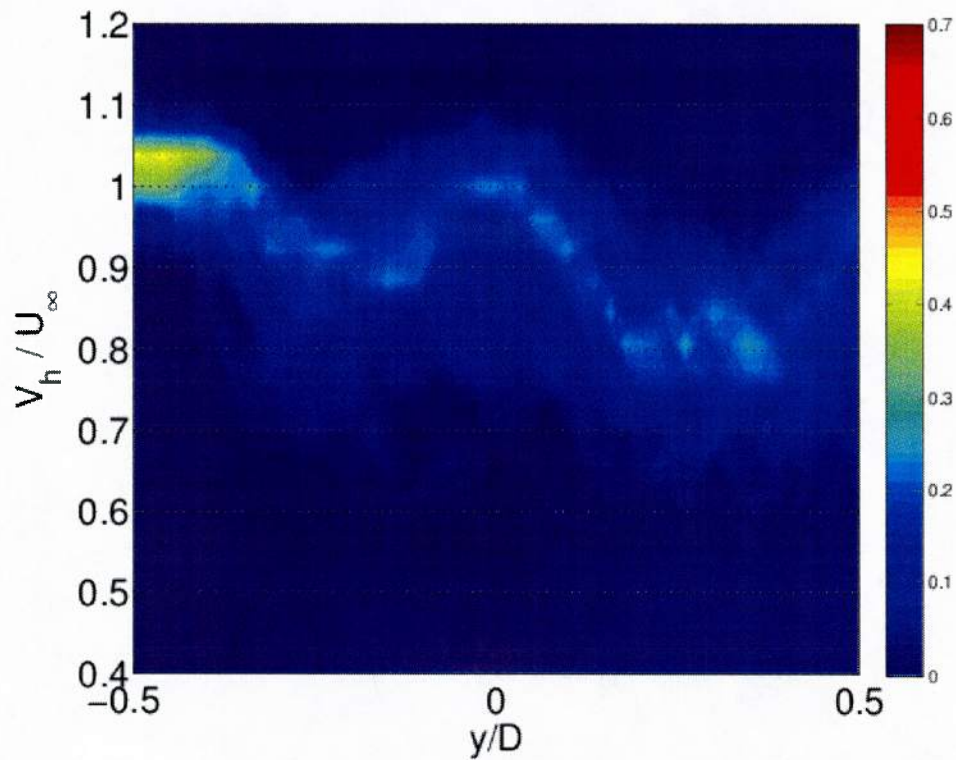
(b) CFD

90

Figure 63: Histogram comparison at  $Z = 0.0$  m and  $X = 1D$ . The rotor hub conditions are at 240 rpm and  $U_\infty = 8.941$  m/s.



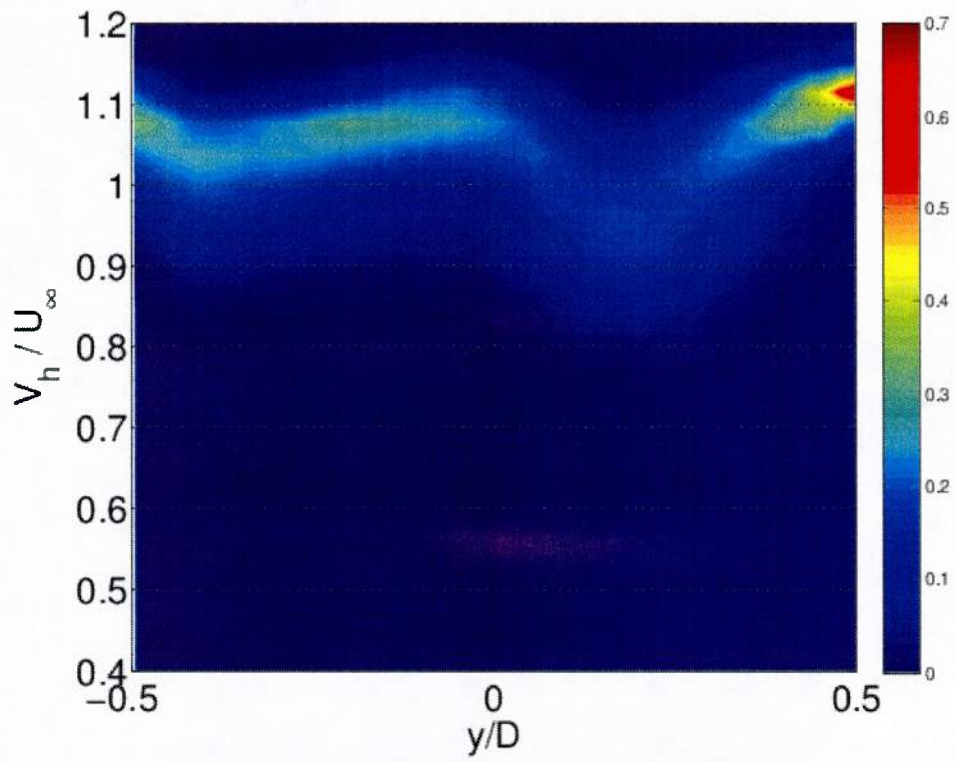
(a) Experiment



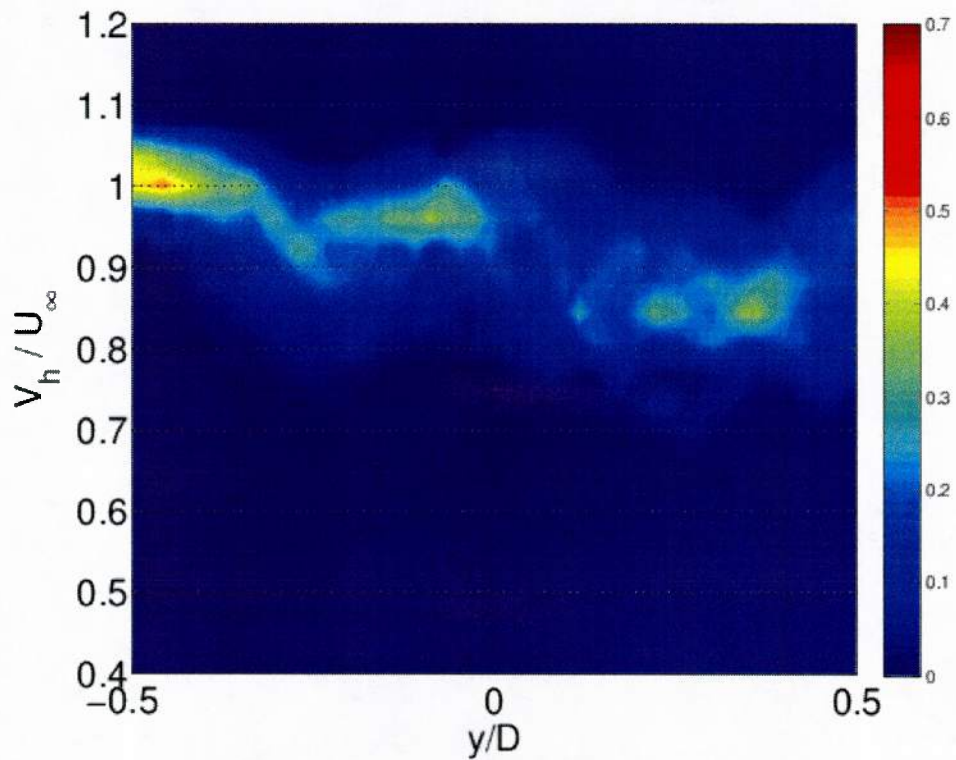
(b) CFD

91

Figure 64: Histogram comparison at  $Z = 0.0$  m and  $X = 2D$ . The rotor hub conditions are at 240 rpm and  $U_\infty = 8.941$  m/s.



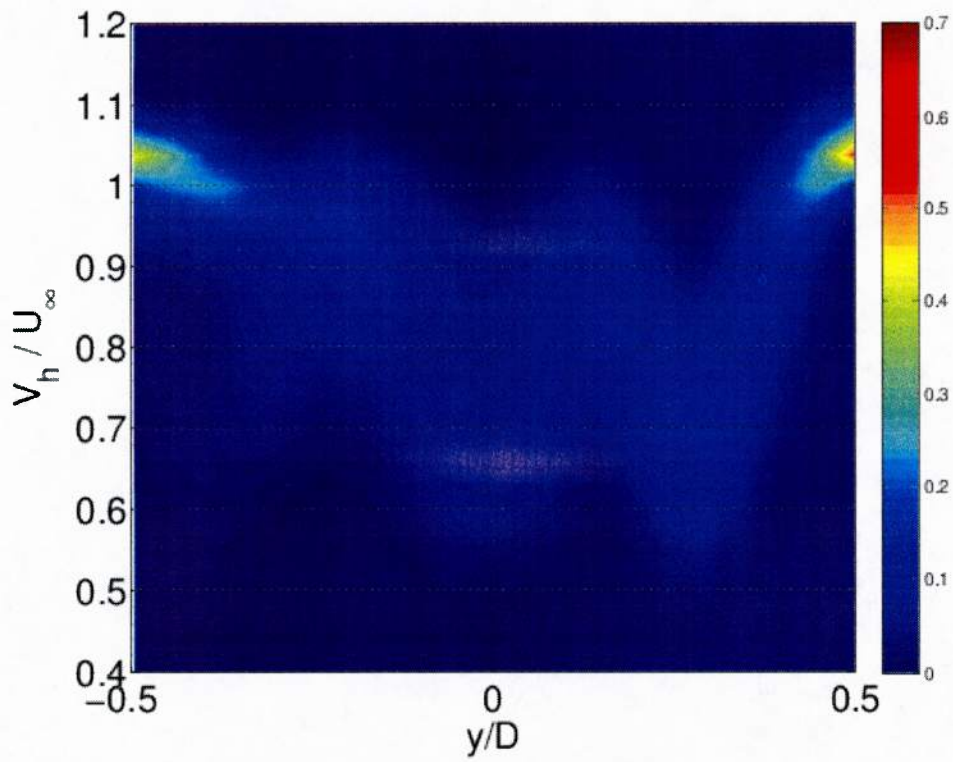
(a) Experiment



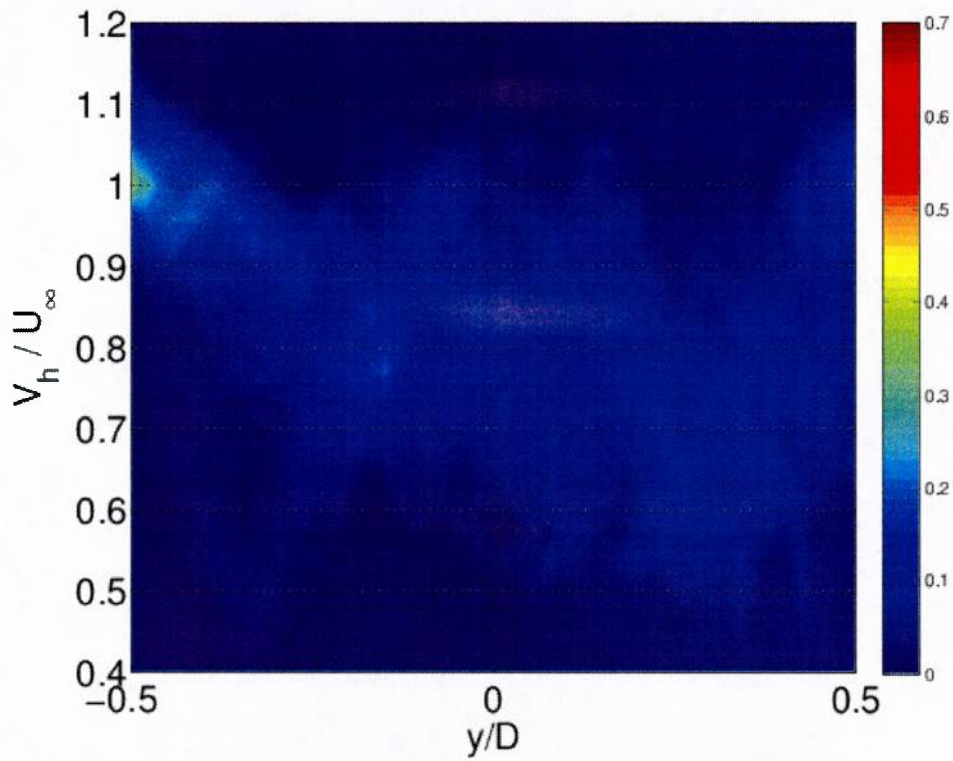
(b) CFD

92

Figure 65: Histogram comparison at  $Z = 0.0$  m and  $X = 3D$ . The rotor hub conditions are at 240 rpm and  $U_\infty = 8.941$  m/s.

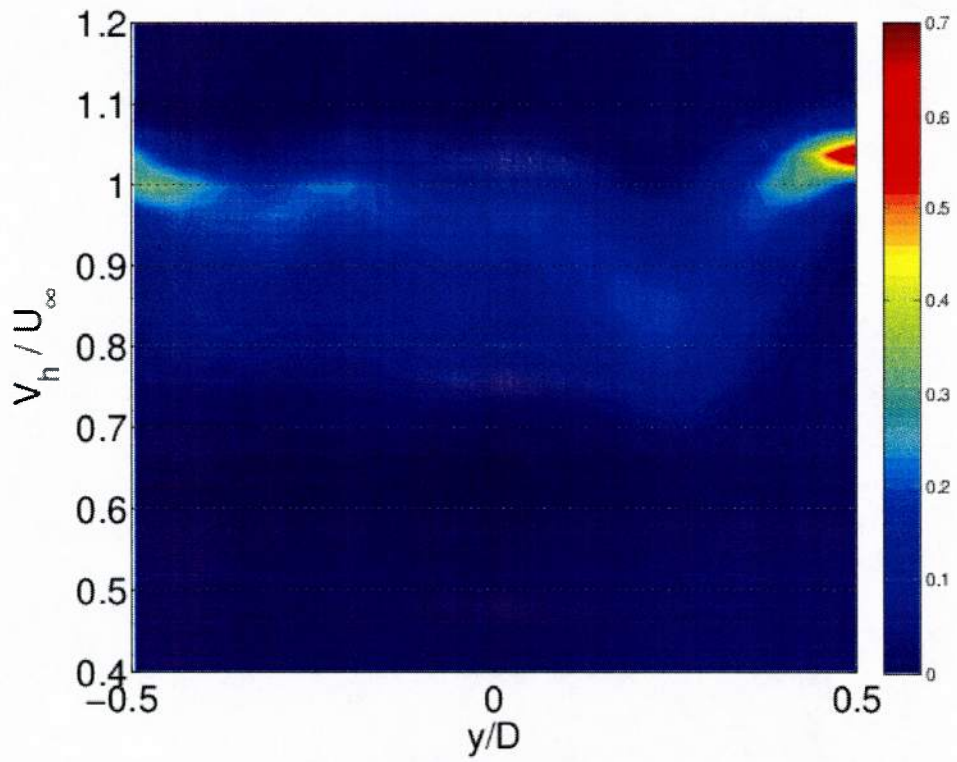


(a) Experiment

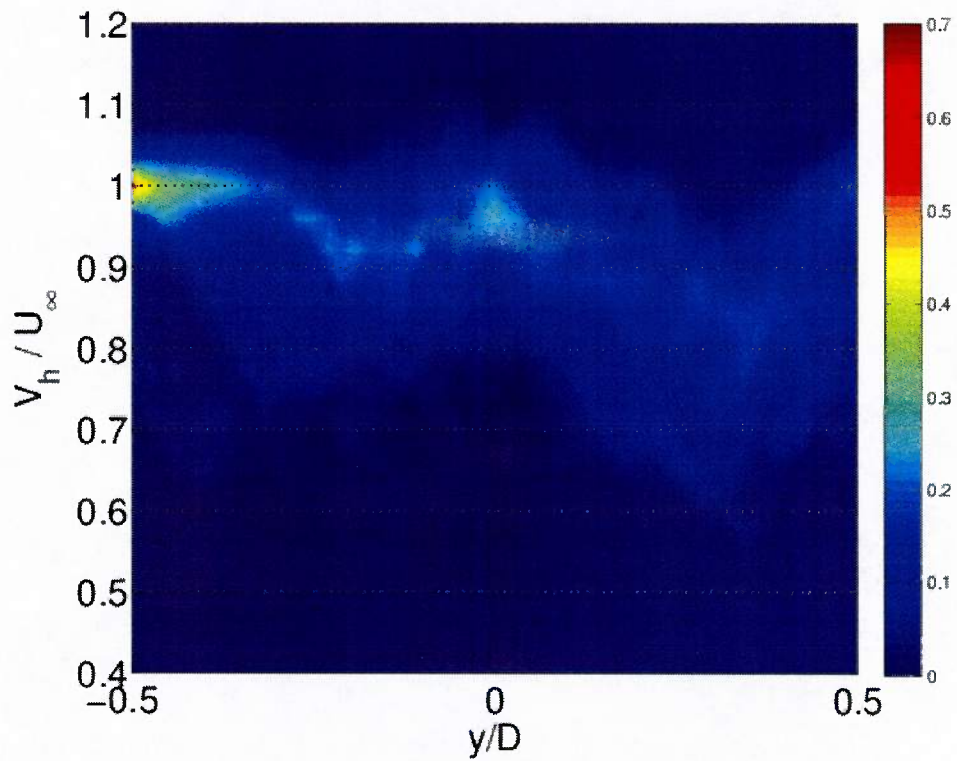


(b) CFD

Figure 66: Histogram comparison at  $Z = 0.0$  m and  $X = 1D$ . The rotor hub conditions are at 240 rpm and  $U_\infty = 13.41$  m/s.

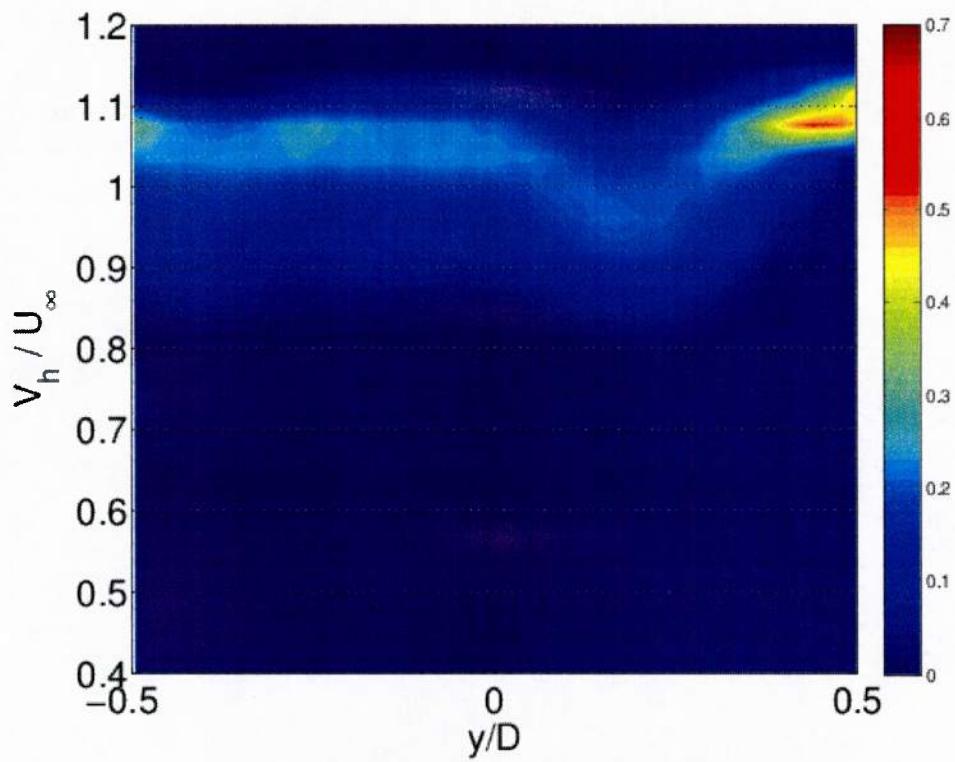


(a) Experiment

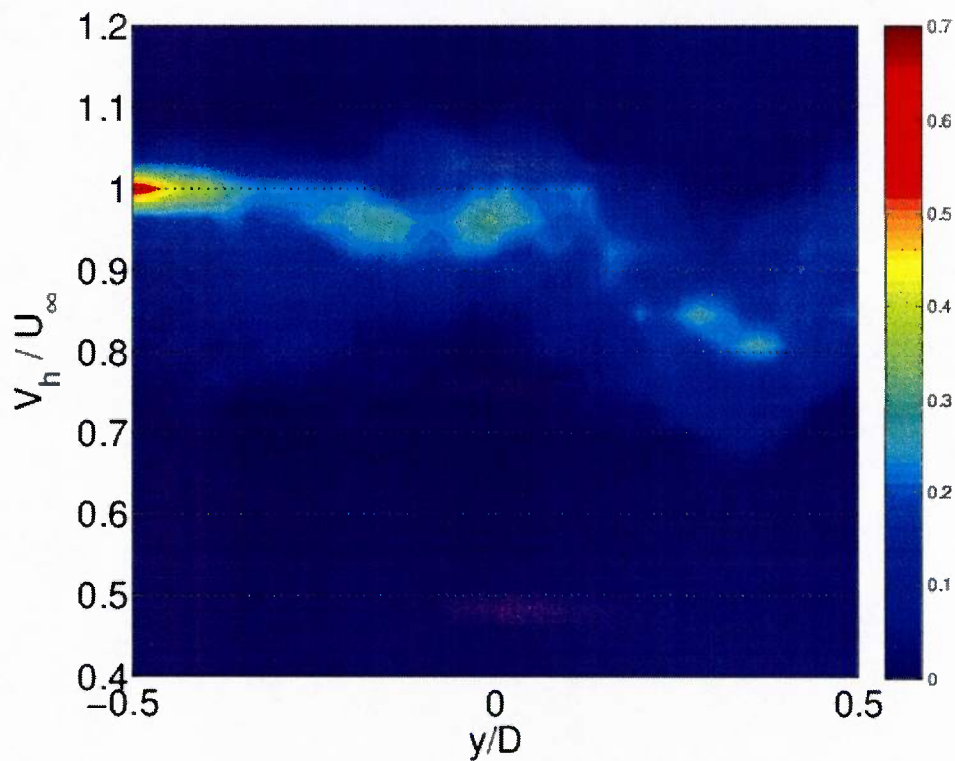


(b) CFD

Figure 67: Histogram comparison at  $Z = 0.0$  m and  $X = 2D$ . The rotor hub conditions are at 240 rpm and  $U_\infty = 13.41$  m/s.



(a) Experiment



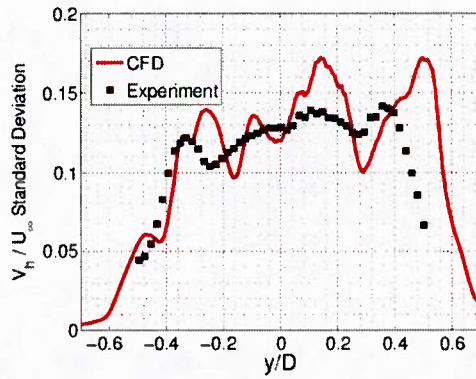
(b) CFD

95

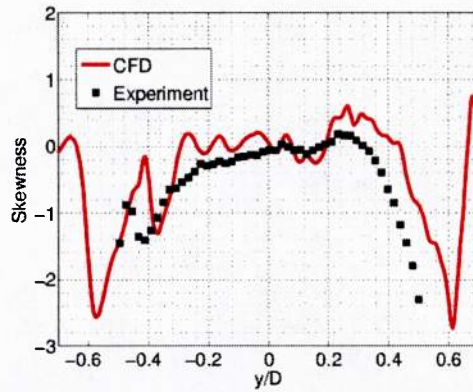
Figure 68: Histogram comparison at  $Z = 0.0$  m and  $X = 3D$ . The rotor hub conditions are at 240 rpm and  $U_\infty = 13.41$  m/s.

Central moment statistics provide additional details about the distributions. The standard deviation, which arises from the second central moment, shows dispersion of the data away from the mean. The skewness, the third central moment, enables understanding of bias of the data above or below the mean. Finally, the kurtosis or distribution slope, the fourth central moment, denotes the probability of extreme events. High kurtosis implies a higher probability of outliers and indicates a distribution with longer tails. A Gaussian distribution will have zero skewness and a kurtosis value of three.

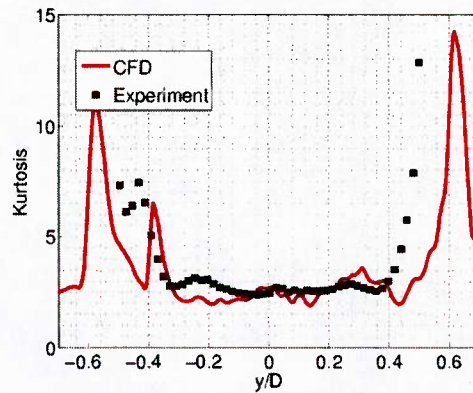
Figures 69 - 74 plot the experimental and computation distributions of standard deviation, skewness, and kurtosis. The values of standard deviation, skewness, and kurtosis correlate well between computational and experiment, especially in the middle of the wake ( $-0.4 < y/D < 0.4$ ). Again, the experimental statistics are smoother than that of computations, similar to the histograms. The skewness and kurtosis plots of both data sets indicate that the mid-wake velocities have distributions close to Gaussian distribution. The skewness shows that the velocities are slightly biased lower than the mean velocities. In common with the prior data analyses, there is a clear shift in the wake extent of the experimental data. From a statistical point of view, the two data sets give reasonable correlation, with the only major differences being the smoothness of the data and the bias of the wake in the experimental data.



(a) Standard Deviation

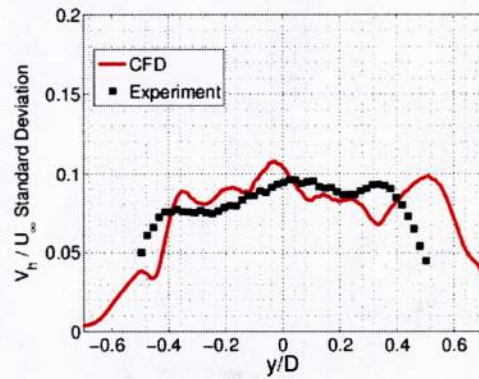


(b) Skewness

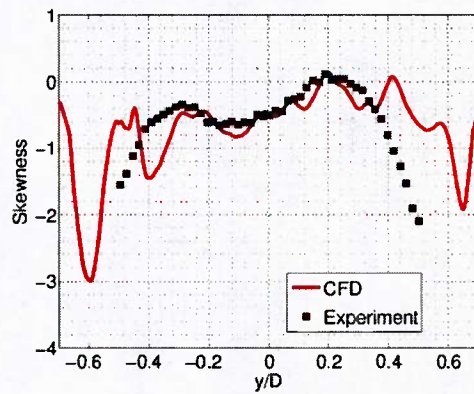


(c) Kurtosis

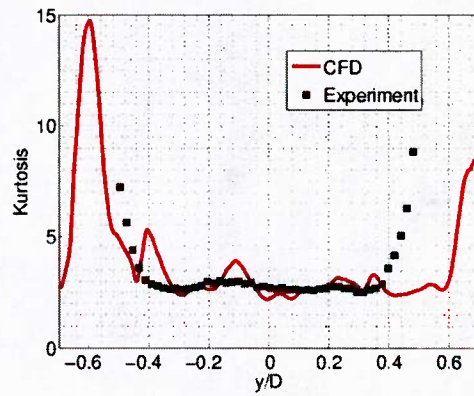
Figure 69: Comparison of statistical central moments from adapted grid at  $Z = 0.0$  m and  $X = 1D$ . The rotor hub conditions are at 240 rpm and  $U_\infty = 8.941$  m/s.



(a) Standard Deviation

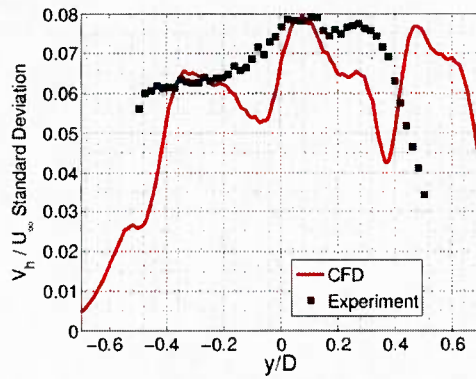


(b) Skewness

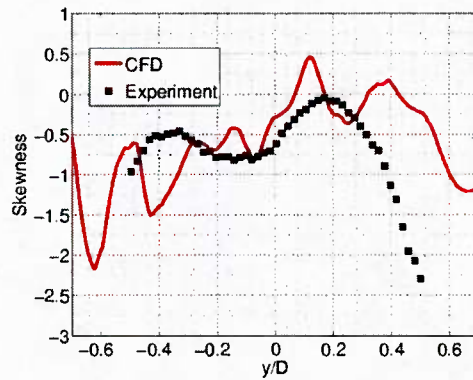


(c) Kurtosis

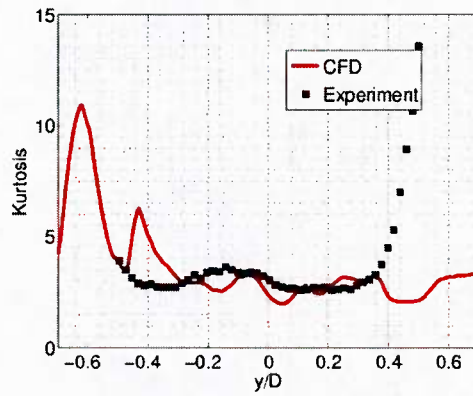
Figure 70: Comparison of statistical central moments from adapted grid at  $Z = 0.0$  m and  $X = 2D$ . The rotor hub conditions are at 240 rpm and  $U_\infty = 8.941$  m/s.



(a) Standard Deviation

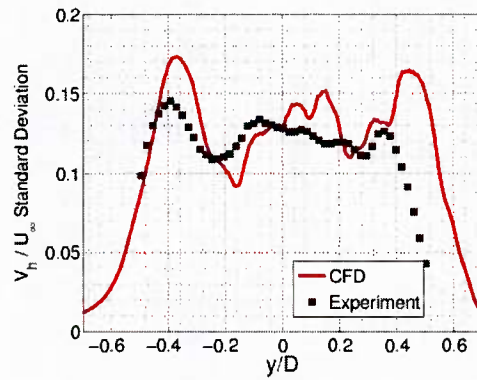


(b) Skewness

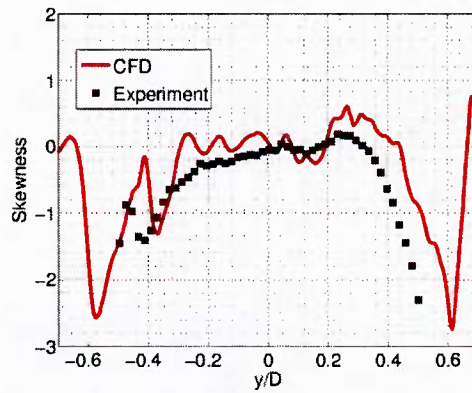


(c) Kurtosis

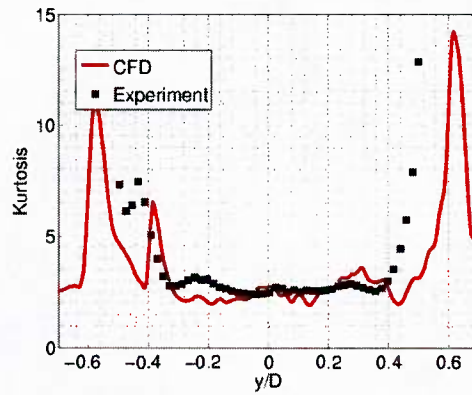
Figure 71: Comparison of statistical central moments from adapted grid at  $Z = 0.0$  m and  $X = 3D$ . The rotor hub conditions are at 240 rpm and  $U_\infty = 8.941\text{m/s}$ .



(a) Standard Deviation

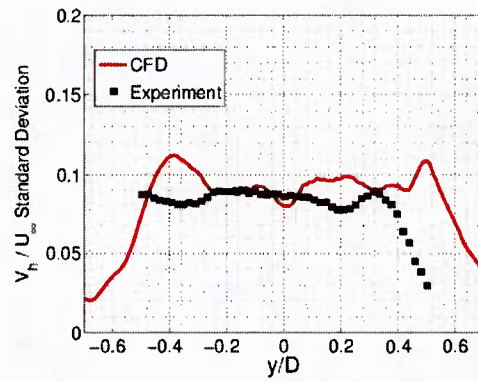


(b) Skewness

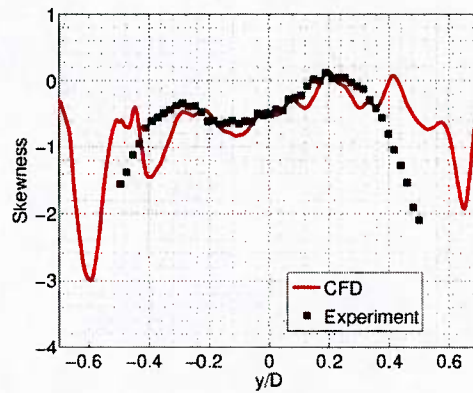


(c) Kurtosis

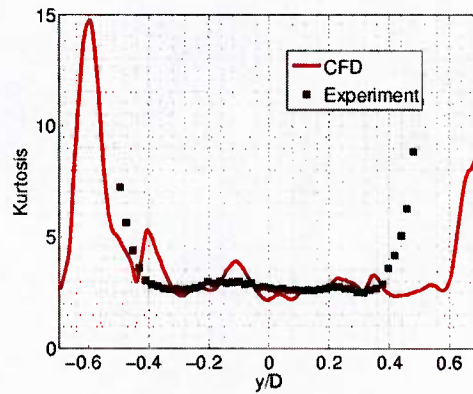
Figure 72: Comparison of statistical central moments from adapted grid at  $Z = 0.0$  m and  $X = 1D$ . The rotor hub conditions are at 240 rpm and  $U_\infty = 13.41$  m/s.



(a) Standard Deviation

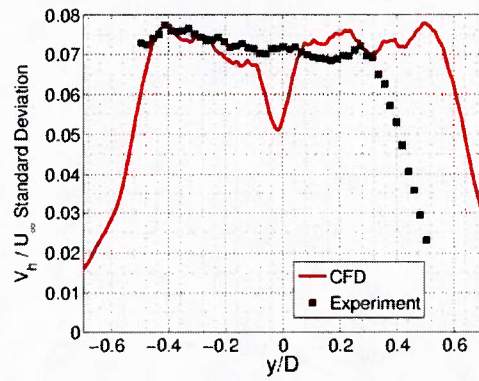


(b) Skewness

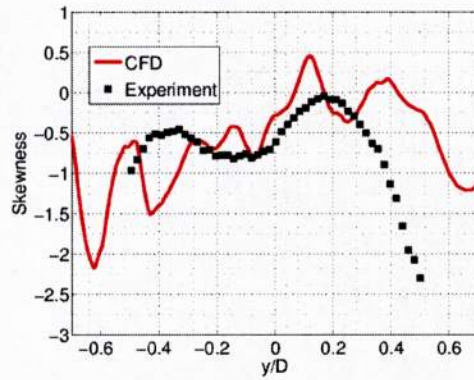


(c) Kurtosis

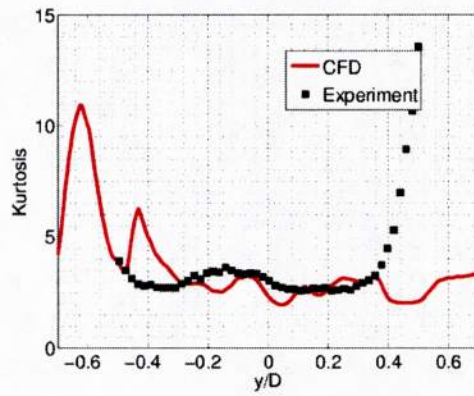
Figure 73: Comparison of statistical central moments from adapted grid at  $Z = 0.0$  m and  $X = 2D$ . The rotor hub conditions are at 240 rpm and  $U_\infty = 13.41$  m/s.



(a) Standard Deviation



(b) Skewness



(c) Kurtosis

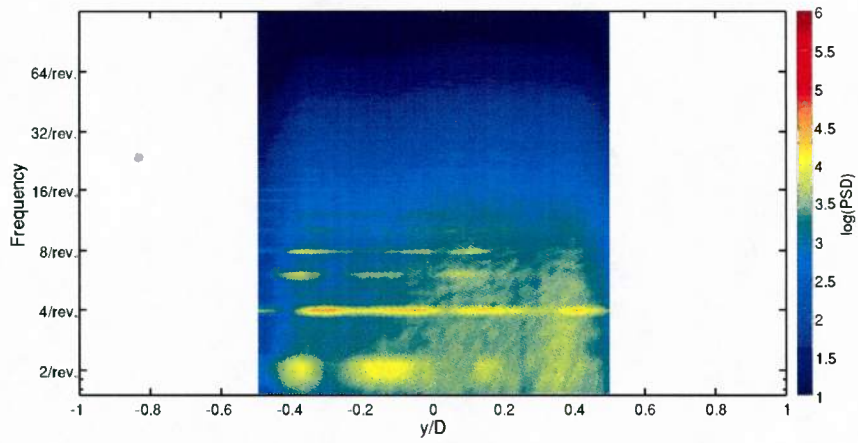
Figure 74: Comparison of statistical central moments from adapted grid at  $Z = 0.0$  m and  $X = 3D$ . The rotor hub conditions are at 240 rpm and  $U_\infty = 13.41$  m/s.

## 7.7 Velocity Spectral Analysis

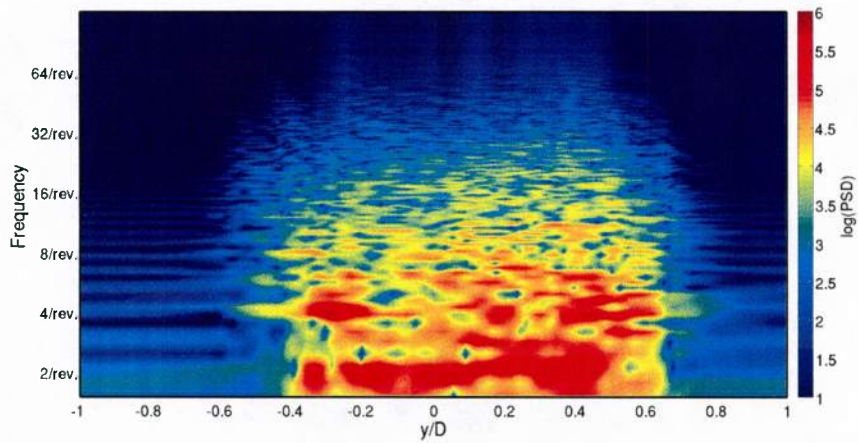
Wake velocity spectra from experiment and computation are plotted and compared in Figs. 75 - 80 at the hub level ( $Z = 0.0$  m). The contours indicate the power spectral density (in logarithmic scale). The frequency axis is in the vertical direction, marked by the per-rev frequency so that wake structures may be traced to their originating geometry. Noting that the contour ranges are the same for both computation and experiment, a general trend is observed that the computational predictions for the power spectra content are greater than their experimental counterparts. Also, since the computational data are averaged for many more data points over the span and over two revolutions, the data appear to be noisy. However, clear correlations are observed particularly in the data at the four-per-rev and two-per-rev levels.

The four-per-rev levels structures are generally present over the range the of the wake, but they are much stronger in the retreating portion of the wake (left side of the plots). These structures emanate primarily from the blade shanks and pitch links. These structures also persist to the  $X = 3D$  downstream location, the farthest point measured by experiment. The eight-per-rev and sixteen-per-rev content are much stronger for  $U_\infty = 13.41$  m/s, but they diminish more rapidly at the downstream locations compared to the four-per-rev structures. Most of these structures are strongest in the retreating portion of the wake, where the spanwise mixing of the flow is much less compared to the advancing rotor wake due to the skewed wake shape. A considerable two-per-rev shedding is also observed in both sets of data and is intermittently prominent across the wake.

Additionally, traces of six-per-rev shedding are observed. This corresponds to a frequency of 24 Hz, which can be attributed to the vortex shedding off the blade shanks ( $D = 0.0349$  m)ee. Sakamoto and Arie<sup>98</sup> have observed that for cylinders of aspect ratio 2.5, which corresponds to the aspect ratio of the blade shanks, the Strouhal number ( $St = \frac{fD}{V}$ ) can vary between 0.11 and 0.14, depending on the portion of the cylinder submerged in the boundary layer. Using the tip speed  $V_{tip}$ , as the characteristic velocity of shedding, a Strouhal number of 0.135 is obtained for this configuration. Therefore, the six-per-rev structures here can be traced to the rotating blade root. This is similar to the findings reported by Reich et al.,<sup>21</sup> where a six-per-rev wake structure was attributed to a Strouhal shedding due to the hub arms of a four-bladed rotor hub.

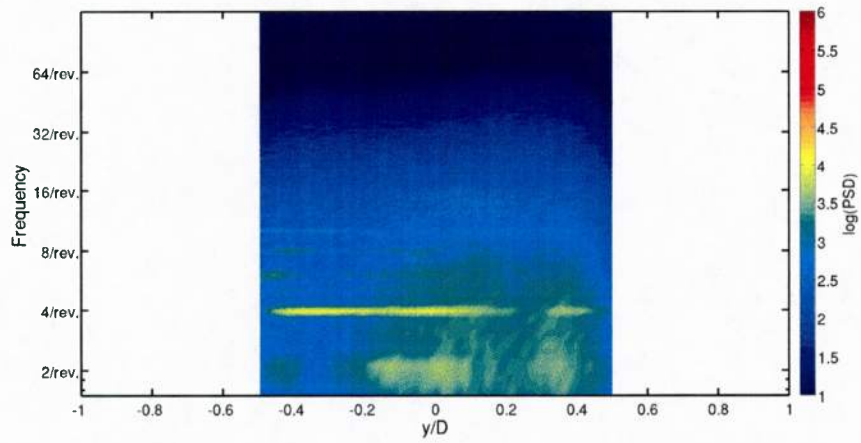


(a) Experiment

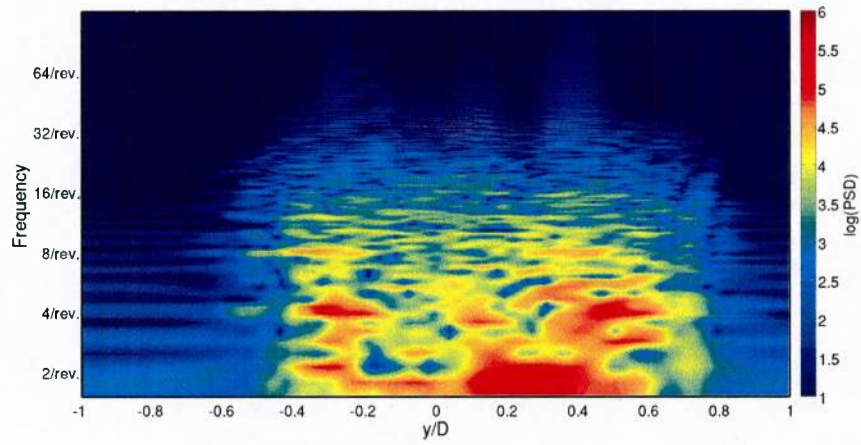


(b) CFD

Figure 75: Wake PSD comparison at  $Z = 0.0$  m and  $X = 1D$ . The rotor hub conditions are at 240 rpm and  $U_\infty = 8.941$  m/s.

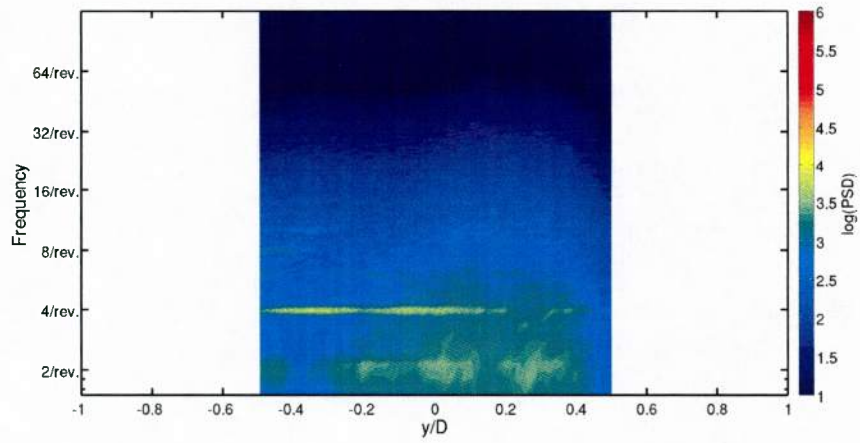


(a) Experiment

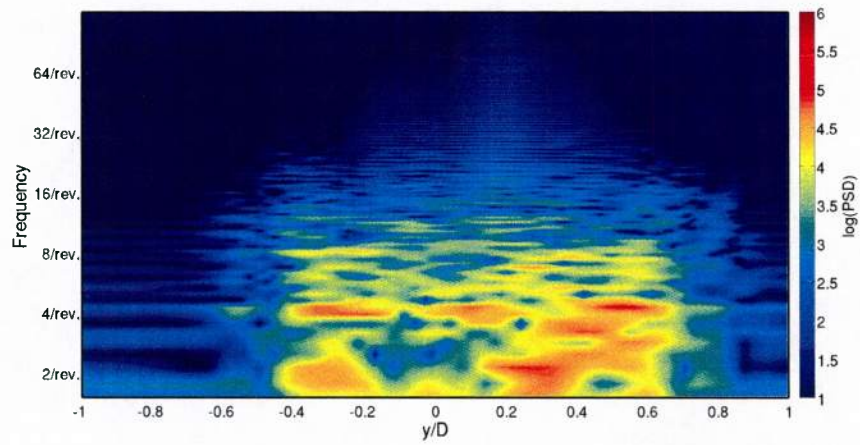


(b) CFD

Figure 76: Wake PSD comparison at  $Z = 0.0$  m and  $X = 2D$ . The rotor hub conditions are at 240 rpm and  $U_{\infty} = 8.941$  m/s.

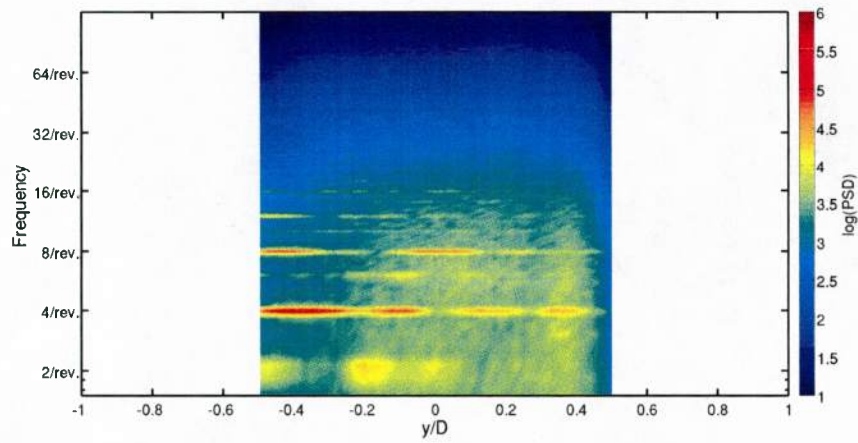


(a) Experiment

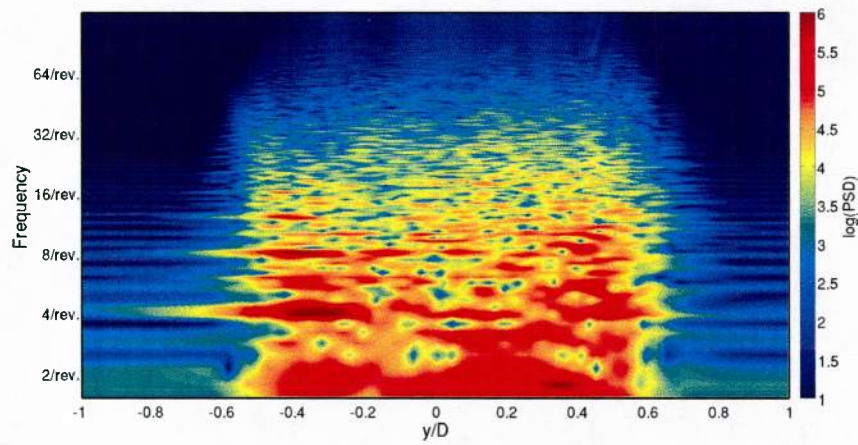


(b) CFD

Figure 77: Wake PSD comparison at  $Z = 0.0$  m and  $X = 3D$ . The rotor hub conditions are at 240 rpm and  $U_\infty = 8.941$  m/s.

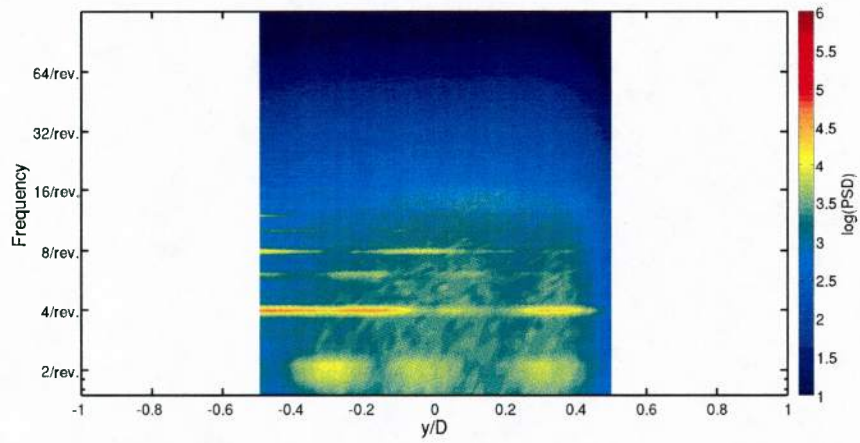


(a) Experiment

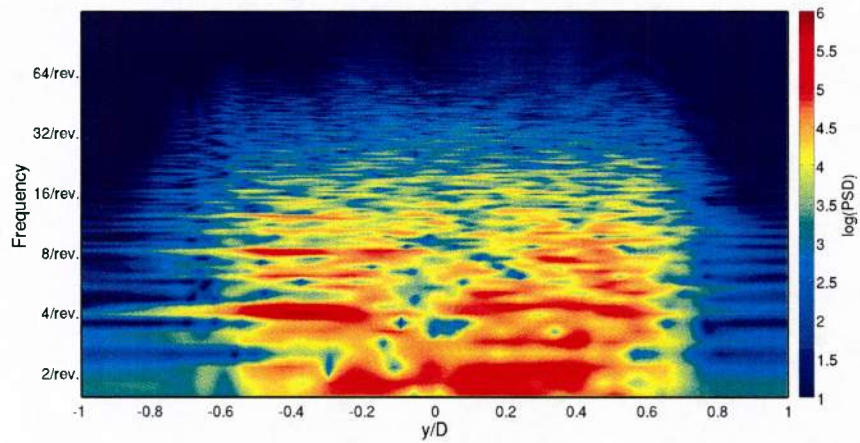


(b) CFD

Figure 78: Wake PSD comparison at  $Z = 0.0$  m and  $X = 1D$ . The rotor hub conditions are at 240 rpm and  $U_{\infty} = 13.41$  m/s.

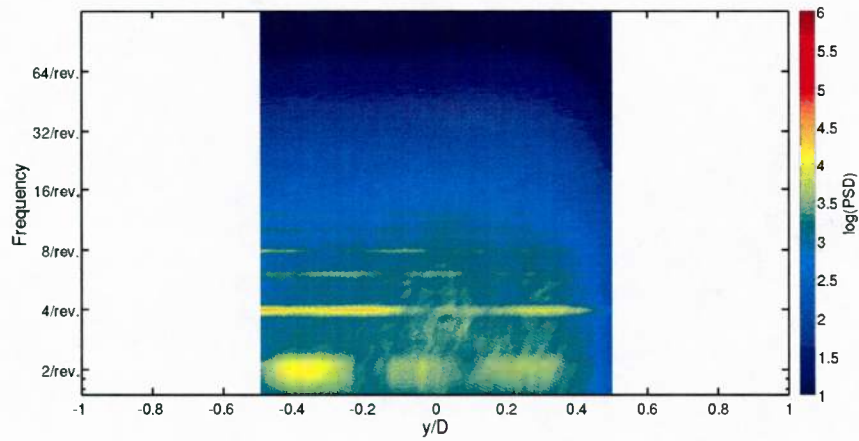


(a) Experiment

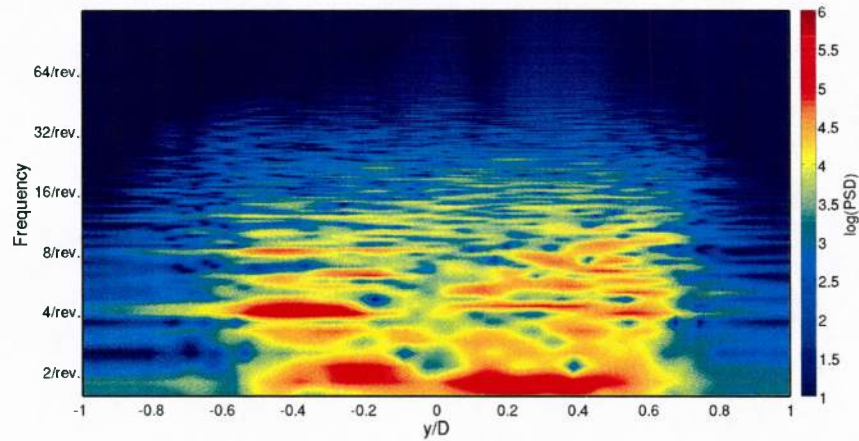


(b) CFD

Figure 79: Wake PSD comparison at  $Z = 0.0$  m and  $X = 2D$ . The rotor hub conditions are at 240 rpm and  $U_\infty = 13.41$  m/s.



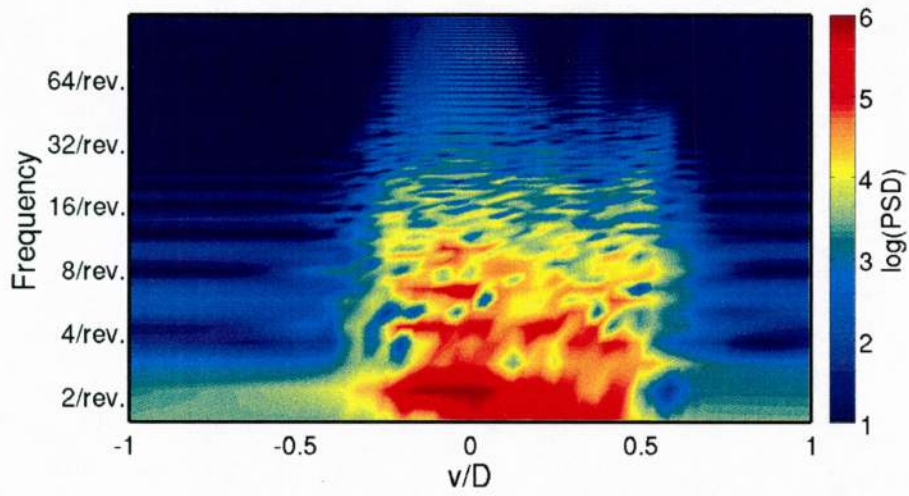
(a) Experiment



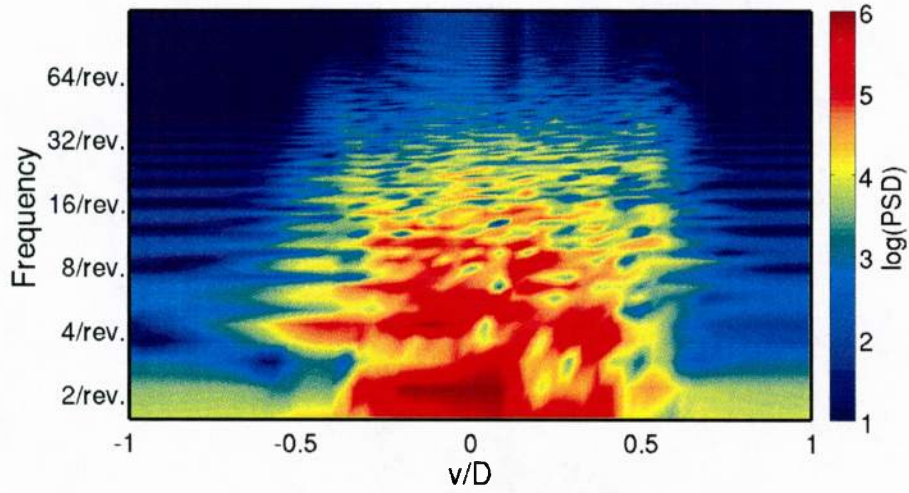
(b) CFD

Figure 80: Wake PSD comparison at  $Z = 0.0$  m and  $X = 3D$ . The rotor hub conditions are at 240 rpm and  $U_\infty = 13.41$  m/s.

Figures 81- 83 plot the computational velocity spectra in the wake at  $Z = -0.204D$ , illustrating the wake character at behind the scissors geometry. Unlike the wake at the hub level ( $Z = 0.0$ ), the wake extent here is narrower, but the rightward bias is still observed, which is expected. It is clear that in addition to the four-per-rev structures, there are also two-per-rev structures that are not as prominently at the hub level. The two-per-rev structure persists strongly up until the  $X = 3D$  location whereas the four-per-rev features tend to diminish.

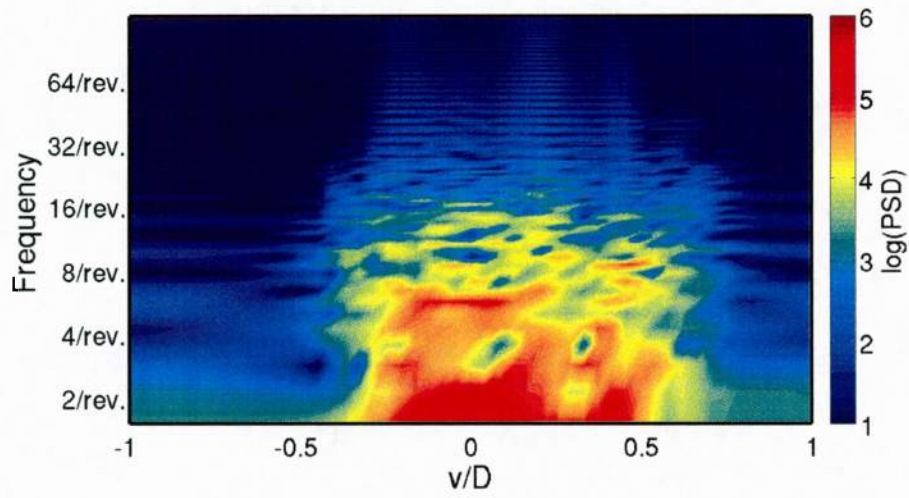


(a)  $U_\infty = 8.941\text{m/s}$

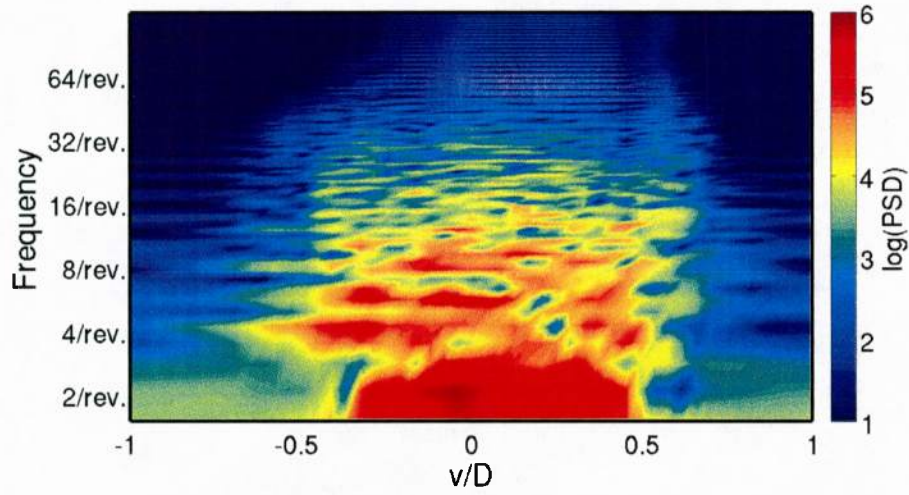


(b)  $U_\infty = 13.41\text{m/s}$

Figure 81: Wake PSD comparison at  $Z = -0.204D$  and  $X = 1D$  at 240 rpm.

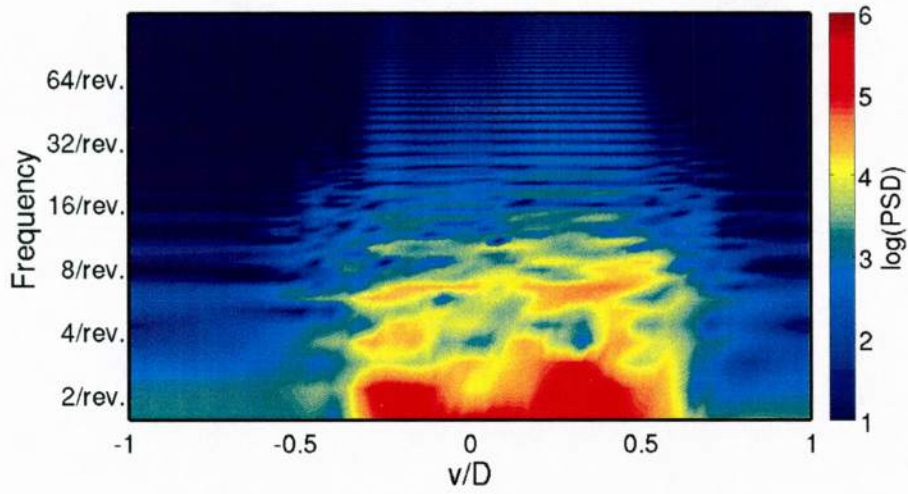


(a)  $U_\infty = 8.941\text{m/s}$

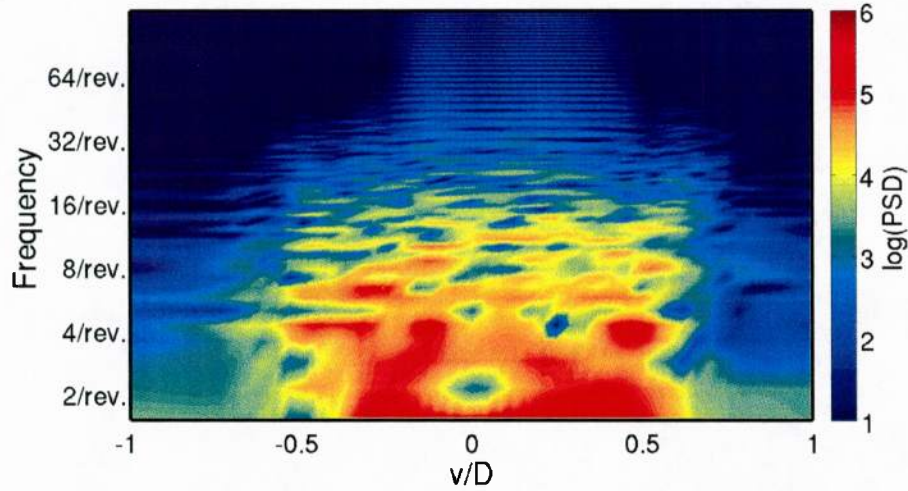


(b)  $U_\infty = 13.41\text{m/s}$

Figure 82: Wake PSD comparison at  $Z = -0.204D$  and  $X = 2D$  at 240 rpm.



(a)  $U_\infty = 8.941$  m/s



(b)  $U_\infty = 13.41$  m/s

Figure 83: Wake PSD comparison at  $Z = -0.204D$  and  $X = 3D$  at 240 rpm.

## 7.8 Long-age Wake Analysis

Figure 84 shows the capability of the current computational methodology. That is, a computational analysis that combines an adaptive grid capability with LES wake modeling enables the capture, in a computationally efficient manner, of the velocity spectra much farther in the wake, here at five diameters downstream. Experimental data are not available at locations beyond  $X = 3D$  due to the limitations of the test section dimensions. The flattening of the spectra at high frequencies indicates that further simulation time is required, but

the predictions are parallel to the 5/3 law at lower frequencies note that the simulation is capturing those turbulent scales. In addition, the harmonics associated with the different components are also still visible. For the  $Y = -D/2$  location, the four-per, six-per, eight-per, and twelve-per revolution are captured, similar to that of .<sup>21</sup> There were no two-per-rev structures as this configuration studied did not include the scissors.

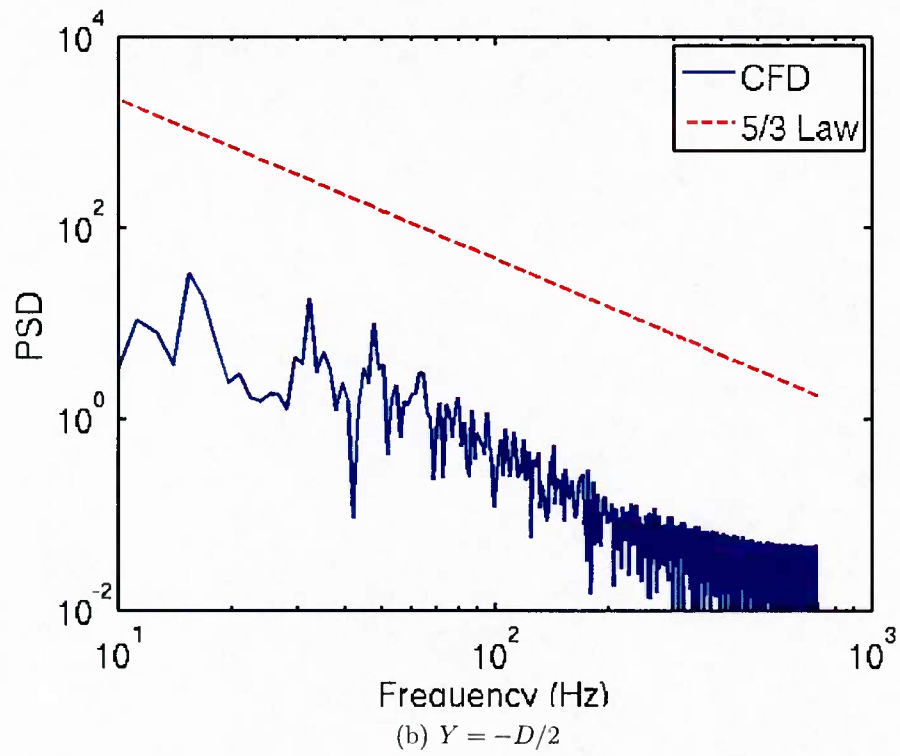
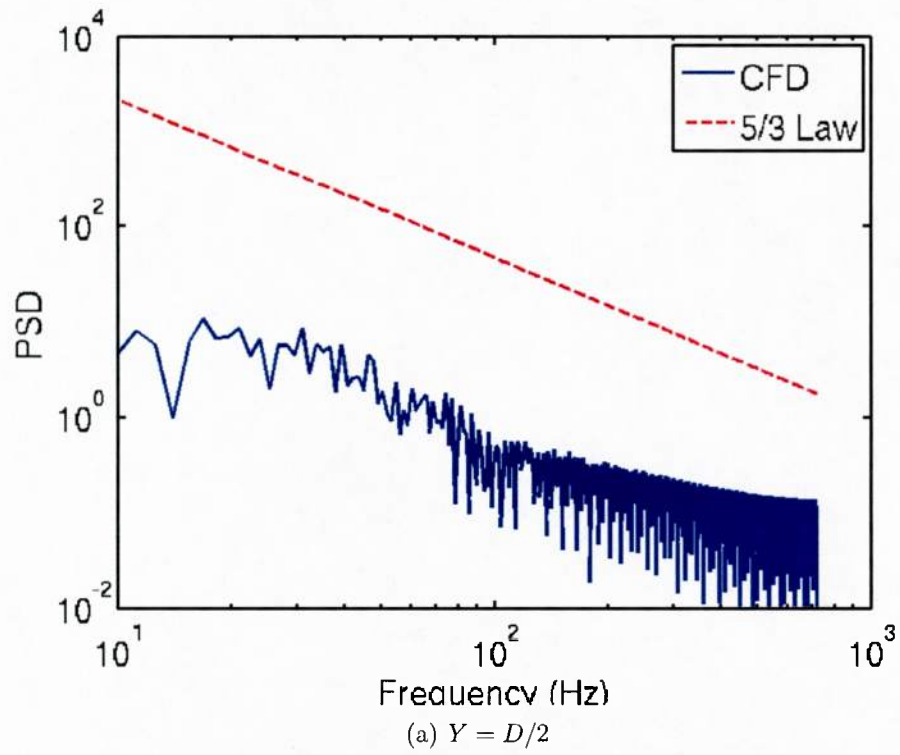


Figure 84: Wake spectra comparison at  $Z = 0.0$  m and  $X = 5D$  at 240 rpm.

## 8 Summary of Findings

Using a combination of experimental and computational methods, the characterization of the integrated loads and complex wake field of a scaled helicopter main rotor hub has been obtained. From this investigation, it can be concluded that

1. Large regions of separated flow contribute to considerable drag from the complex hub. The azimuthal variation of the static hub model shows variation in drag corresponding to the projected frontal area of the hub. For the four-bladed hub configuration, the  $45^\circ$  azimuthal orientation yields similar drag measurements to the mean values obtained for the rotating hub.
2. Initial deconstruction of the hub configuration has provided insight into the drag breakdown and interference effects of geometric components. At the Reynolds numbers and free stream velocities examined, the hub plates and blade shanks contribute approximately  $1/3$  of the hub drag, while the remaining contribution is due to flow separation about the drive shaft, pitch links and swashplate in that order. Rotation effects on the deconstructed model are observed to be minimal at the flow conditions evaluated.
3. Computational prediction at the fidelity level of the FUN3D Navier-Stokes solver, has been shown to be an invaluable tool to augment experimental analyses for this complex hub configuration. Strong correlations between CFD and both experiment load and PIV data permit the utilization of the surface and flow field characteristics predicted by CFD to further explain and clarify the causal physics due to the complex hub geometry.
4. New CFD capabilities developed to permit unstructured overset anisotropic feature-based adaptation across both background and near-body grids are essential to capture the correct physics of complex configurations where significant wake interactions occur in both the near- and far-field grids.
5. The hub characteristics were identified with computational methods for both full assembly and deconstructions of the hub. From these, identification of where theoretical approximations can be applied were identified. Interference effects were also quantified, and the sources identified, including the influence of a fuselage.
6. Strouhal shedding and wake interactions were computed from the rich data provided from the computational simulations. Important effects of scaling for both static and rotating hubs were quantified; it is clear that there are significant differences in the behavior of the hub and the component interference between model and full helicopter scales. Turbulent spectra confirmed the ability to maintain complex wake behavior over these long periods.
7. Long-age wake data were captured and correlated with experimental data from other sources to show that prediction and analysis of empennage-based aeroelastic and un-

steady aerodynamic phenomena, such as tail buffet and “wag” are within reach of current computational resources.

Computational methods have now reached a maturity that, if care is taken in the grid generation and turbulence modeling, it may be more cost-effective and accurate to design and analyze complex hubs directly with computational methods rather than reliance on model scale experiments. Advanced turbulence models that use detached or large eddy simulations and grid adaptation are recommended to improve the performance quantities and the unsteady wake characteristics.

## 9 Management

### 9.1 Research Leveraging

This work leveraged the funding to study the scaling effects of hubs from the Vertical Lift Consortium.<sup>96</sup> Mr. Rajiv Shenoy also spent two summers as a NASA Langley Research Summer Scholar (LARSS) while working on portions of the grid adaptation. Finally, this research has leveraged the turbulence modeling from the DARPA Quiet Helicopter program and Task 3 of the Georgia Tech Vertical Lift Research Center of Excellence (VLRCOE).

### 9.2 Technology Transfer

The modifications made to the FUN3D code have been provided to the NASA-Langley FUN3D Development group, and have or will be released in production versions of the code.

Several projects are currently using the overset grid adaptation developed in this portion of the project. They include Task 10 of the Georgia Tech Vertical Lift Research Center of Excellence (VLRCOE), “Aerodynamic and Dynamic Interaction of Bluff Bodies” and a new Army Research Office project on Dynamic Stall, both of which have as the PD (co-PI with one other faculty member on each) Prof. Smith.

### 9.3 Awards

- Rajiv Shenoy, Vertical Flight Foundation, 2013 PhD Scholarship Winner
- Rajiv Shenoy, Vertical Flight Foundation, 2011 MS Scholarship Winner
- Rajiv Shenoy, “Scaling Hub Drag from Model to Full Scale,” MSAE Awarded December 2011

### 9.4 Publications

A number of conference and journal papers have resulted from funding (or partial funding) from this effort. These papers include:

- Shenoy, R., Smith, M. J., and Park, M. A., “Unstructured Overset Mesh Adaptation with Turbulence Modeling for Unsteady Aerodynamic Interactions,” *AIAA Journal of Aircraft*, in press, 2013.
- Raghav, V., Shenoy, R., Smith, M. J., and Komerath, N. M., “Investigation of Drag and Wake Turbulence of a Rotor Hub,” *Aerospace Science and Technology*, Vol. 28, (1), doi: 10.1016/j.ast.2012.10.012, 2013, pp. 164175.
- Shenoy, R. “An Adaptive Mesh Refinement Strategy for Static and Dynamic Overset Grids,” Overset Grid Symposium Student Poster Competition, October, 2012.

- Ortega, F., Shenoy, R., Raghav, V., Smith, M. J., and Komerath, N., “Exploration of the Physics of Hub Drag,” Paper AIAA-2012-1070, AIAA Aerospace Sciences Meeting and Exhibit, Knoxville, TN, January 9-12, 2012.
- Shenoy, R., Raghav, V., Ortega, F., Smith, M. J., and Komerath, N., “Deconstructing Hub Drag,” Paper AIAA-2011-3821, AIAA 29th Applied Aerodynamics Conference, June 27-30, 2011.
- Shenoy, R. and Smith, M. J., “Unstructured Overset Adaptive Mesh Refinement for Rotorcraft Aerodynamic Interactions,” Proceedings of the 67th Annual Forum of the American Helicopter Society, May 25, 2011.

The additional funding obtained from the Vertical Lift Consortium (VLC) for the scaling computations has resulted in the following papers, which also utilized results from this effort:

- Shenoy, R., Holmes, M., Smith, M. J., and Komerath, N., “Scaling Evaluations on the Drag of a Hub System,” *Journal of the American Helicopter Society*, Vol. 58, (3), July 2013, pp. 113.
- Shenoy, R., Smith, M. J., and Komerath, N., “Computational Investigation of Hub Drag Deconstruction from Model to Full Scale,” Proceedings of the 37th European Rotorcraft Forum, Gallarate, Italy, September 12-15, 2011.

In addition, Mr. Rajiv Shenoy is planning to defend his PhD dissertation in December, 2013, which will include some of the computations reported here. It will include additional computations using the configurations explored in this effort. This report will be available through the Georgia Tech SmartTech system: <http://www.smarttech.gatech.edu>.

## 9.5 Data Availability

Animations that show in additional detail the physics of the wakes of the hub from computational simulations are available at <http://www.msmith.gatech.edu/research/hubdrag>.

Larger data files, including CAD geometry, computational grids, and computational wake data are planned to be incorporated into the “big data” resources being developed at the Georgia Institute of Technology, of which Prof. Marilyn Smith (the PI of this task) is a participant. Links to this web resource will be provided on the afore provided website or can be obtained via email request to the PI of this task, Prof. Marilyn Smith.

## 9.6 Training

This effort provided additional unfunded training for Marlin Holmes (BSAE, May 2013) and Philip Cross in the area of CFD data reduction.

## 10 Acknowledgments

Computational support was provided through the DoD High Performance Computing Centers at ERDC through an HPC grant from the US Navy. Any opinions, findings, and conclusions or recommendations expressed in this material are those of the author(s) and do not necessarily reflect the views of the Department of the Navy or the Office of Naval Research.

The authors would like to acknowledge and thank the NASA FUN3D development team, in particular Dr. Michael Park and Dr. Eric Nielsen, who pioneered the grid adaptation efforts within FUN3D.

The authors would like to thank Marlin Holmes and Philip Cross for their help in the data reduction of the computational analysis for both this and the Vertical Lift Consortium efforts.

The authors would also like to acknowledge Profs. Jerry Seitzman and Ari Glezer of the Georgia Institute of Technology who provided insight and help in analyzing the experimental data, especially the hot wire anemometry experimental data from the 2013 tests.

## 11 References

- [1] Williams, R. and Montana, P., “A Comprehensive Plan for Helicopter Drag Reduction,” Technical report, Naval Ship Research and Development Center, Maryland, 1975.
- [2] Keys, C., Wiesner, R., *et al.*, “Guidelines for Reducing Helicopter Parasite Drag,” *Journal of the American Helicopter Society*, Vol. 20, 1975, pp. 31.
- [3] Hoffman, J., “The Relationship Between Rotorcraft Drag and Stability and Control,” Proceedings of the 31st Annual National Forum of the American Helicopter Society, May 1975.
- [4] Kerr, A., “Effect of Helicopter Drag Reduction on Rotor Dynamic Loads and Blade Life,” Proceedings of the American Helicopter Society Symposium on Helicopter Aerodynamic Efficiency, March, 1975.
- [5] Wake, B., Hagen, E., Ochs, S., and Matalanis, C., “Assessment of Helicopter Hub Drag Prediction with an Unstructured Flow Solver,” 65th Annual Forum of the American Helicopter Society, May 2009.
- [6] Saltzman, E. and Ayers, T., “A Review of Flight-to-Wind Tunnel Drag Correlation,” Paper AIAA-1981-2475, 1981.
- [7] Bushnell, D., “Sealing: Wind Tunnel to Flight,” *Ann. Rev. of Fluid Mechanics*, Vol. 38, (1), 2006, pp. 111–128.
- [8] Vassberg, J. and *et al.*, “Summary of the Fourth AIAA CFD Drag Prediction Workshop.” Paper AIAA-2010-4547, 2010.
- [9] Ueno, M., Akatsuka, J., and Hidaka, A., “Drag Decomposition Analysis of CFD Data of the DLR-F6 Model,” Paper AIAA-2008-6903, August 2008.
- [10] McCroskey, J., “Computations of Unsteady Separating Flows over an Oscillating Airfoil,” *AIAA Journal*, Vol. 35, (7), 1997, pp. 1235–1238.
- [11] Keys, C. and Rosenstein, H., “Summary of Rotor Hub Drag Data,” Technical Report NASA CR-152080, Ames Research Center, 1978.
- [12] Potsdam, M. and Le Pape, A., “CFD Investigations on a NACA0036 Airfoil with Active Flow Control,” Paper AIAA-2008-3869, 4th Flow Control Conference, Seattle, Washington, June 23–26 2008.
- [13] Gregory, J., Porter, C., and McLaughlin, T., “Circular Cylinder Wake Control using Spatially Distributed Plasma Forcing,” 38 th AIAA Fluid Dynamics Conference and Exhibit, 39 th AIAA Plasmadynamics and Lasers Conference, 40 th AIAA Thermophysics Conference, 5 th AIAA Theoretical Fluid Mechanics Conference, 4 th AIAA Flow Control Conference, and the 26 th AIAA Aerodynamic Measurement Technology and Ground Testing Conference, 2008.

- [14] Roshko, A., "Perspectives on bluff body aerodynamics," *Journal of Wind Engineering and Industrial Aerodynamics*, Vol. 49, (1-3), 1993, pp. 79–100.
- [15] Sheehy, T. and Clark, D., "A Method for Predicting Helicopter Hub Drag," Technical report, United Technologies Corp., Stratford CT, Sikorsky Aircraft Div., 1976.
- [16] Sheehy, T. *et al.*, "A general review of helicopter rotor hub drag data," *Journal of the American Helicopter Society*, Vol. 22, 1977, pp. 2.
- [17] Ochs, S. S., Matalanis, C. G., Wake, B. E., and Egolf, T. A., "Evaluation of Helios CFD Toolset for Faired Rotor-Hub Drag Prediction," American Helicopter Society 67th Annual Forum Proceedings, Virginia Beach, Virginia, May 3-5 2011.
- [18] Bridgeman, J. O. and Lancaster, G. T., "Predicting Hub Drag on Realistic Geometries," American Helicopter Society Aeromechanics Specialists Conference, San Francisco, California, January 20-22 2010.
- [19] Bridgeman, J. O. and Lancaster, G. T., "Physics-Based Analysis Methodology for Hub Drag Prediction," American Helicopter Society 66th Annual Forum Proceedings, Phoenix, Arizona, May 11-13 2010.
- [20] Hill, M. J. and Louis, M. E., "Rotating Hub Drag Prediction Methodology," American Helicopter Society Specialists Conference on Future Vertical Lift Aircraft Design, San Francisco, California, January 18-20 2012.
- [21] Reich, D. and Elbing, B. and Berezin, C. and Schmitz, S., "Water Tunnel Flow Diagnostics of Wake Structures Downstream of a Model Helicopter Rotor Hub," American Helicopter Society 69th Annual Forum Proceedings, Phoenix, Arizona, May 2013.
- [22] Ruffin, S., O'Brien, D., Smith, M., Hariharan, N., Lee, J., and Sankar, L., "Comparison of Rotor-Airframe Interaction Utilizing Overset Unstructured Grid Techniques," Proceedings of the 42nd AIAA Aerospace Sciences Meeting and Exhibit, Jan 2004.
- [23] O'Brien, D., and Smith, M., "Understanding the Physical Implications of Approximate Rotor Methods Using an Unstructured CFD Method," Proceedings of the 31st Annual European Rotorcraft Forum, Sep 2005.
- [24] O'Brien, D. M., *Analysis of Computational Modeling Techniques for Complete Rotorcraft Configurations*, Ph.D. thesis, Georgia Institute of Technology, 2006.
- [25] Potsdam, M., Smith, M., and Renaud, T., "Unsteady Computations of Rotor-Fuselage Interactions," Proceedings of the 35th Annual European Rotorcraft Forum, Sep 2009.
- [26] Smith, M.J., Shenoy, R., Kenyon, A.R., and Brown, R.E., "Vorticity Transport and Unstructured RANS Investigation of Rotor-Fuselage Interactions," Proceedings of the 35th Annual European Rotorcraft Forum, Sep 2009.

- [27] Komerath, N., Smith, M. J., Tung, C., "A Review of Rotor Wake Physics and Modeling," *Journal of the American Helicopter Society*, Vol. to appear, 2011.
- [28] Kang, H.J. and Kwon, O.J., "Effect of Wake Adaptation on Rotor Hover Simulations Using Unstructured Meshes," *Journal of Aircraft*, Vol. 38, (5), 2001.
- [29] Kang, H.J. and Kwon, O.J., "Unstructured Mesh Navier-Stokes Calculations of the Flow Field of a Helicopter Rotor in Hover," *Journal of the American Helicopter Society*, Vol. 47, (2), 2002.
- [30] Dindar, M., Shepherd, M., Flaherty, J., and Jansen, K., "Adaptive CFD analysis for rotorcraft aerodynamics," *Computer Methods in Applied Mechanics and Engineering*, Vol. 189, (4), 2000.
- [31] Potsdam, M. and Mavriplis, D., "Unstructured Mesh CFD Aerodynamic Analysis of the NREL Phase VI Rotor," 47th AIAA Aerospace Sciences Meeting, Jan 2009.
- [32] Park, Y.M. and Kwon, O.J., "Simulation of Unsteady Rotor-Fuselage Interactions Using Unstructured Adaptive Sliding Meshes," *Journal of the American Helicopter Society*, Vol. 49, (4), 2006.
- [33] Cavallo, P.A., Sinha, N., and Feldman, G.M., "Parallel Unstructured Mesh Adaptation Method for Moving Body Applications," *AIAA Journal*, Vol. 43, (9), 2005.
- [34] Meakin, R.L., "On adaptive refinement and overset structured grids," Proceedings of the 13rd AIAA Computational Fluid Dynamics Conference, June 1997.
- [35] Henshaw, W.D., and Schwendeman, D.W., "Parallel Computation of Three-dimensional Flows Using Overlapping Grids with Adaptive Mesh Refinement," *Journal of Computational Physics*, Vol. 227, (16), 2008.
- [36] Kannan, R., and Wang, Z.J., "Overset Adaptive Cartesian/Prism Grid Method for Stationary and Moving-Boundary Flow Problems," *AIAA Journal*, Vol. 45, (7), 2007.
- [37] Canonne, E., Benoit, C., and Jeanfaivre, G., "Cylindrical mesh adaptation for isolated rotors in hover," *Aerospace Science and Technology*, Vol. 8, (1), 2004.
- [38] Duque, E.P.N., Biswas, R. and Strawn, R.C., "A Solution Adaptive Structured/Unstructured Overset Grid Flow Solver with Applications to Helicopter Rotor Flows," Proceedings of the 13rd AIAA Applied Aerodynamics Conference, June 1995.
- [39] Park, M.A. and Darmofal, D.L., "Parallel Anisotropic Tetrahedral Adaptation," Proceedings of the 46th AIAA Aerospace Sciences Meeting and Exhibit, Jan 2008.
- [40] Lee-Rausch, E.M., Park, M.A., Jones, W.T., Hammond, D.P, and Nielsen, E.J., "Application of Parallel Adjoint-Based Error Estimation and Anisotropic Grid Adaptation for Three-Dimensional Aerospace Configurations," Proceedings of the 23rd AIAA Applied Aerodynamics Conference, June 2005.

- [41] Jones, W.T., Nielsen, E.J. and Park, M.A., “Validation of 3D Adjoint Based Error Estimation and Mesh Adaptation for Sonic Boom Prediction,” Proceedings of the 44th AIAA Acrospace Sciences Meeting and Exhibit, Jan 2006.
- [42] Bibb, K.L., Gnoffo, P.A., Park, M.A. and Jones, W.T. , “Parallel, Gradient-Based Anisotropic Mesh Adaptation for Re-entry Vehicle Configurations,” Proceedings of the 9th AIAA/ASME Joint Therophysics and Heat Transfer Conference, Jun 2006.
- [43] Sankaran, V., Sitaraman, J., Wissink, A., Datta, A., Jayaraman, B., Potsdam, M., Mavriplis, D., Yang, Z., O’Brien, D., Saberi, H., Cheng, R., Hariharan, N., and Strawn, R., “Application of the Helios Computational Platform to Rotorcraft Flowfields,” Proceedings of the 48th AIAA Acrospace Sciences Meeting and Exhibit, Jan 2010.
- [44] Wissink, A.M., Kamkar, S., Pulliam, T.H., Sitaraman, J., and Sankaran, V., “Cartesian Adaptive Mesh Refinement for Rotorcraft Wake Resolution,” Proceedings of the 28th AIAA Applied Aerodynamics Conference, June 2010.
- [45] Wissink, A., Potsdam, M., Sankaran, V., Sitaraman, J., Yang, Z., and Mavriplis, D. J., “A Coupled Unstructured-Adaptive Cartesian CFD Approach for Hover Prediction,” Proceedings of the 66th Annual Forum of the American Helicopter Society, May 2010.
- [46] Sterenborg, J., van Zuijlen, A., and Bijl, H., “Solution Based Mesh Adaptation Applied to Fluid Structure Interaction Computations,” 47th AIAA Aerospace Sciences Meeting, Jan 2009.
- [47] Alauzet, F. and Olivier, G., “Extension of Metric-Based Anisotropic Mesh Adaptation to Time-Dependent Problems Involving Moving Geometries,” Proceedings of the 49th AIAA Acrospace Sciences Meeting and Exhibit, Jan 2011.
- [48] Pirzadeh, S., “Advanced Unstructured Grid Generation for Complex Aerodynamic Applications,” *AIAA Journal*, Vol. 48, (5), 2010, pp. 904–915.
- [49] Noack, R., Boger, D., Kunz, R., and Carrica, P., “SUGGAR++: An Improved General Overset Grid Assembly Capability,” Proceedings of the 19th AIAA Computational Fluid Dynamics Conference, June 2009.
- [50] Renaud, T., O’Brien, D. M., Jr., Smith, M. J., and Potsdam, M., “Evaluation of Isolated Fuselage and Rotor-Fuselage Interaction Using CFD,” *Journal of the American Helicopter Society*, Vol. 53, (1), 2008, pp. 3–17.
- [51] Liggett, N. and Smith, M. J., “Temporal Convergence Criteria for Time-Accurate Viscous Simulations of Separated Flows,” *Computers & Fluids*, Vol. 66, doi: 10.1016/j.compfluid.2012.06.010, 2012, pp. 140–156.
- [52] Komerath, N., “Deconstructing Hub Drag, Part I: Experiments,” Technical Report ONR Final Report, September 2013.

- [53] Anderson, W., Rausch, R., and Bonhaus, D., “Implicit/Multigrid Algorithms for Incompressible Turbulent Flows on Unstructured Grids,” *Journal of Computational Physics*, Vol. 128, (2), 1996.
- [54] Chorin, A., “A Numerical Method for Solving Incompressible Viscous Flow Problems,” *Journal of Computational Physics*, Vol. 135, (2), 1997.
- [55] Roe, P., “Approximate Riemann Solvers, Parameter Vectors, and Difference Schemes,” *Journal of Computational Physics*, Vol. 43, (2), 1981.
- [56] Menter, F., “Two-Equation Eddy-Viscosity Turbulence Models for Engineering Applications,” *AIAA Journal*, Vol. 32, (8), 1994.
- [57] Sanchez-Rocha, M. and Menon, S., “The Compressible Hybrid RANS/LES Formulation using an Additive Operator,” *Journal of Computational Physics*, Vol. 228, 2009, pp. 2037–2062.
- [58] Sanchez-Rocha, M. and Menon, S., “An order-of-magnitude approximation for the hybrid terms in the compressible hybrid RANS/LES governing equations,” *Journal of Turbulence*, Vol. 12, 2011, pp. 1–22.
- [59] Noack, R., “DiRTlib: A Library to Add an Overset Capability to Your Flow Solver,” Proceedings of the 17th AIAA Computational Fluid Dynamics Conference, June 2005.
- [60] Renaud, T., D. M. O’Brien, J., Smith, M. J., and Potsdam, M., “Evaluation of Isolated Fuselage and Rotor-Fuselage Interaction Using CFD,” *Journal of the American Helicopter Society*, Vol. 53, (1), 2008, pp. 3–17.
- [61] Lynch, C. E., *Advanced CFD Methods for Wind Turbine Analysis*, Ph.D. thesis, Georgia Institute of Technology, 2011.
- [62] Abras, J. N., *Enhancement of Aeroelastic Rotor Airload Prediction Methods*, Ph.D. thesis, Georgia Institute of Technology, 2009.
- [63] Lynch, C. E. and Smith, M. J., “Extension and Exploration of a Hybrid Turbulence Model on Unstructured Grids,” *AIAA Journal*, Vol. 49, (11), 2011, pp. 2585–2591. doi: 10.2514/1.56296
- [64] Liggett, N. and Smith, M. J., “A Study of the Gap Physics of Airfoils with Unsteady Flaps,” *AIAA Journal of Aircraft*, Vol. 50, (2), doi: 10.2514/1.C032026, 2013, pp. 643–650.
- [65] Kravchenko, A. G. and Moin, P., “Numerical Studies of Flow Over a Circular Cylinder at  $Re_D = 3900$ ,” *Physics of Fluids*, Vol. 12, (2), 2000, pp. 403–417.
- [66] Norberg, C., Unpublished data that was digitized from Fig. 11 in Ref.<sup>65</sup>.

- [67] Son, J. and Hanratty, T. J., "Velocity Gradients at the Wall for Flow Around a Cylinder at Reynolds Numbers  $5 \times 10^3$  to  $10^5$ ," *Journal of Fluid Mechanics*, Vol. 35, (2), 1969, pp. 353–368.
- [68] Ong, L. and Wallace, J., "The Velocity Field of the Turbulent Very Near Wake of a Circular Cylinder," *Experimental Fluids*, Vol. 20, (6), 1996, pp. 441–453.
- [69] Menter, F., "Two-Equation Eddy-Viscosity Turbulence Models for Engineering Applications," *AIAA Journal*, Vol. 32, (8), 1994, pp. 1598–1605.
- [70] Spalart, P. R., "Strategies for Turbulence Modelling and Simulations," *International Journal of Heat and Fluid Flow*, Vol. 21, (3), 2000, pp. 252–263.
- [71] Menter, F., "Review of the Shear-Stress Transport Turbulence Model Experience from an Industrial Perspective," *International Journal of Computational Fluid Dynamics*, Vol. 23, (4), 2009, pp. 305–316.
- [72] Smirnov, P. E. and Menter, F. R., "Sensitization of the SST Turbulence Model to Rotation and Curvature by Applying the Spalart-Shur Correction Term," *Journal of Turbomachinery*, Vol. 131, (4), 2009, pp. 1–8.
- [73] "tecplot 360 2013 User's Manual, Release 1," Technical report, Tecplot, Inc., Bellevue, WA, 2013.
- [74] "Fieldview 13 User's Manual," Technical report, Intelligent Light, 2013.
- [75] "MATLAB R2013b User's Manual," Technical report, MathWorks, Inc., Natick, Massachusetts, 2013.
- [76] Bridgeman, J. and Lancaster, G., "Physics-Based Analysis Methodology for Hub Drag Prediction," Proceedings of the 66th Annual Forum of the American Helicopter Society, May 2010.
- [77] Shenoy, R., Smith, M. J., and Park, M. A., "Unstructured Overset Mesh Adaptation with Turbulence Modeling for Unsteady Aerodynamic Interactions," *AIAA Journal of Aircraft*, in press.
- [78] Park, M. A., *Anisotropic Output-Based Adaptation with Tetrahedral Cut Cells for Compressible Flows*, Ph.D. thesis, Massachusetts Institute of Technology, 2008.
- [79] Kamkar, S. J., *Mesh Adaption Strategies for Vortex-Dominated Flows*, Ph.D. thesis, Stanford University, 2011.
- [80] Venditti, D. A., *Grid Adaptation for Functional Outputs of Compressible Flow Simulations*, Ph.D. thesis, Massachusetts Institute of Technology, 2002.
- [81] Brand, A. G., *An Experimental Investigation of the Interaction Between a Model Rotor and Airframe in Forward Flight*, Ph.D. thesis, Georgia Institute of Technology, 1989.

- [82] Mavris, D. N., *An Analytical Method for the Prediction of Unsteady Rotor/Airframe Interactions in Forward Flight*, Ph.D. thesis, Georgia Institute of Technology, 1988, revised 1991.
- [83] O'Brien, D., and Smith, M., "Analysis of Rotor-Fuselage Interactions Using Various Rotor Models," Proceedings of the 43rd AIAA Aerospace Sciences Meeting and Exhibit, Jan 2005.
- [84] Lee, J. and Kwon, O.J., "Predicting Aerodynamic Fuselage Interactions by Using Unstructured Meshes," *Transactions of the Japanese Society for Aeronautical and Space Sciences*, Vol. 44, (146), 2002.
- [85] O'Brien, D. M., *Analysis of Computational Modeling Techniques for Complete Rotorcraft Configurations*, Ph.D. thesis, Georgia Institute of Technology, Atlanta, Georgia, 2006.
- [86] Park, M.A. and Carlson, J.R., "Turbulent Output-Based Anisotropic Adaptation," Proceedings of the 48th AIAA Aerospace Sciences Meeting and Exhibit, Jan 2010.
- [87] Mineck, R. and Althoff Gorton, S., "Steady and Periodic Pressure Measurements on a Generic Helicopter Fuselage Model in the Presence of a Rotor," Technical Report NASA/TM-2000-210286, June 2000.
- [88] Ghee, T.A. and Elliott, J.W., "The Wake of a Small-Scale Rotor in Forward Flight Using Flow Visualization," *Journal of the American Helicopter Society*, Vol. 40, (3), 1995.
- [89] Park, Y.M., Nam, H.J, and Kwon, O.J., "Simulation of Unsteady Rotor-Fuselage Interactions Using Unstructured Adaptive Meshes," *Journal of the American Helicopter Society*, Vol. 51, (2), 2006.
- [90] Kenyon, A.R. and Brown, R.E., "Wake Dynamics and Rotor-Fuselage Aerodynamic Interactions," *Journal of the American Helicopter Society*, Vol. 54, (1), 2009.
- [91] Raghav, V., Shenoy, R., Smith, M. J., and Komerath, N. M., "Investigation of Drag and Wake Turbulence of a Rotor Hub," *Aerospace Science and Technology*, Vol. 28, (1), doi: 10.1016/j.ast.2012.10.012, 2013, pp. 164–175.
- [92] Lynch, C. E. and Smith, M. J., "Hybrid RANS-LES Turbulence Models on Unstructured Grids," Proceedings of the 38th Fluid Dynamics Conference and Exhibit, June 2008.
- [93] Shenoy, R., Holmes, M., Smith, M. J., and Komerath, N., "Scaling Evaluations on the Drag of a Hub System," *Journal of the American Helicopter Society*, Vol. 58, (3), July 2013, pp. 1–13.
- [94] Schlichting, H., *Boundary Layer Theory, 7th edition*, McGraw-Hill, New York, NY, 1979.

- [95] Hoerner, S. F., *Fluid Dynamic Drag*, Sighar Hoerner, 1965.
- [96] Shenoy, R., Smith, M. J., and Komerath, N., "Computationally Deconstructing Drag From Model To Full Scale," Technical Report Vertical Lift Consortium Final Report, WBS 2011-B-11-07.3-A1, February 2013.
- [97] Zdravkovich, M. M., *Flow Around Circular Cylinders, Vol. 2: Applications*, Oxford Science Publications, New York, NY, 2003.
- [98] Sakamoto, H. and Arie, M., "Vortex shedding from a rectangular prism and a circular cylinder placed vertically in a turbulent boundary layer," *Journal of Fluid Mechanics*, Vol. 126, (-1), 1983, pp. 147-165.
- [99] Bousman, W. G. and Kufeld, R. M., "UH-60A Airloads Catalog," Technical Report NASA TM-2005-212827/AFDD TR-05-003, August 2005.

# REPORT DOCUMENTATION PAGE

Form Approved  
OMB No. 0704-0188

Public reporting burden for this collection of information is estimated to average 1 hour per response, including the time for reviewing instructions, searching data sources, gathering and maintaining the data needed, and completing and reviewing the collection of information. Send comments regarding this burden estimate or any other aspect of this collection of information, including suggestions for reducing this burden to Washington Headquarters Service, Directorate for Information Operations and Reports, 1215 Jefferson Davis Highway, Suite 1204, Arlington, VA 22202-4302, and to the Office of Management and Budget, Paperwork Reduction Project (0704-0188) Washington, DC 20503.

PLEASE DO NOT RETURN YOUR FORM TO THE ABOVE ADDRESS.

1. REPORT DATE (DD-MM-YYYY) 30-09-2013		2. REPORT TYPE Final Technical Report (Part 2 of 2)		3. DATES COVERED (From - To) 01-07-2009 to 30-06-2013	
4. TITLE AND SUBTITLE Deconstructing Hub Drag Part II: Computational Development and Analysis				5a. CONTRACT NUMBER	
				5b. GRANT NUMBER N0001409-1-1019	
				5c. PROGRAM ELEMENT NUMBER	
6. AUTHOR(S) Rajiv Shenoy and Marilyn J. Smith				5d. PROJECT NUMBER	
				5e. TASK NUMBER	
				5f. WORK UNIT NUMBER	
7. PERFORMING ORGANIZATION NAME(S) AND ADDRESS(ES) Georgia Tech Research Corporation Daniel Guggenheim School of Aerospace Engineering Georgia Institute of Technology Atlanta, GA 30332-0150				8. PERFORMING ORGANIZATION REPORT NUMBER	
9. SPONSORING/MONITORING AGENCY NAME(S) AND ADDRESS(ES) Office of Naval Research 875 North Randolph Street Arlington, VA 22203-1995				10. SPONSOR/MONITOR'S ACRONYM(S)	
				11. SPONSORING/MONITORING AGENCY REPORT NUMBER	
12. DISTRIBUTION AVAILABILITY STATEMENT Distribution approved for public release; distribution is unlimited					
13. SUPPLEMENTARY NOTES Part I of this report on the experimental research reported separately by co-PI Dr. N. Komerath					
14. ABSTRACT Development, validation and demonstration of a computational approach to model complex rotorcraft hubs, their components and their wakes for both static and rotating operation has been developed. A priori computations were compared with experimental results to yield high confidence in the computational analysis. The hub was analyzed for its total and component drag, including interference drag. Components include hub plates, shanks, pitch links, scissors, and hardware. Wake turbulent spectra were obtained for the near and far field wakes, and wake velocities in the near wake. Scaling, influence of the fuselage, and physics of the wake were all explored. With the highly accurate computational approach developed, design and analysis of hubs can be conducted using computations directly on full-scale configurations.					
15. SUBJECT TERMS Hub Drag, Computational Fluid Dynamics, CFD, Large Eddy Simulations, LES, turbulence modeling, grid adaptation, rotational effects, turbulent wake spectra, drag, interference drag,					
16. SECURITY CLASSIFICATION OF:			17. LIMITATION OF ABSTRACT Unlimited	18. NUMBER OF PAGES 127	19a. NAME OF RESPONSIBLE PERSON Prof. Marilyn J. Smith
a. REPORT Unclassified	b. ABSTRACT Unclassified	c. THIS PAGE Unclassified			19b. TELEPHONE NUMBER (Include area code) 404-894-3065